This is to certify that the

dissertation entitled

Characteristics of the superconducting
Magnets for the S800 Spectrometer

presented by

Bo Zhang

has been accepted towards fulfillment
of the requirements for

*Ph.D*_____ degree in *Physics*_____

_____
Major professor

Date *27 Feb. 1997*

Characteristics of the Superconducting Magnets for the S800 Spectrometer

By

Bo Zhang

A DISSERTATION

submitted to
Michigan State University
in partial fulfillment of the requirements
for the Degree of

DOCTOR OF PHILOSOPHY

Department of Physics and Astronomy

1997

ABSTRACT

CHARACTERISTICS OF THE SUPERCONDUCTING MAGNETS FOR THE S800 SPECTROMETER

BY

Bo Zhang

The National Superconducting Cyclotron Laboratory's K1200 cyclotron is capable of providing high quality heavy-ion beams with rigidities of 1.6 GeV/c. However, the highest velocity beams are 200 MeV/nucleon, or 1.28 GeV/c. In order to study the properties of single particle states populated in reactions at these energies, a magnetic spectrometer with an energy resolution $E/\Delta E$ of 10^4 is necessary. To achieve the physics goals, a large acceptance, high resolution spectrometer (S800) has been designed and constructed. The spectrometer system chosen for the S800 is a QQDD configuration. A strongly focussing y-quad immediately after the target allows a large solid angle and x-focussing quad before the dipoles makes efficient use of the dipoles. This thesis describes the magnets that are the heart of the S800.

In the first part of this thesis the beam optics calculations of the S800 spectrometer are presented. Part two is dedicated to the design and construction of two dipoles for the S800 spectrometer. The third part addresses the design and construction of high gradient, large aperture quadrupoles for the S800. The S800 is a software corrected spectrometer; that is, the energy loss and scattering angle are inferred from measurements of the particle's position and angle at the focal plane. In order for the calculations to work, precise and accurate magnetic field maps of the S800 magnets are

important for achieving high resolution using ray reconstruction. The last part of this thesis also includes the field mapping and harmonic analysis of the S800 quadrupole doublet and S800 beamline quadrupole triplets, essential to the ray reconstruction process.

To my wife Wei and my daughter Amy.

ACKNOWLEDGEMENTS

Weishi Wan, Dr. Hong Wang, Jing Wang, Dr. Qing Yang. From them with them, I learned a lot.

I want to thank my parents Yinglian Sun, Guangai Zhang and my brother Hong Zhang for helping me reach this point, my grandmother Dingjing Liu for special role she has played in my life.

Finally, I want to thank the person who taught me the most important lessons of my graduate years, and gave me the love and affection to make it through: my wife Wei Liu.

I am also very grateful to Michigan State University and National Science Foundation for the financial support during my graduate study.

Contents

List of Tables

List of Figures

xiii

Chapter 1

Introduction

Magnetic spectrometers have played an important role in nuclear physics research and have many advantages over other types of particle detectors. First of all, they have the ability to separate products of interest from unwanted products, in some cases to the level of one part in 10^{12} [Mu88]. This allows the detection of products with low production cross sections relative to more probable reactions. Secondly, they also have the ability to make very precise determinations of momentum and energy. For example, with the Split-pole spectrometer and a 35 MeV proton beam the MSU K50 cyclotron, energy resolution as good as 1.5 keV was achieved in inelastic proton scattering [No75]. This is similar to Ge detectors used in γ-ray studies. Spectrometers allow coincidence experiments to be performed with a very selective reaction filter by measuring a forward-going ion in the spectrometer and the coincident particles or gamma rays in detector arrays surrounding the target.

In heavy ion research, such as takes place at the NSCL, the arguments for the use of magnetic spectrometers are equally valid. A measure of their usefulness is the large demand for the magnetic spectrometers at the two heavy ion laboratories in the intermediate energy range of 10 to 100 MeV/nucleon, the NSCL and GANIL. At the NSCL, the S320 spectrometer even with its limited solid angle and resolution had consistently received 30 percent of the beam time and was used in 40 percent

1

of the approved experiments from 1983 to 1990 using the K500 cyclotron. Since that time the A1200 fragment separator [Sh92] has been used as the primary NSCL spectrometer and takes up to 80 % of the beam time. For the first few PACs at the NSCL where S800 experiments were considered 30 % of the beam time has gone to the S800. At GANIL, the SPEG spectrometer has consistently used more than 20 percent of the accelerator time since its completion in 1986 [Mu89].

The NSCL facility has unique capabilities for heavy ion studies. With the K1200 and K500 cyclotrons, experiments with beams from proton to Uranium and energies of 2 to 200 MeV/u are possible. In addition, the A1200 beam analysis device for the K1200 cyclotron is able to measure and define precisely the beam energy, and produce separated radioactive beams which can be transported to any experimental device. A layout of the facility, showing the position for the S800 spectrometer is given in Fig. 1.1.

With the energies and beams available at the NSCL, there is now a wide range of very interesting experiments with the S800 which could be performed. Although it is impossible to conceive of all the potential physics which will be carried out with the spectrometer, the research will include four significant areas: Giant Resonances, Charge Exchange, Direct Reaction Studies and Nuclear structure. A much more detailed description of these areas is covered in A Proposal for Construction of the S800 Spectrometer along with a discussion of why a magnetic spectrometer is essential for these experiments [No89].

The S800 spectrometer will be able to bend and analyze reaction products from the K1200 and the K500 cyclotrons up to a K=800 dipole magnet field bending limit $(E/A(MeV) = K \times (q/A)^2)$. Hence, the S800 spectrometer will be able to bend onto its focal plane any heavy ion extracted from the K1200 and stripped to its equilibrium charge state by a target. For comparison of the S800 to other spectrometers, a figure of
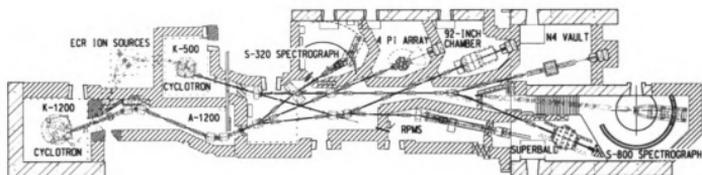
Figure 1.1: Floor plan of the NSCL showing the beam distribution system to allow experiments with the K1200 and K500 cyclotrons.

merit, which will be discussed in more detail in Chapter 2, versus year of construction for various magnetic spectrometers is shown in Fig. 1.2. The S800 spectrometer is among the best in terms of its combination of large solid angle, large energy range, and good energy resolution. This is possible because of the use of superconducting technology and ray reconstruction techniques.

This thesis is organized as follows: The S800 spectrometer properties are discussed in Chapter 2. The design and construction of the S800 dipole are presented in Chapter 3. A detailed design and construction of high gradient, large aperture quadrupoles for S800 spectrometer are given in Chapter 4. Chapter 5 shows the magnetic field mapping and analysis for the S800 quadrupoles. Finally, a summary concludes the thesis.
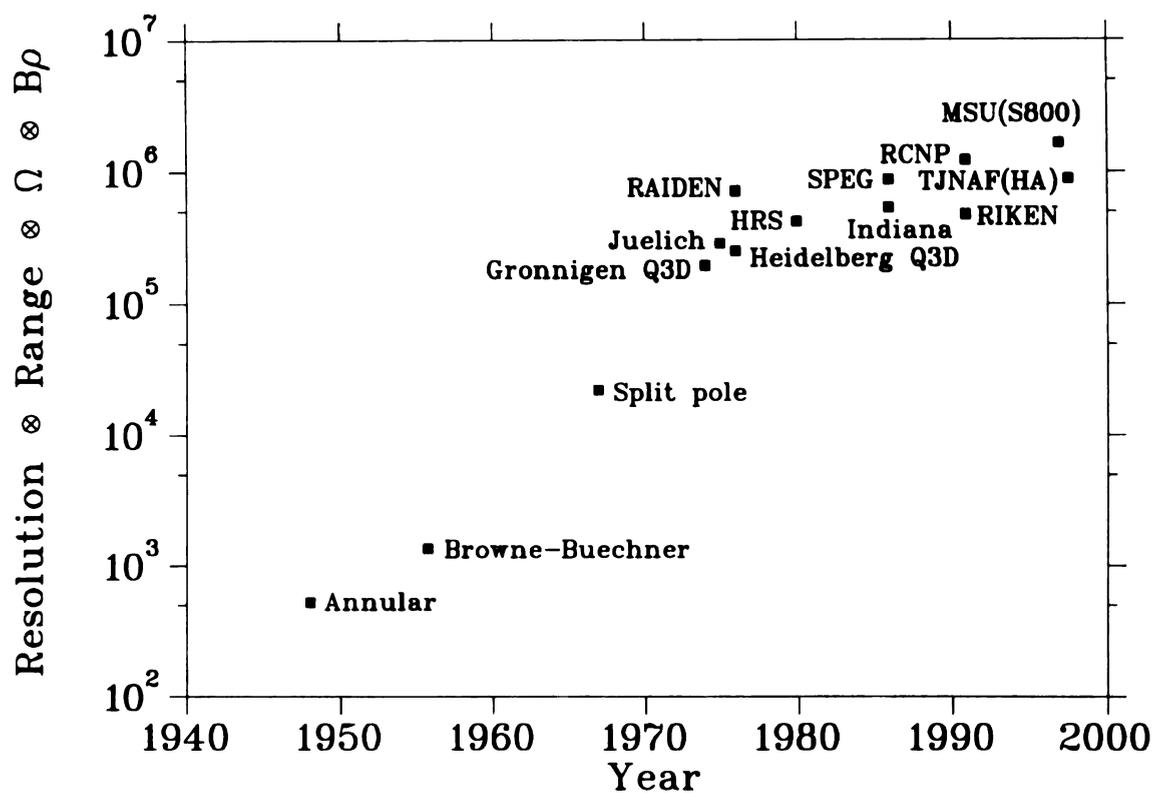
Figure 1.2: Figure of merit versus year of construction for forty years of spectrometer development.

Chapter 2

Optical Properties of the NSCL Superconducting Spectrometer

To achieve the physics goals discussed in Chapter 1 in the most efficient manner, a large acceptance, high resolution spectrometer has been designed and constructed. As illustrated in Fig. 1.2, the S800 spectrometer has a large "figure of merit", that we have defined as the product of resolution, solid angle, energy range and magnetic rigidity. It achieves these values, in part, because it is one of the first superconducting high resolution magnetic spectrometers for nuclear physics. The spectrometer has a design energy resolution $E/\Delta E$ of 10^4 for the entire 20 msr solid angle. This has been demonstrated by raytracing and by a simulation of software corrections through the use of the optimization computer code MOTER [Th79].

Since the appearance of the first magnetic spectrometers in 1948 continuous improvements in resolution, solid angle and range have been made. With the large increase in accelerator energies, the bend radius of spectrometers has been increased from 35 cm [Bu48] to 8.4 m [Ha89], since the practical limit in magnetic field for an iron dominated dipole magnet is in the range of 1.5 to 1.8 T. Calculating an appropriate figure of merit for spectrometers involves solid angle, resolution, energy range, and the particle rigidity, $B\rho$. Additionally, normalization to a 1 mm object size allows

comparison between spectrometers matched to beams of various emittances, allowing a comparison that is independent of the accelerator to which the spectrometer is attached. Fig. 1.2 shows the historical development of spectrometers during the last forty five years.

The unusual physical layout chosen for this spectrometer conveniently satisfies several design goals, constraints and guidelines. Firstly, the combination of vertical beamline dispersion, horizontal scattering, and vertical spectrometer dispersion (VHV) decouples the momentum and scattering angle measurements. This is most relevant for beam phase space matching to the spectrometer. For example, in the dispersive direction it is desirable to have a small incoherent spot size on target, which implies a relatively large divergence, whereas in the scattering direction small beam divergence, and consequently a relatively large spot size, is dictated.

The spectrometer mode was chosen to have the normal point-to-point imaging in the dispersive direction, but parallel-to-point in the axial direction to facilitate accurate scattering angle determinations. This is the system used at the LAMPF HRS in Los Alamos [Mo]. Thus, in first order, the focal plane is two-dimensional with x determining the particle's momentum and y its scattering angle, where the coordinate x is in the plane of bend of the central trajectory and the coordinate y is perpendicular to the plane of bend of the central trajectory (using the standard TRANSPORT notation).

The choice of first order resolving power, or (dispersion/magnification) D/M, for the system is directly related to the resolution specification. The quantity D/Mx_0, where x_0 is the incoherent spot size, determines the first order resolution. It is common to assume $x_0 = 1$ mm at the target so that $(D/M)_s = 20$ cm/% implies a resolution of 20,000. However, in our case we chose to use a high resolving power analysis line $(D/M = 20$ cm/%) to demagnify the beam by 0.6. Thus, a 1 mm spot at

the start of the analysis system is 0.6 mm at the target of the spectrometer and the spectrometer need only a D/M of 12 cm/%. In the case of the S800 $D/M = 12$ cm/%. This choice yields nearly a factor of two larger solid angle for a given dipole width in the spectrometer while still permitting an overall momentum resolution of 20,000 at the spectrometer focal plane [Ro]. The analysis line also allows for dispersion matching. The dispersion matching condition specifies that the dispersion of the beam at target must equal the D/M of the spectrometer or D = 12 cm/% on target in this case. This implies M = 0.6 for the beam spot at the target since $D/M = 20$ cm/% for the beam, yielding an incoherent spot size of 0.6 mm at the target of the spectrometer.

The previous considerations determined the selection of $(D/M)_B$, D_B, and $(D/M)_S$, but they do not determine the spectrometer focal plane dispersion D_S. This term and the associated magnification M_S determine the spatial line width of the beam at the focal plane and the length of the focal plane for a given spectrometer momentum range δ_S. For the present spectrometer $D_S = 12$ cm/% and $M_S = 0.74$ were chosen, giving a line width of 0.5 mm for momentum resolution of 20,000 and a detector length of 60 cm for a momentum range of 5%. It is assumed that a detector resolution of 0.2 mm FWHM for a 60 cm long detector is attainable, so that detector resolution should not limit the system resolution.

The S800 beamline and spectrometer is shown in Fig. 2.1. The design goals and physical parameters are summarized in Table 2.1.

The S800 beamline can operate at beam momenta of up to 1.6 GeV/c even though stripping of the heavy ions at the target limits the maximum rigidity requirement of the spectrometer to 1.2 GeV/c. The analysis system must be for the dispersion-matched (energy-loss) spectrometer. The system must have a momentum resolving power of at least 20,000 with a 1 mm object slit. It must also accept the K1200's
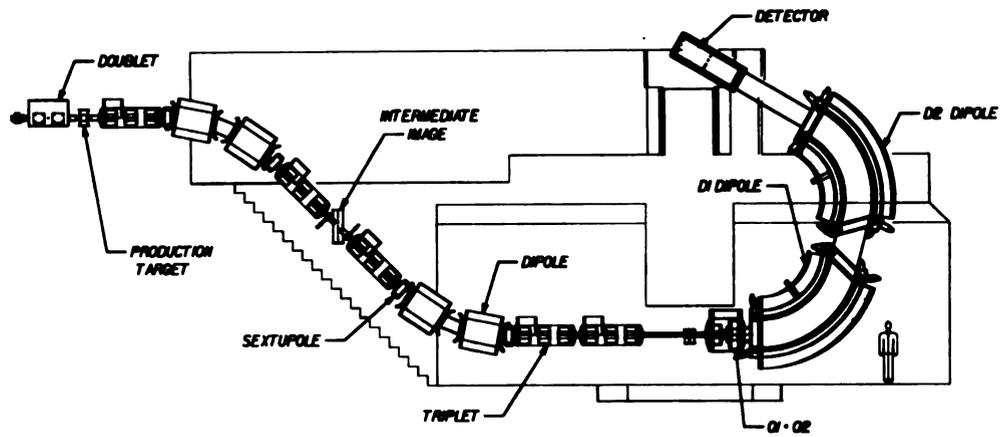
Figure 2.1: The view of the S800 beam analysis system and the spectrometer.

Table 2.1: Parameters of the S800 superconducting spectrometer.

Energy Resolution:	$\Delta E/E = 10^{-4}$ with 1 mm radial object size for beam analysis system
Energy range:	$\Delta E/E = 10\%$
Solid angle:	$\Omega = 10\text{-}20$ msr
Resolving power:	$D/M = 12.3$
Radial dispersion:	$D = 12$ cm/%
Radial magnification:	$M = 0.74$
Axial dispersion:	$R_{34} = 0.88$ mm/mr
Angular resolution:	$\Delta\theta \leq 2$ mr (Total of beam plus spectrometer contributions)
Focal plane size:	50 cm (radial) × 15 cm (axial)
Focal plane tilt:	$28.5°$
Magnetic rigidity limit:	$B\rho = 4$ T·m
Dipole fields:	1.5 T ($\rho = 2.7$ m)
Dipole gap:	$D = 15$ cm
Dipole size:	3.5 m long × 100 cm wide
Weight of dipole:	70 tons each
Quad sizes:	(1) 20.3 cm ID × 40 cm long
	(2) 32.9 cm ID × 40 cm long
Detector Requirements:	Two 2-dimensional detectors 1 m separation
	(1) 50 cm × 15 cm
	(2) 62 cm × 16 cm
	Resolution: Radial 0.2 mm
	Axial 0.4 mm

full phase space of at least 5π mm·mr (axially and radially) and 0.2% in beam energy spread. When coupled to the spectrometer the whole system must be fully achromatic. A TRANSPORT calculation for the entire system is shown in Fig. 2.2. Fig. 2.2 shows the beam envelope and demonstrates the full achromat for a $\delta_B = 0.1\%$ momentum spread in the beam and 5π mm·mr phase space. A more detailed discussion of the beamline optics is given elsewhere [No81].

The two 45° bends are mechanically easier, and cheaper, to achieve by using four 22.5° dipoles. The space between the dipoles allows for placement of sextupoles which are used for second order corrections. Additionally, the smaller bend angle of the individual magnets permit using the dipole magnet design as is used elsewhere in the beam transport system. A more detailed discussion of the S800 beamline dipoles and quadrupoles is given elsewhere [Ze95].

The spectrometer system chosen for the S800 is a QQDD configuration. A strongly focussing y-quad immediately after the target allows a large solid angle (20 msr) and an x-focussing quad before the dipoles makes efficient use of the dipoles. The basic layout of the spectrometer is shown in Fig. 1.1. and an enlarged version is shown in Fig. 2.3. Table 2.2 and Table 2.3 the effects of misalignment on the resolution using MOTOR and COSY INFINITY [Be93a] codes are shown. For each of the four elements Q1, Q2, D1 and D2, we analyzed the sensitivity to unknown errors in position in horizontal and vertical displacements, horizontal and vertical tilts, as well as rotations of the element around the reference trajectory at its entrance, multipole errors in Q1 and Q2.

The first order optics of the spectrometer were chosen to satisfy a complicated set of requirements related to physics measurements, physical constraints. matching to the accelerator beam, simplicity of tuning, and monetary considerations. These considerations have been given elsewhere [No78, No79, Ze81]. The detailed design and
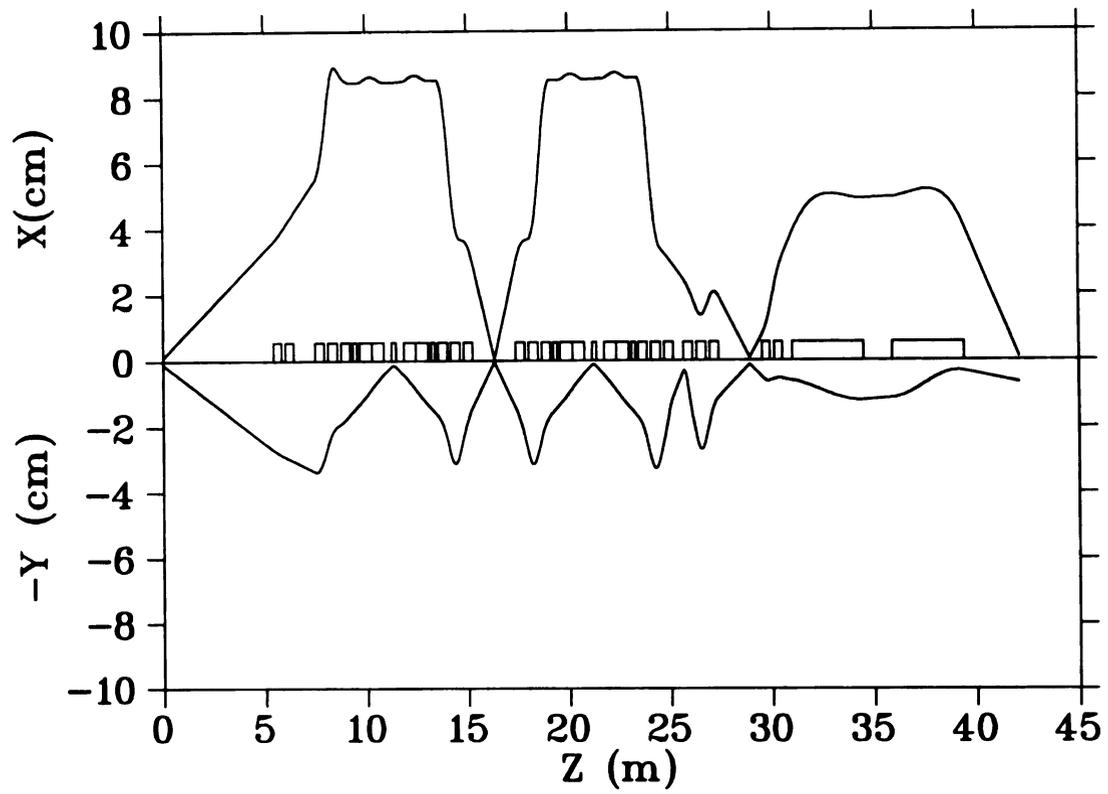
Figure 2.2: The x- and y-envelopes calculated by TRANSPORT for the S800 beamline and spectrometer.

Figure 2.3: Side view of S800 showing position of magnetic elements.

construction of the S800 dipole and quadrupole magnets are discussed in following chapters.

Table 2.2: Sensitivity analysis of misalignment and multipole errors. The energy resolution is parts in 10,000.

Parameter	Change	%Change	ERes (MOTER)	ERes (COSY)
Drift Before Q1	5 mm	0.83	1.12	1.10
Effective Length of Q1	10 mm	2.5	1.09	1.32
Field of Q1	0.011 T	1.	1.41	2.00
Aperture of Q1	0.5 mm	0.4	1.03	1.01
Drift Q1 - Q2	1 mm	0.5	1.22	1.22
Effective Length of Q2	0.5 mm	0.125	1.18	1.16
Field of Q2	0.0013 T	0.2	1.18	1.18
Aperture of Q2	0.8 mm	0.4	1.00	1.00
Drift Q2 - D1	5 mm	1.	1.26	1.22
Deflection Radius D1	5 mm	0.188	1.33	1.25
Deflection Angle D1	0.05 deg	0.07	1.23	1.22
Aperture of D1	5 mm	3.33	1.00	1.00
Entrance Edge Angle D1	0.1 deg	—	1.20	—
Entrance Edge Curv. D1	—	—	—	—
Exit Edge Angle D1	0.1 deg	0.33	1.43	1.82
Exit Edge Curv. D1	—	—	—	—
Half Drift D1 - D2	10 mm	1.43	1.00	1.01
Deflection Radius D2	3 mm	0.11	1.27	1.45
Deflection Angle D2	0.05 deg	0.07	1.32	1.32
Aperture of D2	5 mm	3.33	1.01	1.00
Entrance Edge Angle D2	0.05 deg	0.167	1.16	1.85
Entrance Edge Curv. D2	—	—	—	—
Exit Edge Angle D2	0.05 deg	—	1.23	—
Exit Edge Curv. D2	—	—	—	—
Drift to Focal Plane	5 mm	0.19	1.27	1.20

Table 2.3: Sensitivity analysis of misalignment and multipole errors. The energy resolution is parts in 10,000.

Parameter	Change	%Change	ERes (MOTER)	ERes (COSY)
Hor. misalignment Q1	0.05 mm	—	1.01	1.14
Ver. misalignment Q1	0.05 mm	—	1.00	1.18
Hor. tilt Q1	0.10 deg	—	1.01	1.05
Ver. tilt Q1	0.024 deg	—	1.00	1.02
Rotation Q1	0.041 deg	—	1.05	1.11
Hor. misalignment Q2	1.00 mm	—	1.00	1.05
Ver. misalignment Q2	1.00 mm	—	1.00	1.20
Hor. tilt Q2	0.10 deg	—	1.01	1.08
Ver. tilt Q2	0.05 deg	—	1.00	1.09
Rotation Q2	0.05 deg	—	1.05	1.11
Hor. misalignment D2	3.00 mm	—	1.12	1.00
Ver. misalignment D2	3.00 mm	—	1.08	1.00
Hor. tilt D2	0.10 deg	—	1.15	1.00
Ver. tilt D2	0.10 deg	—	1.41	1.00
Rotation D2	0.09 deg	—	1.01	1.05
Sextupole in Q1	0.0088766 T	0.7555	1.130	1.129
Octupole in Q1	0.0120890 T	1.0289	1.119	1.038
Decapole in Q1	0.0149080 T	1.2688	1.010	1.011
Dodecapole in Q1	0.0350980 T	2.9873	1.019	1.032
Sextupole in Q2	0.0026606 T	0.4089	1.024	1.006
Octupole in Q2	0.0047558 T	0.7310	1.001	1.005
Decapole in Q2	0.0084737 T	1.3024	1.003	1.002
Dodecapole in Q2	0.0127540 T	1.9603	1.004	1.001

Chapter 3

Design and Construction of Large Superconducting Spectrometer Dipoles

3.1 Why use superconducting coils in conventional spectrometer magnets

The S800 is a large solid angle (20 msr) high resolution spectrometer which requires two large gap (15 cm) dipoles with good field uniformity. The maximum field required in these dipoles is 1.5 T. This section is to compare the cost of construction and operation of these dipoles with superconducting coils with those associated with conventional copper coils.

Fig. 3.1 shows the results of a POISSON calculation for a dipole using a superconducting coil. This dipole has a 15 cm gap and a useful field width of 70 cm as required by the spectrometer. It has two small superconducting coils, one above and one below the median plane, which carry 130,000 amp-turns each to produce a 1.5 T field. The top and side pieces are fairly thin (40 cm and 37 cm, respectively) and run at 2.1 ~ 2.2 T when the central field is 1.5 T. The 15 cm gap would require only 100,000 amp-turns if the top and side pieces were much thicker. The resulting dipoles are relatively lightweight, less than 75 tons each for a central path length of

3.5 m. A similar design optimized for a conventional copper coil would be about 50% more massive because the top and side pieces would be thickened to reduce the power requirements.

The total costs of both systems are compared [No81b]. The superconduting version of these dipoles wins by about a factor of 2 in both initial cost and operational cost. The savings are substantial, several hundred thousand dollars. This comparison has been done for one specific dipole design, but generalization to other cases is fairly easy. The costs of the copper coil system scale very rapidly with the gap of the magnet, whereas the costs of the superconducting coil scale very slowly with the magnet gap. Hence, for large gap magnets, e.g. 20 to 30 cm or more, there is absolutely no question that superconducting coils are much more cost effective than conventional coils. The construction of the CEBAF high momentum spectrometer dipole magnet demonstrates this principle [Bo93].

On the other hand, scaling the present estimates down to smaller gaps, e.g. 5 to 10 cm, the cost advantages of the superconducting coils for this style dipole tend to go away. For such smaller dipoles, however, other magnet designs may be more cost effective. We have done preliminary studies of 5 cm Window-frame dipoles with superconducting saddle coils. By using cold steel in these designs very compact systems can be built. In any case, before concluding that superconducting coils are not cost effective for small dipoles, various options must be considered.

It is very clear that any large solid angle, high resolution spectrometer for momenta above 1 GeV/c superconducting coils can permit substantial savings in both initial cost and operational cost.

3.2   Design parameters of S800 dipoles

The specified resolving power, momentum range, and solid angle of the spectrometer, combined with the chosen first order S800 optics, determines the volume of "good" magnetic field required in the S800 dipoles. The choice of dipole to achieve the volume of good field then to a large extent determines the cost of the S800 system. If the dipoles are over designed, they can easily cost two to three times more than necessary. However, if they are under-designed or poorly constructed the system will not meet the resolution specifications at the designed solid angle. (It will have good resolution if the solid angle aperture is stopped down far enough.)

In a system, such as the S800, where focal plane measurements of x_f, y_f, θ_f and ϕ_f are made for physics reasons and aberration corrections, the dipole good field specifications can be greatly reduced. For example, it is certainly not necessary to specify a field flatness of 1 in 20,000 in order to obtain a momentum resolution of 20,000. It is essential that the dipole fields not have small scale or fine structure, but slowly changing field across the dipole widths can be accounted for via the focal plane measurements in the same way as the intrinsic aberrations discussed above.

Quantitative consideration must be given to the upper limit of field gradients which can be accommodated with the focal plane measurements. For example, the following analysis shows that in the present design field gradients of up to 1 gauss per cm in the radial direction can be corrected via focal plane angle measurements. Consider a ray with the central momentum which leaves the target with angle θ_t and hits the focal plane at position x_f with angle θ_f. This ray passes through the dipole with an average radial displacement $\bar{x}_D$ given by:

$$\bar{x}_D = (x/\theta)\theta_t$$

When $(\overline{x/\theta})$ is the average value of the matrix element (x/θ) within the dipoles. Since a change or error in the magnetic field is equivalent to the same percentage change in momentum, then a field variation ΔB changes the x-coordinate at the focal plane by:

$$\Delta x_f = (\Delta B/B)(x/\delta)$$
$$= \frac{(B - B_0)}{B_0}(x/\delta)$$

Assume the actual dipole field B is given by

$$B = B(x_D)$$

Such that

$$\frac{dB}{d\theta} = \frac{dB(x_D)}{dx}(x/\theta).$$

These equations can be combined to give the uncertainty in focal plane x-coordinate δx_f as a function of the uncertainty $\delta\theta_t$ in the initial angle at the target:

$$\delta x_f = \left(\frac{1}{B}\frac{dB}{dx}\right)(x/\theta)(x/\delta)\delta\theta_t$$

Finally, the uncertainty in x_f is converted to momentum uncertainly $\delta(\Delta P/P)$ by dividing by the dispersion (x/δ), and the uncertainty in θ_t is related to the uncertainty in the measured quantity θ_f by the magnification $M_\theta = M_x^{-1}$, yielding:

$$\delta(\Delta P/P) = M_x(\overline{x/\theta})\left(\frac{1}{B}\frac{dB}{dx}\right)\delta\theta_f$$

For our system $M_x = 0.8$ and $(\overline{x/\theta}) = 0.7$ cm/mr, so if the angular measurement uncertainty $\delta\theta_f$ is 1 mr, then a gradient of 1 G/cm at 15 kG yields:

$$\delta(\Delta P/P) = \frac{0.8(0.7)(0.1)}{15,000}1.$$

$$= 1/27,000$$

In other words, field gradient of as much as 1 part in 15,000 per cm can be tolerated in the dipoles if the focal plane is measured to 1 mr uncertainty and the magnitudes of these gradients are measured [No81a].

When the design goal is a gradient specification instead of a flatness requirement, the iron can be driven into saturation. Superconducting coils, with their higher current densities, provide cheap amp-turns, allowing reduced iron mass and larger dipole gaps (increased solid angle). When one already has a liquid helium refrigerator and the superconducting magnet experience, the choice is much easier still. The saturation level of the yoke has been kept low enough to avoid stray fringing fields which may interfere with detectors near the target.

The simplest configuration is a window frame with a compact superconducting coil. This was the first extensively studied design [Ze79, Ze80, Ze81a], which although it gives the most compact design for a given volume of good field (a gradient of ± 1 G/cm), it requires a complex superconducting saddle coil. We have chosen to concentrate on the alternate magnet type, the H-frame. Two strategies were used to maximize the region of good field: (1) improving the infinite permeability solution, and (2) improving the finite permeability solution. The infinite permeability solution is improved by the addition of a trim coil on the median plane with current in the same direction as the main coil. Because the field in the H-frame magnet decreases as the edge of pole tip is approached, a coil on the median plane has the effect of keeping the field from decreasing as rapidly. The addition of the return coil directly above, on the pole tip, also improves the field profile and makes assembly easier. The trim coils are normal conductors, carrying approximately 0.7% of the main coil ampere-turns.
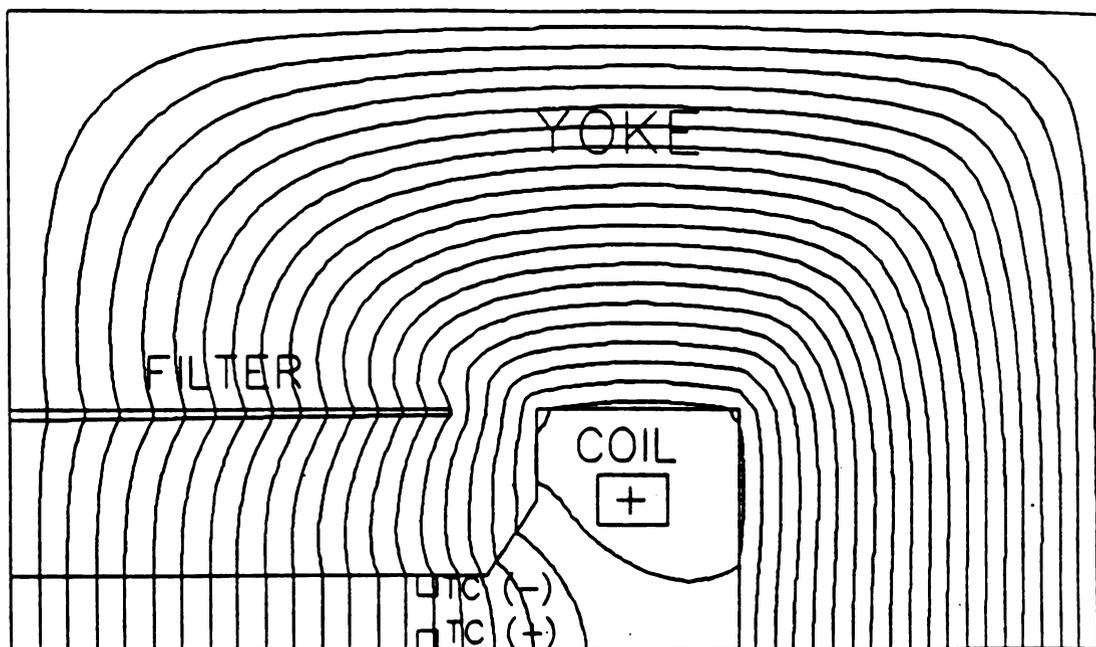
Figure 3.1: S800 H-frame dipole POISSON calculation.

The field profile is kept reasonable over a wide dynamic range (with finite permeability) by using a tapered gap behind the pole tip which is 1 cm high at the midline and 1/2 cm at a distance of 40 cm . It does not extend all the way across the pole. The basic design is shown in Fig. 3.1 and Fig. 3.2. Fig. 3.1 shows a calculation for 1.5 T and Fig. 3.2 gives the basic dimension. The dipole bending limit gives K=800 MeV for the central ray at a field of slightly less than 1.5 T, but the dipoles can be run up to fields of 1.6 T if necessary for slightly more rigid particles.

The effects of the trim coil at low field where the iron is closest to infinite permeability is seen in Fig. 3.3 and Fig. 3.4. The degree of field uniformity at 5 kG

for several trim coil settings are shown in Fig. 3.3. The volume of good field needed is out to 35 cm. The optimized trim coil current is 0.7 % of the main coil. The infinite permeability solution is also shown for comparison, required for the infinite permeability case. The permeability curve used in the calculations is for 1003 iron, supplied by the vendor (Japan Steel). Fig. 3.4 shows the gradients for the same cases.

For field levels where significant saturation of the iron occurs, as around the normal 1.5 T range, the effects of the filter are seen. The filter is tapered to provide a variable reluctance so that the field stays uniform with increasing excitation. It is seen in Fig. 3.5 that the volume of good field has been increased by several centimeters by the combination of trim coils and filters. This is seen more readily in Fig. 3.6, which shows the gradients for the same cases. Note that the infinite permeability case has trim coils turned on.

Since the operating range of the dipoles is designed to be from 0.5 to 1.6 T, the magnet must meet the gradient requirements at all excitations. The gradient requirements are actually a percentage of central field, ie., 1 G/cm at 1.5 T, 0.33 at 0.55 T, and 1.06 at 1.6 T. The field profiles are shown in Fig. 3.7. With the corrections described the dipole meets the gradient requirements.

In order to insure reliable operation of the superconducting coils, a low current density, cryostable coil configuration was chosen. A current density of about $4 \, kA/cm^2$ (about the same as the NSCL K1200 cyclotron) will be used. Although this is considerably less than the $18 \, kA/cm^2$ used in the beamline dipoles, the stored energy is much greater. The $\pm 16°$ dipoles have only 35 kJ, while each S800 dipole has 1.1 MJ. The magnetic field in the coil package of the S800 never exceeds the gap field. The choice of a cryostable coil, while it should never quench since the Steckley parameter is < 1 [Re83], does require the use of a dump resistor to protect the coil in case of a massive heat pulse sufficient to remove all the liquid helium. Both the K500 and
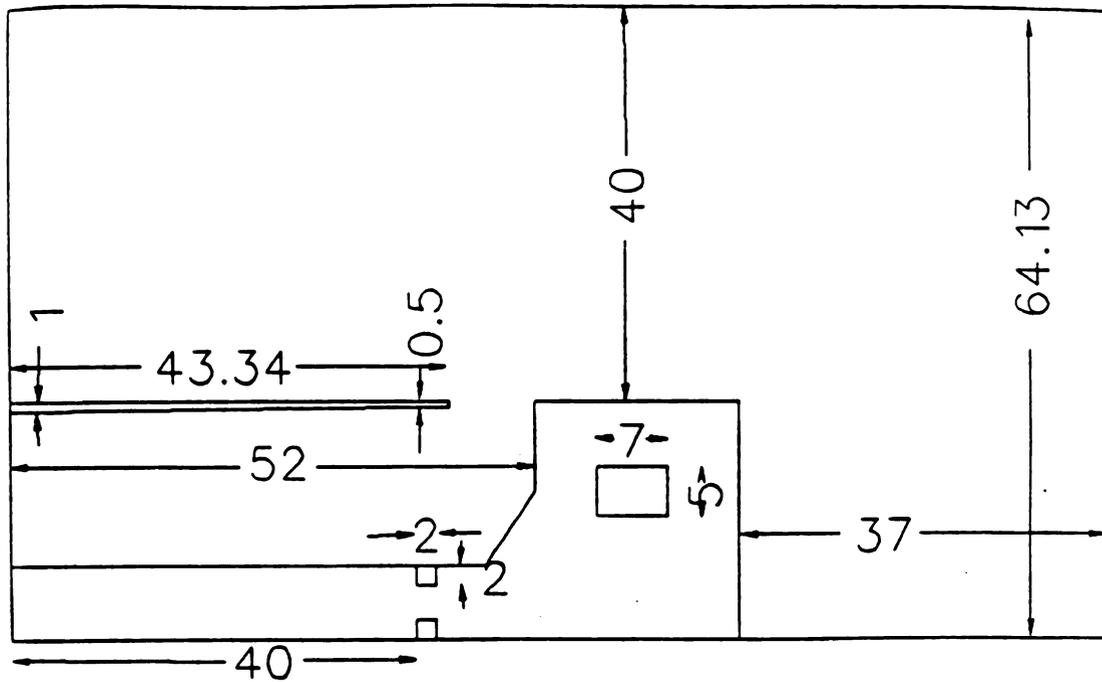
Figure 3.2: S800 dipole showing dimensions in cm.

K1200 cyclotrons are equipped with a fast dump (emergency) and a slow dump resistor for energy removal. Quench calculations have been done which show the coils will survive a quench when the dump switch is used in a timely manner [Ze86]. In this case, the calculated hot spot temperature is only 75 K. Additionally, the dump should not cause a quench. This has been experimentally verified by high current dumps. A summary of the coil and wire specifications is given in Table 3.1.
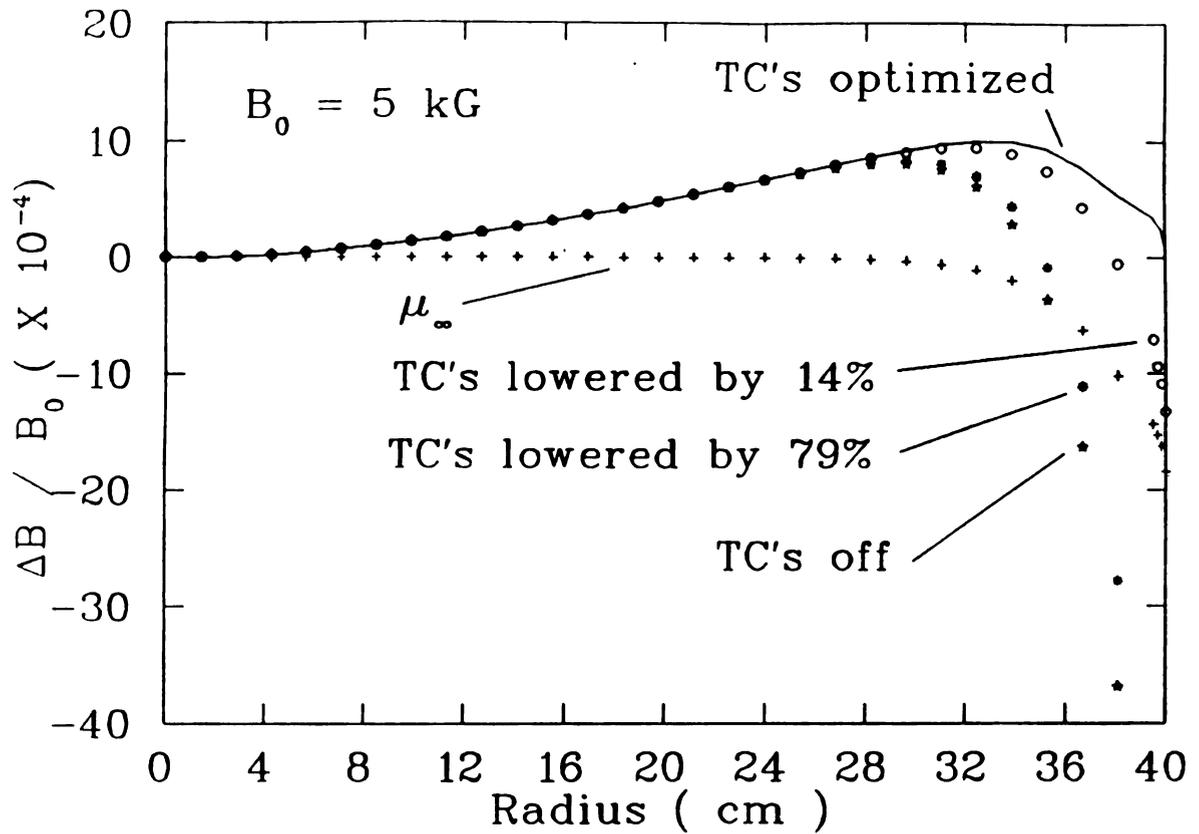
Figure 3.3: Deviations of the field from the central field at low field as a function of charge in trim coil currents.
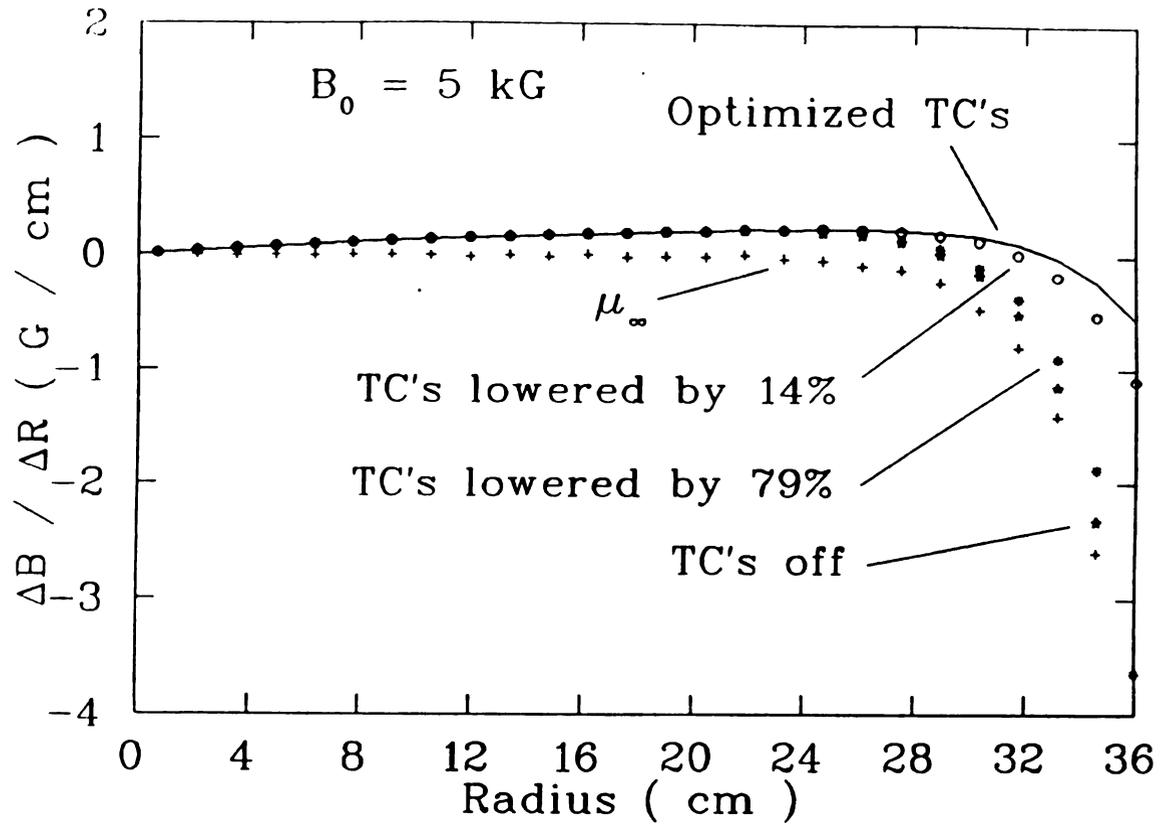
Figure 3.4: Deviations of the gradients from the central field at low field as a function of charge in trim coil currents.
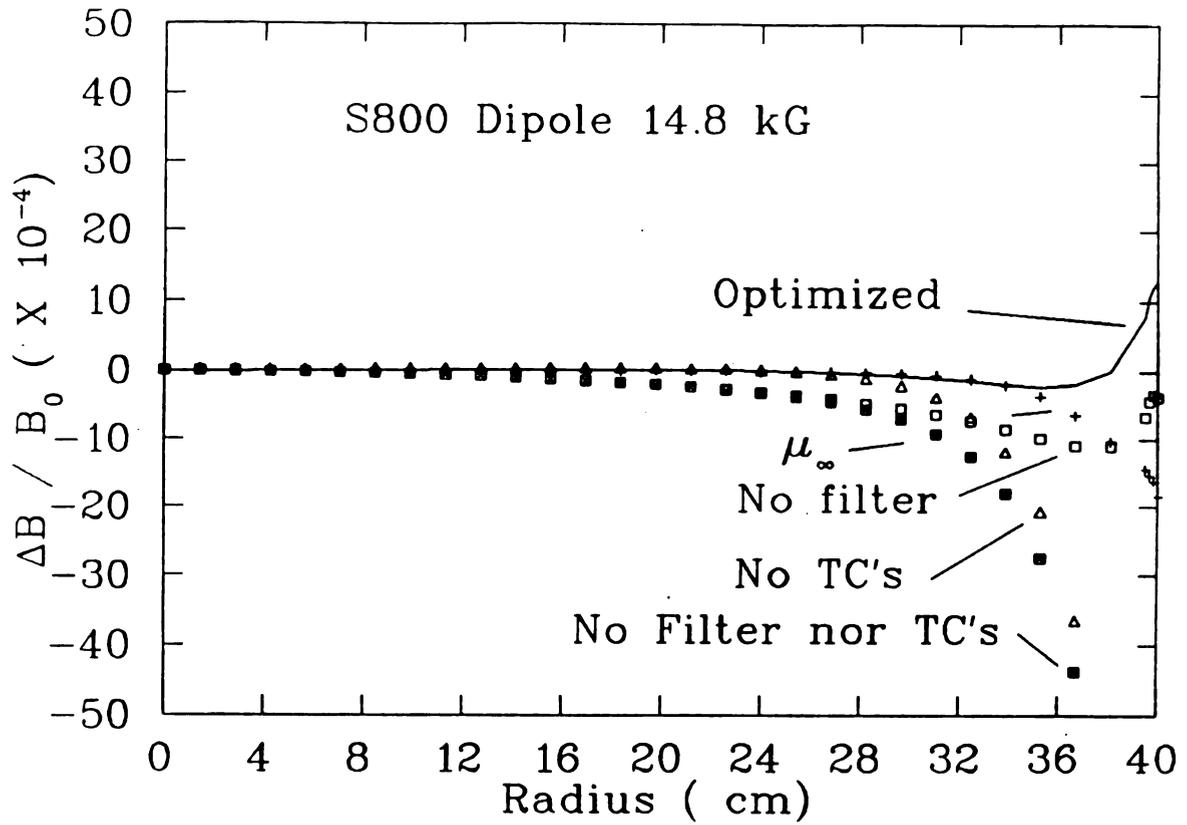
Figure 3.5: Deviations of the fields at 14.8 kG for several cases showing the effects of trim coils and filters.
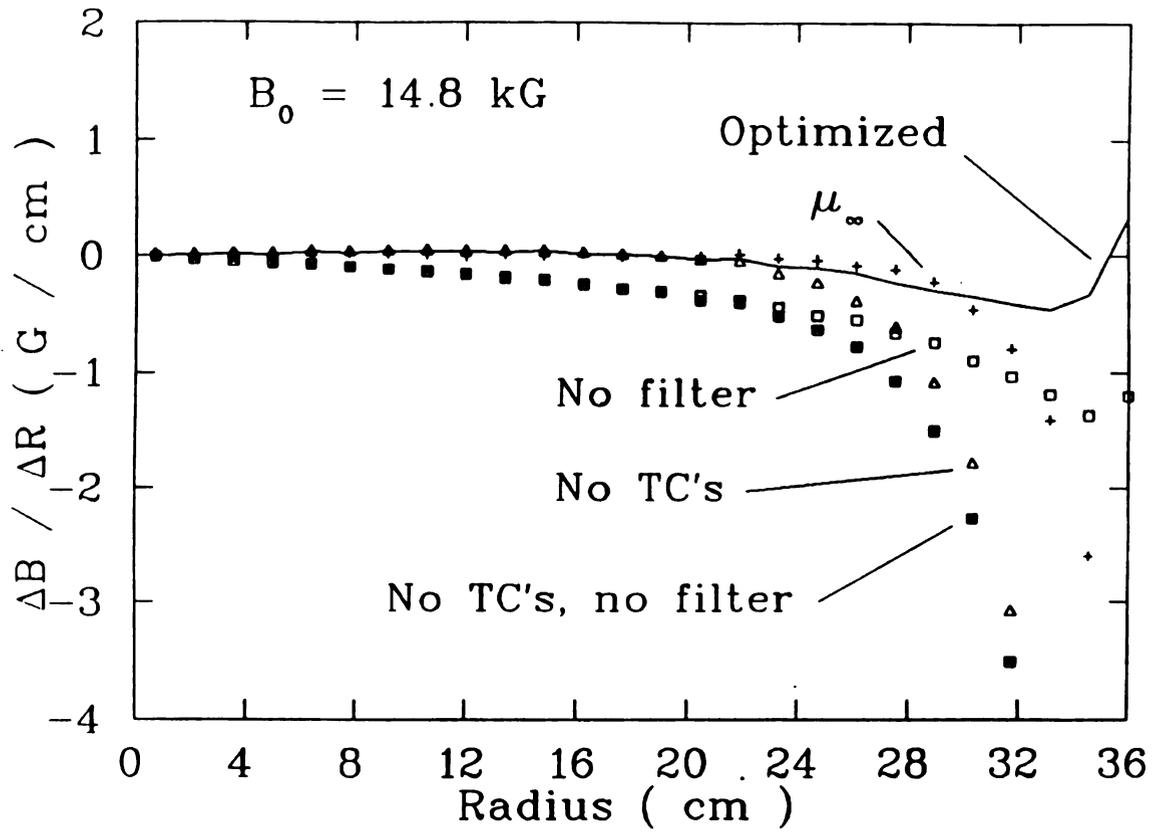
Figure 3.6: Deviations of the gradients at 14.8 kG for several cases showing the effects of trim coils and filters.
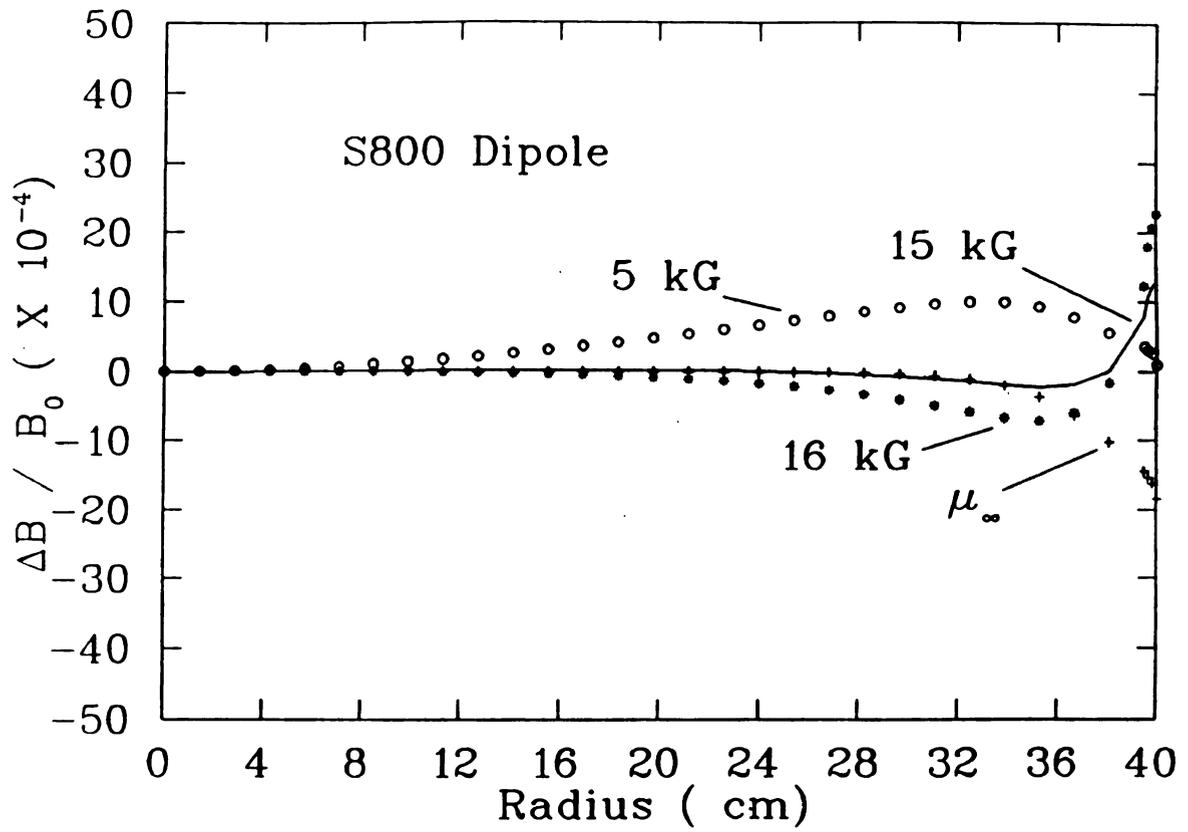
Figure 3.7: Deviations of the fields over the dynamic range needed for spectrometer operation.
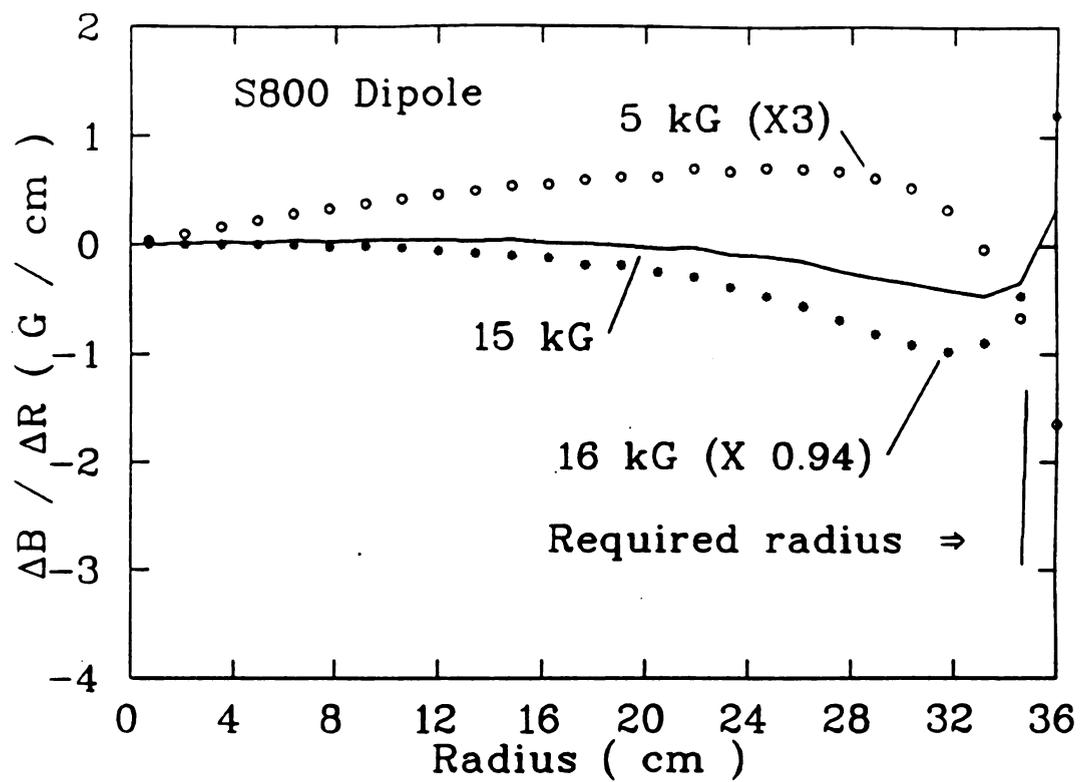
Figure 3.8: Deviations of the gradients over the dynamic range needed for spectrometer operation, scaled to the 1.5 T field.

Table 3.1: S800 dipole conductor and coil specifications.

Conductor	
type: Copper to Superconducting Ratio: Size: I_{crit} @ 2 T I_{oper} @ 1.6 T central field	NbTi in copper matrix 15:1 1.981 × 3.25 mm² measured as ≥ 1400 A 420 A
Coil	
Number turns per coil : Weight of conductor per coil: Inductance: Stored energy: Protection resistor:	350 250 kg 10 H 1.1 MJ 0.25 Ω

3.3 S800 Dipole Construction

Because the cost of the spectrometer is strongly determined by the mass of the dipoles, the size must be kept to a minimum, consistent with the required good field region. Additionally, as the spectrometer is designed to disperse in the vertical plane, a lighter set of magnets means the support structure does not have to be as massive. Minimizing the mass requires the construction of a dipole with coils that follow the beam sagitta, that is, a kidney shaped magnet. The result is a coil with one negative curvature side. We have kept the number of turns to a minimum, consistent with liquid helium consumption and power supply costs. This necessitates going to a cryostable coil for this relatively low field (1.6 T in the gap) device and running at higher current (420 A) [Ze93].

The coils of the dipoles have 350 turns, arranged in 28 layers. Layer-to-layer climbs are made alternately on the straight ends. This results in 12.5 turns per layer. Insulation for each layer is provided by winding the turns into slots machined in thin G10 pieces. Cross cuts and small gaps between pieces provide additional helium

passageways and flexibility in going around corners.

Winding the negative curvature side of the coil is difficult because any tension in the winding pulls the wire out of its insulation groove. The first few layers can be done by first clamping the wire at the corner then passing the wire around a cylinder to form it to the right curvature. The wire can then be rolled into the grooves. It can then be clamped at the other end to hold it in place. However, after a few layers the accumulated tension begins to separate the layers. We have solved this problem by the straightforward method of using many clamps along the negative curvature side. More clamps are required for the additional layers because of the accumulated tension which makes the coil package act like a big spring. A pneumatic arm is used to keep the same force on the coil regardless of coil thickness to which is attached a roller for the negative side. This roller bends the wire to the required radius so that the wire lays in the groove. The clamps are removed ahead of the arm and replaced after it has gone by. The procedure requires two people to operate efficiently. In addition to winding, insulation strips and climb pieces must be positioned, resulting in taking nine hours per layer.

Because of the manufacture's wire lengths, two or three splices were made in each coil. These are accomplished by milling one half of the width of each piece for a length of two twist pitches (about 6 cm) and soldering them together so that the width and height are the same as the original conductor. Added cross channels in the G10 insulation pieces are used near the splices to ensure that any helium vapor bubbles formed can escape. A test joint showed a resistance of ≤ 2 nΩ.

Once all layers have been wound, nonmagnetic spring assemblies are placed on the outside of the coil. These provide for thermal contraction compensation and to compress the coil to prevent movement when the coil is energized. Assembly of the outer wall and top of the bobbin on the negative side necessitates the removal of all

of the clamps at once. Fortunately, it was found the time constant for loosening of the coil after it has been clamped for several days is about two hours. Therefore, it is possible to remove all the clamps, place the covers in place and re-clamp them before the coil relaxes. After carefully welding the first coil closed, it was leak checked and the bobbin prepared for winding the second coil.

Since the magnet operates at a relatively low field, the magnetic field shape is predominately determined by the iron, with coil contributing only twenty percent even at high field. However, the field uniformity requirement is one part in a thousand, so coil placement cannot be neglected. The shape of the coil is such that forces are much larger on one side of the arc than the other, and the bobbin is not stiff enough to resist excessive deflections on it own. The deflections of the bobbin, which is a box structure of 1.9 cm thick 316 Stainless Steel, would result in asymmetries in the field if they were not properly restrained. Three dimensional force calculations were used to determine the required support structure [Ze92] and more support links were used than would be required to simply restrain the bobbin. A set of five tension links and a compression link is used to minimize deflection in the radial direction. Smaller pairs of links at each corner support any axial force due to off centering across the median plane.

The tension links are constructed from S-glass unidirectional tape. Because of the stress concentrations in the bushings and attachment points due to the small space requirements, titanium (Ti-6Al-4V ELI) was used for these parts. The links have been tested to beyond the maximum calculated loads. Additionally, each link assembly is proof tested to at least its calculated load. The compression link is made of a Randolite PD43 tube with Ti fittings. To insure the link would not fall apart if it went into tension, a small Ti rod holds the link assembly together. This link has also been extensively tested. At the room temperature end of the links is a spherical

bearing, which combined with the orthogonal clevises at the coil end, takes up the motion during cool down. The calculated heat load at 4 K from all the links is less than one watt.

The S800 dipole magnet consists of five major pieces: the two top slabs, the inner and outer side yokes and the pole tip assembly. The pole tip assembly is made up of the pole tips , which are connected together with precision stainless steel spacers, and the coil cryostat. The cryostat was handled as a unit. With the carriage in place on the track, first one of the top slabs was lowered into 10 meter deep pit and attached to the supports. Next, the bottom side yoke was mounted to the top slab. The pole tip/cryostat assembly was then carefully lowered into position and moved to the top slab. Because the compression support link on the negative curvature side has to stick out of the inner side yoke, a key way was cut in the inner yoke. The inner yoke was then slid into place on the assembly. The clearance between the support structure and the link assembly did not allow the remaining top yoke slab to be simply lowered into place, so another crane was placed into the pit to pick up the now connected four pieces (50 t). Then the in house 40 t crane picked up the last top slab while the other crane lifted the other assembly straight up. Then both were brought close together and lowered at the same rate. They were then bolted together to complete the assembly. Once all the pieces were in place, the lead/dewar box was connected to the magnet. The liquid helium feed circuit brings liquid through a heat exchanger at the top of the magnet before delivering high quality liquid into the bottom of the coils. Each coil is fed separately and the overflow fills the dewar to provide cooling for the incoming liquid. Liquid nitrogen is supplied at the bottom of each side (the inner and outer arcs) and conducted through 0.95 cm diameter copper tubing soldered in a serpentine path along the shield. Aluminum tape provides the necessary thermal radiation protection between 4 K and 77 K [Ze94]. Superinsulation is used between

the nitrogen shield and the cryostat walls. The current leads consist of five strands each of a cabled superconductor (147 wires of 0.25 mm diameter).

The power supply is capable of providing 600 A at ±20 V. The nominal current for the maximum field of 1.6 T is about 420 A. However, the current leads and the support links are capable of operating at 468 A for peak field of 1.7 T [Ze95a]. Although the magnetic field profile at this field will not be good enough to allow the full solid angle and momentum acceptance to be used, it will allow more rigid beams to be analyzed. Coil protection is achieved with a 0.25 Ω dump resistor which is activated when a potential difference between the coils of greater than 0.5 V is detected. Additionally, the dump switch is activated if the helium vessel rupture disk is used.

3.4   Commissioning of the S800 Dipole Magnets

During final leak checking, and before the first magnet cryogenic connections were completed, a small helium leak on the bobbin was discovered. Since disassembly of the magnet to try to find and fix the leak would result in a six month delay, the pumping option was accepted. It was felt the leak was small enough to allow operation of the magnet, so two holes were added to the dewar box and the cryostat to allow the placement of vacuum pumps. The magnet was then cooled down successfully, although the heat load was twice as high as anticipated. After adjusting the support links, the magnet successfully ran to the required central field of 1.6 T. No training nor unbalanced coil voltages were observed. All support links were well below their limits and their loading agreed well with calculations. The field of the first dipole as a function of coil current in the 15 cm gap is shown in Fig. 3.9. The fields were measured with a Hall Gaussmeter, and later confirmed with NMR. The maximum field of 1.6 T is achieved at 420 A, while the current estimated to give this field based

on two dimensional POISSON calculation is 498 A. Three dimensional calculations were not used to estimate the transfer function because the tapered "Purcell filter" could not be put in the calculation due to node limitations. The discrepancy between the POISSON calculations and the measured data could be the result of an under-estimation of the saturation magnetization or because the truly three dimensional structure of the iron yoke: The inner and outer side yoke have different areas to keep the saturation constant of either side of the middle. However, more iron is available to return the flux, due to the longer length of the outer slab. Therefore, a lower level of saturation is achieved and hence, less current is required to achieve the higher fields. The magnet is designed to have significant saturation, so that the expected gradient in the field is constant over the operating range of 0.5 to 1.6 T. This satura-tion, together with the tapered filter provide the required field quality. Measured and POISSON calculations of the deviations of the field gradient are shown in Fig. 3.10 [Ca]. The deviations of the mapping field gradients are less than 1 Gauss/cm which reached the spectrometer requirements. More field mapping results of D1 and D2 will be in J. Caggiano's thesis.

In order to try to reduce the heat load due to the helium leak, the magnet was warmed up and more pumping was added. Additionally, holes were cut through the superinsulation blanket to reduce the pumping impedance from the bobbin to the pumps. The magnet was again been cooled down. The insulation vacuum is now improved, but the heat load is still high although it should be sufficient for operation. It is possible that part of the heat load is due to the nitrogen shield making contact with the bobbin in some location. Since the shield has its own support links, it can be adjusted independent of the bobbin, which must be adjusted to optimize the field quality and minimize the forces. The heat load of the first dipole magnet is 12 W. Fig. 3.11 shows the heat load as a function of helium background pressure in the

cryostat.

Based upon our initial operating experiences with the first dipole, D1, some small modifications were made to the second dipole, D2, during its assembly. The cavities in the bobbin on either long, curved side between the two coils were left open to the insulating vacuum on D1. Concerns about the potential of helium leakage from the coil packages into this space caused these volumes to be sealed and lines run to allow independent evacuation of the these spaces on D2. Also, a number of G-10 composite bumpers were added to the surface of the bobbin to prevent any possibility of direct contact between the 4 K bobbin and the 77 K nitrogen shield around it. The heat load of the D2 magnet is only 5.5 W.
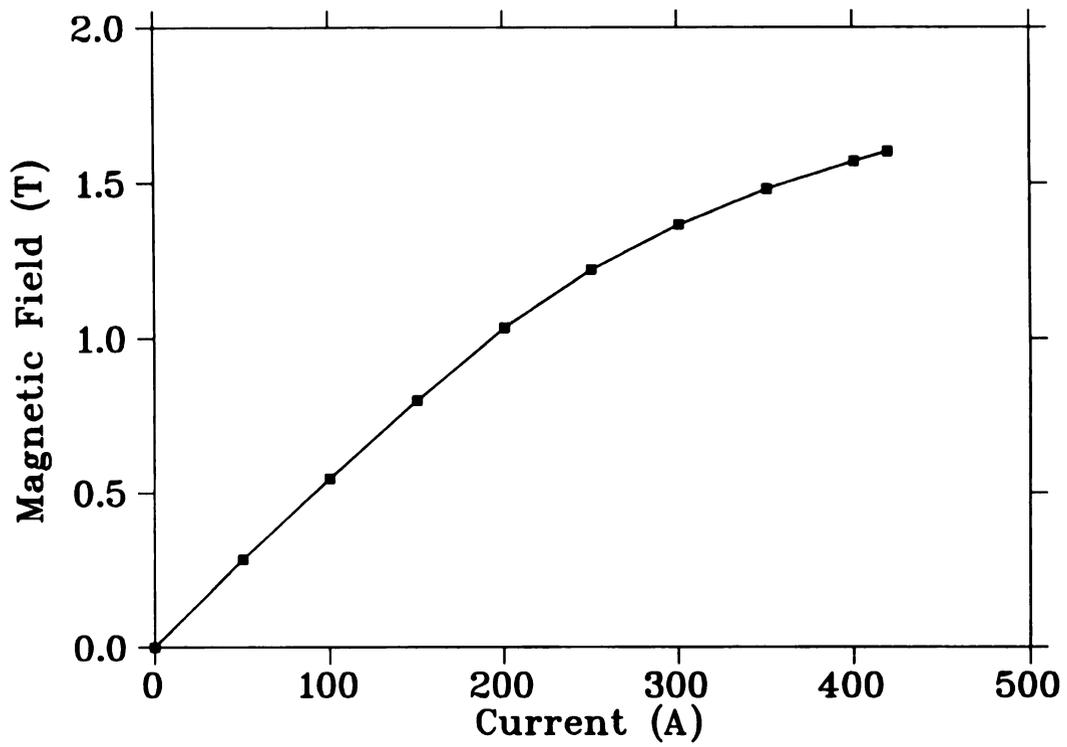
Figure 3.9: Central magnetic field as measured by a Hall Gaussmeter as function of current.
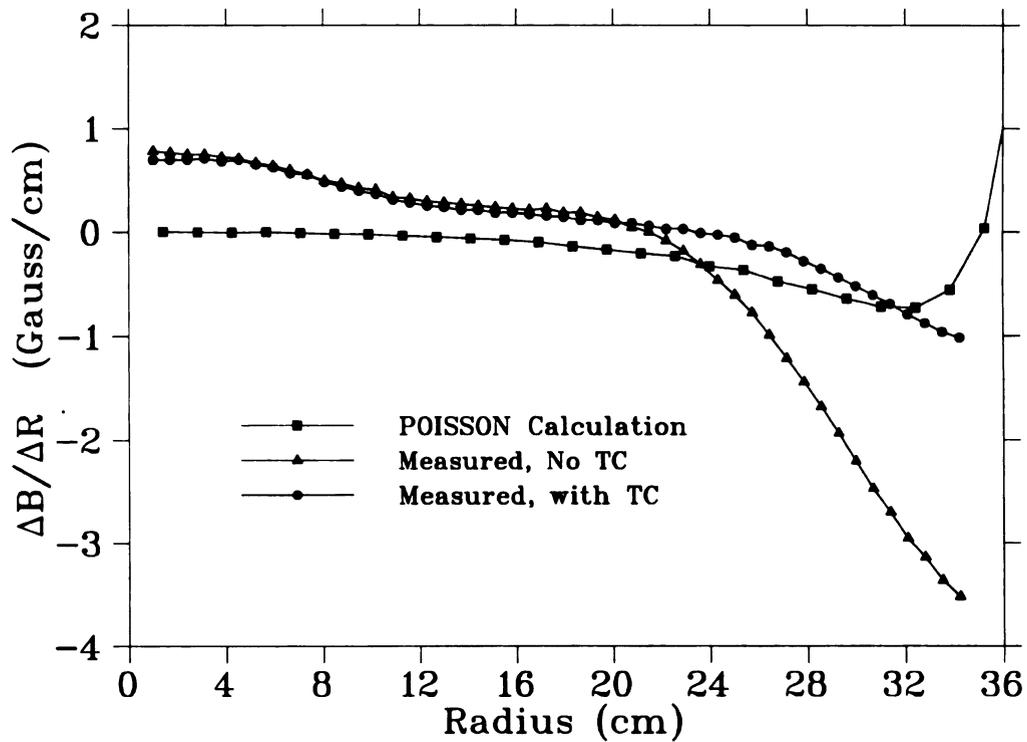
Figure 3.10: Measured and POISSON calculation deviations of the field gradient with trim coil on and off. The data were measured at the center of D1 as a function of radius.
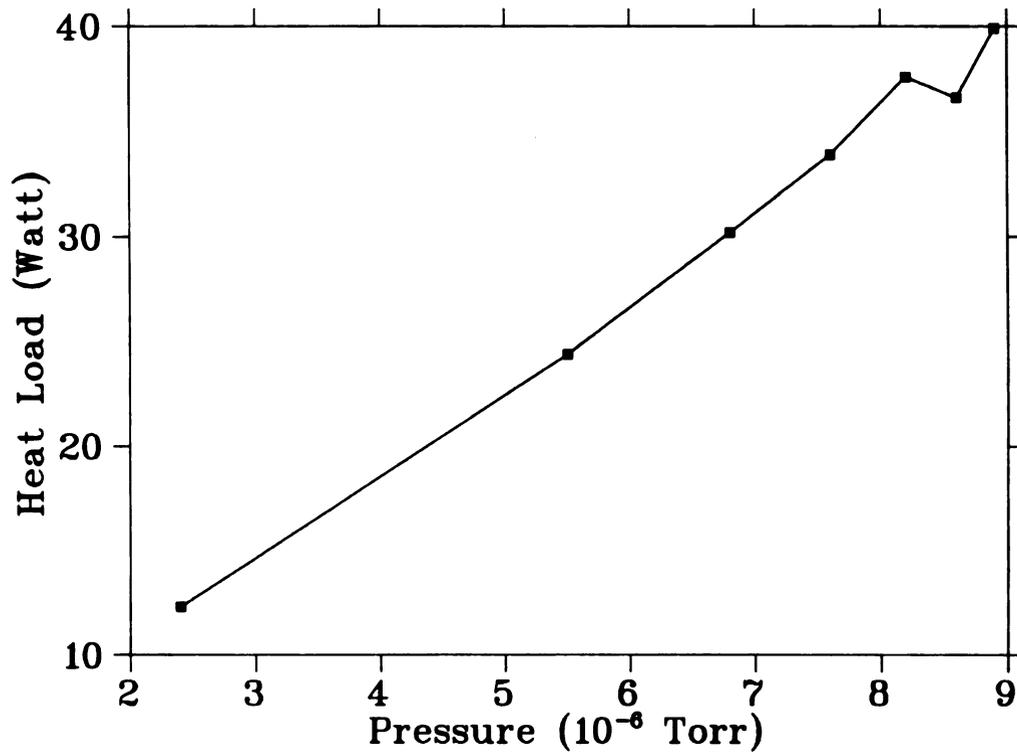
Figure 3.11: The heat load of the first dipole magnet as a function of insulation vacuum pressure.

Chapter 4

Design and Construction of High Gradient, Large Aperture Quadrupoles for the S800

4.1 Magnetostatics of quadrupoles

From the Biot-Savart law of magnetostatic we find

$$\nabla \cdot \mathbf{B} = 0 \tag{4.1}$$

$$\nabla \times \mathbf{B} = \frac{4\pi}{c} \mathbf{J} \tag{4.2}$$

where $\mathbf{B}$ and $\mathbf{J}$ are the magnetic field and the current density. The current density is zero inside quadrupoles, therefore $\nabla \times \mathbf{B} = 0$ permits the expression of the vector magnetic induction $\mathbf{B}$ as the gradient of magnetic scalar potential and hence, $\mathbf{B} = -\nabla \, \Phi_M$. Then the basic differential laws of magnetostatics reduces to the Laplace equation for Φ_M, namely

$$\nabla^2 \Phi_M = \frac{1}{r} \frac{\partial}{\partial r} \left(r \frac{\partial \Phi_M}{\partial r} \right) + \frac{1}{r^2} \frac{\partial^2 \Phi_M}{\partial^2 \theta} + \frac{\partial^2 \Phi_M}{\partial z^2} = 0 \tag{4.3}$$

Cylindrical coordinates have been chosen since they are most suitable for quadrupole magnet geometries. We attempt a solution by the method of separation of variables

and assume that

$$\Phi_M(r,\theta,z) = R(r)\Theta(\theta)Z(z) \tag{4.4}$$

Then, upon substituting this expression into eq. (4.3) the complete solution in cylindrical coordinates becomes [Ma65]

$$\Phi_M(r,\theta,z) \sim \sum_{m,n}[A_{mn}J_n(kr) + B_{mn}N_n(kr)]e^{\pm in\theta}e^{\pm kz} \tag{4.5}$$

where

$$J_n(kr) = \left(\frac{kr}{2}\right)^n \sum_{m=0}^{\infty} \frac{(-1)^m}{m!\Gamma(m+n+1)}\left(\frac{kr}{2}\right)^{2m} \tag{4.6}$$

is a Bessel function of order n and $N_n(kr)$ is a Neumann function of order n. Since Neumann functions become $-\infty$ at r=0, we choose only the $J_n(kr)$ to treat problems which involve the origin. The values of n, m and k are in principle arbitrary, although n must be an integer (or zero) in order to insure the singlevaluedness of $\Theta(\theta)$. There are an infinite number of solutions which, apart from an arbitrary angular phase and assuming that z=0 is the center of a quadrupole magnet, may be written as [Na91]

$$\Phi_M(r,\theta,z) = \sum_{n=0}^{\infty} sin(n\theta)\Phi_n(r,z)$$

$$= \sum_{n=0}^{\infty}\left\{sin(n\theta)\left(\frac{r}{r_0}\right)^n \sum_{m=0}^{\infty}\left[\frac{b_{m,n}(z)r_0}{2m+n}\left(\frac{r}{r_0}\right)^{2m}\right]\right\} \tag{4.7}$$

where r_0 is the pole radius. (If $k = 0$, then there is no dependence on z and the Laplace's equation becomes two dimensional case. Φ_M is just proportional to $r^n sin(n\theta)$.) In cylindrical coordinates, the radial component of the magnetic field is

$$B_r(r,\theta,z) = -\frac{\partial\Phi_M}{\partial r}$$

$$= -\sum_{n=0}^{\infty}\left\{sin(n\theta)\left(\frac{r}{r_0}\right)^{n-1}\sum_{m=0}^{\infty}\left[b_{m,n}(z)\left(\frac{r}{r_0}\right)^{2m}\right]\right\}$$

$$= -\sum_{n=0}^{\infty}sin(n\theta)B_{r,n}(r,z) \tag{4.8}$$

where

$$B_{r,n}(r,z) = \left(\frac{r}{r_0}\right)^{n-1} \sum_{m=0}^{\infty} \left[b_{m,n}(z)\left(\frac{r}{r_0}\right)^{2m}\right] \tag{4.9}$$

The n=2 term corresponds to the quadrupole component of the magnetic field and has a sin(2θ) angular dependence. By Fourier analyzing a magnetic field, it is possible to extract each multipole component of the magnetic field, which is used to judge the quality of the field.

For an ideal quadrupole, $B_{r,2}$ would be proportional to r and would have no z dependence inside a quadrupole magnet. Outside the quadrupole magnet, $B_{r,2}$ would be zero, and $B_{r,n}$ would be zero everywhere for n$\neq$2. However, there is always a gradual decrease in the field near the end of the quadrupole magnet, and it is impossible to completely remove every higher order multipole, so the main goal for the design of the quadrupole magnet is primarily to attempt to minimize the higher order multipoles, while maximizing the quadrupole term of the magnetic field. With perfect symmetry, not every term in the magnetic field expansion is present. The quadrupole magnet has fourfold symmetry and

$$\Phi_M(r,\theta,z) = -\Phi_M(r,\theta + \pi/2, z)$$

so only the n = 2, 6, 10, 14, $\cdots$ 2(1+2k) terms are allowed. Substituting equation (4.7) into equation (4.3) and using the orthogonality relation, we obtain

$$\frac{(2m+n)b_{m,n}(z)}{r_0^{(2m+n-1)}} - \frac{n^2 b_{m,n}(z)}{(2m+n)r_0^{(2m+n-1)}} + \frac{1}{(2m+n-2)r_0^{(2m+n-3)}}\frac{d^2 b_{m-1,n}(z)}{dz^2} = 0$$

This equation yields [Ha96]

$$b_{m,n}(z) = -\frac{2m+n}{4m(m+n)(2m+n-2)}\frac{d^2 b_{m-1,n}(z)}{dz^2} \tag{4.10}$$

where m $\geq$ 1. From equation (4.5) we know that $b_{m,n}$ are linear combinations of e^{kz} and e^{-kz} which meets the boundary condition. The z component of the magnetic field, $B_z(\text{r},\theta,z)$, must vanish at $z = 0$ and $z = \infty$ or

$$\frac{db_{m,n}}{dz} = 0 \quad at \quad z = 0 \quad and \quad z = \infty \tag{4.11}$$

Since the spectrometer mainly depends on the integrals of the transverse components along a path parallel to the beam axis, we have

$$\int_0^\infty B_{r,n}(r,z)dz = \left(\frac{r}{r_0}\right)^{n-1} \sum_{m=0}^\infty \left(\frac{r}{r_0}\right)^{2m} \int_0^\infty b_{m,n}(z)dz$$

and using equation (4.10) and (4.11), we find that only the $m = 0$ term contributes. Therefore,

$$\int_0^\infty B_{r,n}(r,z)dz = \left(\frac{r}{r_0}\right)^{n-1} \int_0^\infty b_{0,n}(z)dz \tag{4.12}$$

which shows that the integral is proportional to r^{n-1}, and that only the leading term of the integral in the radial expansion is important.

4.2   Quadrupole types

Quadrupole magnets are the primary focusing elements in an accelerator beamline. The design for the high resolution spectrometer at the NSCL requires two quadrupole magnets, Q1 and Q2. These magnets are required to have high field gradients and large apertures as compared with typical beamline magnets. Room temperature magnet designs were found to be too power hungry and could not have been fit within the space available. This necessitated the use of superconducting magnets.

The choice of superconducting quadrupoles is limited to three basic types: a) cos(2θ) type, where the field is shaped by the coil, b) Panofsky type [Ha59], which

is a square or rectangular current sheet approximation, and c) iron dominated type (also called superferric) [Ze84], where the field is shaped primarily by the iron pole tip.

4.2.1 Cos(2θ) quads

Cos(2θ) quads, which produce highly uniform gradients of up to 50 T/m over a large volume, have been built [Co83] at Fermi Lab, CERN and other places. However, this type is convenient only if the conductor is a flat cable (approximating a current sheet) which requires high current operation (1,000-5,000A). Vapor-cooled current leads for 1,000 A consume liquid helium at a rate of 2.8 litres per hour. In recent years, Cos(2θ) magnets have been used as spectrometer elements at CEBAF's experimental hall A [Al95]. One of the quadrupoles has a 30 cm warm bore and a 1.6 m length. The peak gradient of 8.3 T/m is produced by epoxy-impregnated coils operating at 3250 A. The maximum stored energy is 130 kJ and the effective length is only 92 cm. The other two quadrupoles have 60 cm warm bores and 3 m lengths, which have used a 3 sector, 2 layer coil construction operating at a peak current of 1850 A. The stored energy is 592 kJ and the effective length is only 1.8 m. Each of the Cos(2θ) quadrupoles costs about 1.1M$. Engineering and construction of a Cos(2θ) magnet was considered to be quite expensive. In addition, they have an effective length less than their physical length, requiring even higher field gradients to offset this condition.

4.2.2 Panofsky quads

The Panofsky quad, while easy to build, suffers from two problems. First, the field in the corners of a square quad is $\sqrt{2}$ times the field at pole faces. The means that the superconducting wire parameters are dominated by a region of wasted field. The second problem is that Panofsky quads which have been built have achieved the

desired field uniformity only by very careful construction and attention to where each individual wire is placed.

4.2.3 Iron dominated quads

The third type of superconducting quadrupole is the iron dominated quad which was developed for the NSCL standard beamlines. It differs from the other two in that the field shaping is done primarily by iron poles; in this sense it is similar to classical iron dominated quadrupoles but with some important differences. The resulting iron and coil cross section and calculated field lines are shown in Fig. 4.1 for a 12.7 cm inside diameter quad. The fraction of useful bore of this magnet is quite good when compared to room temperature magnets. Mathematically this performance can be understood by conformal mapping this and the standard geometries into equivalent dipoles. In the infinite permeability limit, a window-frame dipole produces a perfect field up to the coil, and such a dipole conformally mapped into a quadrupole geometry is also perfect. This is not true for the H dipole magnet; typically, 0.5 to 0.75 gaps are lost inside of the pole edge with a commensurate loss in the mapped quadrupole. Room temperature magnets are forced into the mapped H geometry by virtue of the large number of ampere-turns needed by the typical magnet and the limited current density available with copper. The magnets simply need the space to get all the ampere-turns packed in. The pole fields are also limited by saturation of the iron. The pole does not grow in cross section to contain the additional flux which enters it with increasing radius; in some magnets the cross section even decreases in order to permit a large coil to be used. The mapped window-frame magnet does not suffer from this disadvantage since the pole cross section increases until the return iron is reached. According to conformal mapping, the coil surface should be hyperbolic and the current density would not be uniform. Since an accurately non-uniform current
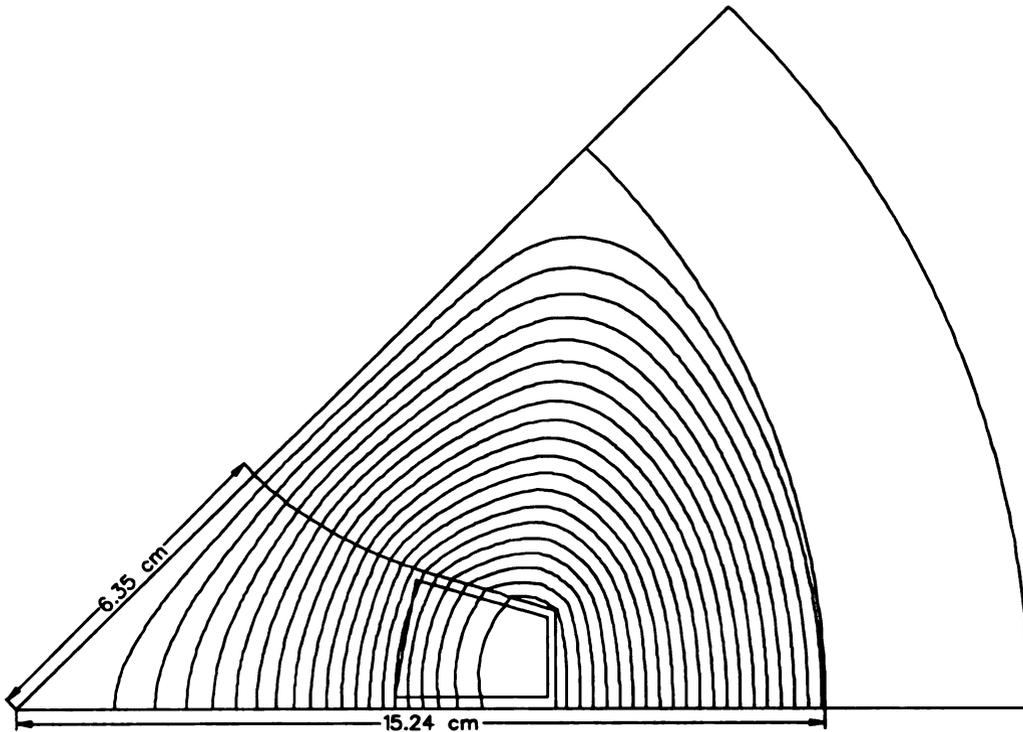
Figure 4.1: Octant of the NSCL beamline quadrupole with magnetic field lines using the POISSON code.

density coil would be difficult to achieve, the nonuniformity is compensated for by repositioning the exposed surface of the conductor.

4.3 Physical parameters of Q1, Q2 and a sextupole as related to the S800

We decided against $\cos(2\theta)$ quadrupoles because of the high current operation and its helium requirements. We also investigated superconducting Panofsky quadrupoles. A Panofsky design was not chosen due to the sensitivity of the field quality to er-

Table 4.1: The physical parameters of Q1 and Q2 magnets.

Item	Q1	Q2
Length of iron	0.34 m	0.30 m
Pole tip diameter	0.24 m	0.42 m
Peak gradient	19.7 T/m	7.5 T/m
Effective length (nominal)	40 cm	40 cm

rors in conductor placement and the construction problem. Our conclusions from these studies and from experience with our cold-iron, iron dominated superconducting beamline quads is that a larger version of the latter type is our choice for both Q1 and Q2 quadrupoles. The design goals and physical parameters of Q1 and Q2 magnets are summarized in Table 4.1.

According to the beam optics calculation for S800 spectrometer, the dominant aberration in the focal plane is x/θ^2. This results in a very large line width, even in the absence of any momentum spread. Sometimes it is desirable to physically stop intense elastically scattered particles just before the detector, while permitting low-lying excited states to pass. A sextupole has been used to correct the x/θ^2 term. The best place for the sextupole is in Q2.

4.4 Magnetostatic calculations

4.4.1 Magnetic field calculation of Q1

The original Q1 design was based on two dimensional magnetic field calculations performed with POISSON. Q1 is a large version of the NSCL's standard cold beamline quads. The beamline quadrupole pole tip radius is 6.35 cm and Q1 is 12 cm. A sketch of one eighth of this design is shown in Fig. 4.2. However, the compromise coil design and the finite length that include the coil return at the ends may introduce significant

higher order multipoles to the field, even with ideal placement of all components. The end effects were studied with a three dimensional magnetostatic code, TOSCA [To]. We used six 20-node bricks and two straight bars to model the Q1 coil [Zh96]. The cross section shape of the straight bar is same as in Fig. 4.2. Since the cross section of the NSCL standard beamline quad coil end is irregular in shape, it is impossible to precisely model the real coil end using TOSCA. We used three 20-node bricks to approximately model the end of Q1 coil and kept the cross section area of the 20-node brick coil the same as the straight bar's. The coils and iron are shown in Fig. 4.3.

The code TOSCA computes three-dimensional magnetic fields in the presence of arbitrary current distributions including the presence of nonlinear materials. In regions of space where the current density is zero, the magnetic field is defined in terms of a scalar potential which solves Laplace's equation. In regions where currents are present, the code calculates the magnetic field directly using the Biot-Savart law.

The mesh used in the $r\theta$ plane of the magnet is shown in Fig. 4.4. Boundary conditions are $\Phi = $ constant along the horizontal and $B_{normal} = 0$ along the symmetry edge running through the center of the pole face. This mesh is replicated in z with the granularity shown in Table 4.2. This results in a total of 25,323 mesh points. The magnet iron ends abruptly at z = 17 cm with no shaping and chamfer. The problem takes roughly 3 hours of CPU time on a ALPHA 3000-400 undergoing 15 iterations.

We use the three-dimensional finite element analysis program TOSCA to calculate the scalar potential and the magnetic field. For fixed radii r and axial positions z, the individual multipole components are extracted using a straightforward Fourier analysis. Table 4.3 shows the peak multipole components and the integrated multipole components for Q1 magnet at a current of 86 A. These quantities are important, and will have different significance when the S800 spectrometer is operating in different modes. Fig. 4.5 shows the various multipole components as a function of z, the dis-
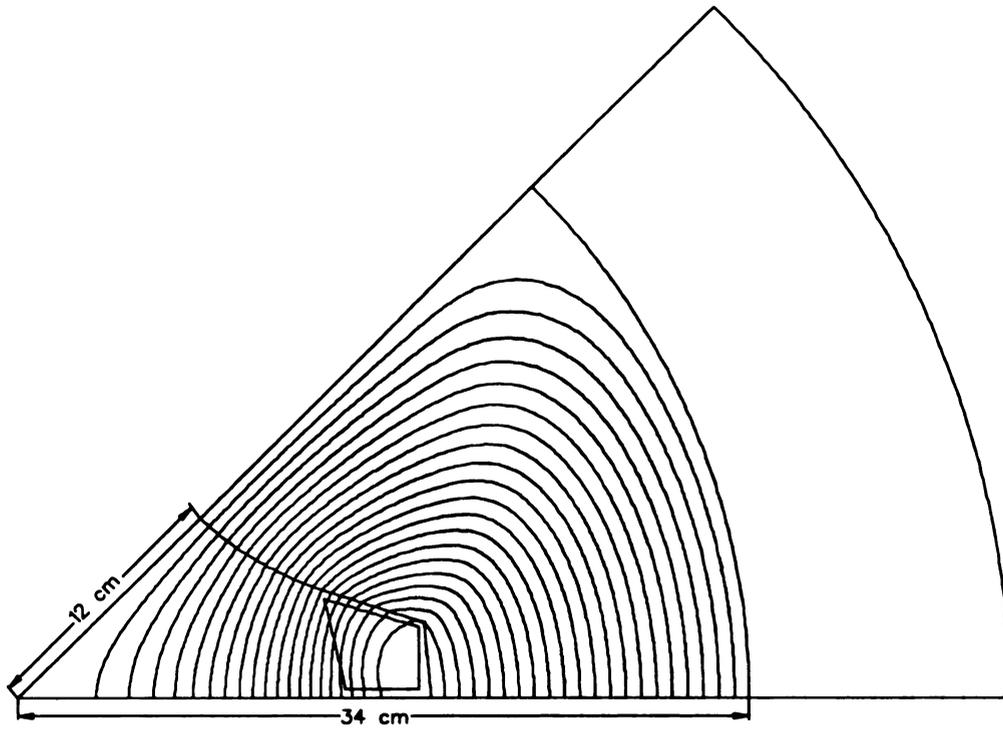
Figure 4.2: Octant of Q1 with magnetic field lines calculated by POISSON.
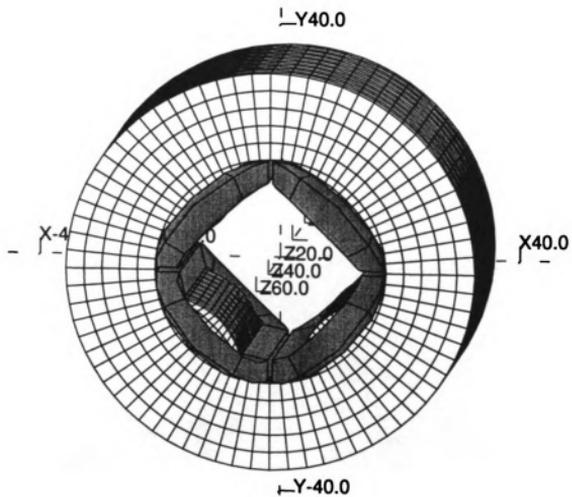
Figure 4.3: Q1 coils and iron geometry used for TOSCA calculations.
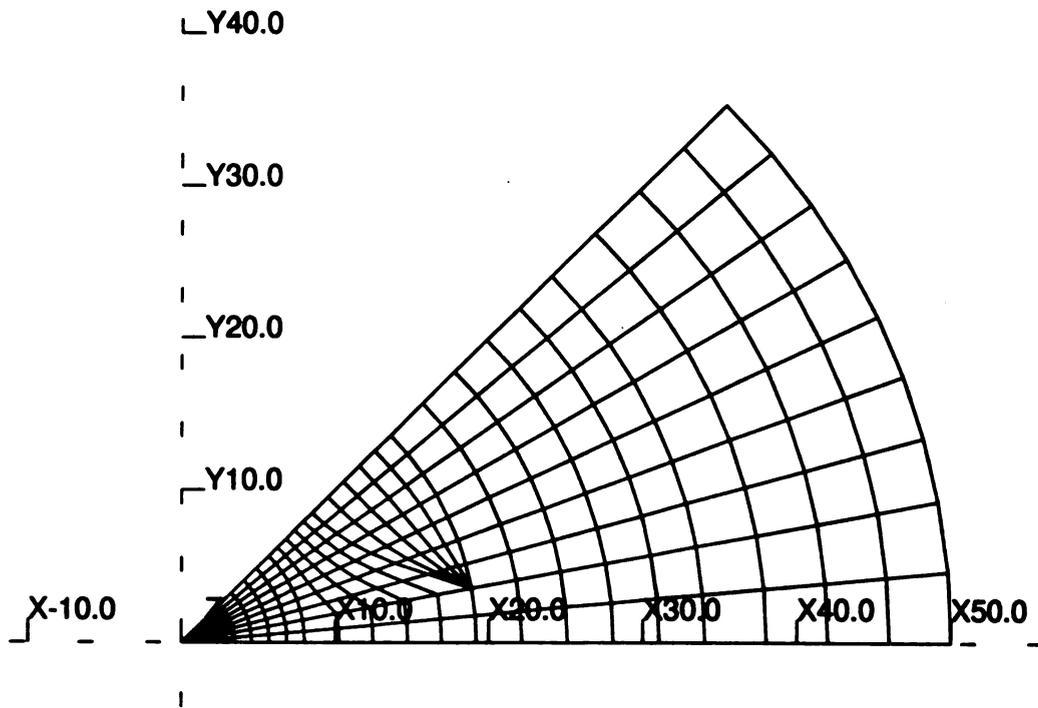
Figure 4.4: Details of the Q1 mesh used in the $r\theta$ plane for the TOSCA calculation.

Table 4.2: Longitudinal granularity for Q1 used in the TOSCA calculations.

z (cm)	Number of divisions	Type
$0 \geq z \geq 17$	8	quadratic
$17 \geq z \geq 25$	4	quadratic
$25 \geq z \geq 35$	4	quadratic
$35 \geq z \geq 45$	4	quadratic
$45 \geq z \geq 60$	5	quadratic
$60 \geq z \geq 100$	10	quadratic
$100 \geq z \geq 200$	12	linear
$200 \geq z \geq 300$	8	linear

tance from the center of the Q1 magnet along the beamline axis. As expected, the field inside the Q1 magnet is dominated by straight section of the coils, producing an almost pure quadrupole field. Near the ends of the Q1 magnet , the higher order multipole fields increase greatly in strength. We have plotted the integrals of these functions, integrated up to the plotted value of z, to show their development and convergence. There is rather long tail to large z, but the contribution to the integral past $z \approx 30$ cm is rather small. Note that these components change sign at the end of the Q1 magnet iron, yielding a significant cancellation effect in the final field integral. Numerical programs which calculate the magnetic field by some finite difference method solution of eq. 4.3 can not be expected to give highly reliable results near the interface of empty space and a highly nonlinear material such as the iron pole tip. However, since the field integrals depend only on the coefficients $b_{0,n}$ it is possible to determine then at lower radii and extrapolate to $r=r_0$. The results for Q1 are summarized as follows:

$$\frac{1}{2} \int_{-\infty}^{\infty} B_{r,2}(12cm, z)dz = \int_{0}^{\infty} B_{r,2}(12cm, z)dz = 0.49 \quad T \cdot m$$

$$\int_{0}^{\infty} B_{r,6}(12cm, z)dz = (2.0 \times 10^{-3}) \times 0.49 \quad T \cdot m$$

Table 4.3: Q1 multipole analysis results for half of the magnet at a radius of 8.8 cm.

n	Maximum $\mid B_{r,n} \mid$ (T)	$\int_0^z B_{r,n} dz (T \cdot m)$
2	1.754	0.358
6	8.54×10^{-3}	5.35×10^{-4}
10	1.63×10^{-3}	1.17×10^{-4}
14	3.76×10^{-4}	6.38×10^{-5}

Table 4.4: The calculated parameters of the Q1 magnet.

Operation current	86 A
Stored energy	68 kJ
Inductance	18.4 H

$$\int_0^\infty B_{r,10}(12cm, z)dz = (-6.1 \times 10^{-4}) \times 0.49 \quad T \cdot m$$

$$\int_0^\infty B_{r,14}(12cm, z)dz = (-4.5 \times 10^{-4}) \times 0.49 \quad T \cdot m$$

The calculated parameters for Q1 are given in Table 4.4. The calculated gradients for Q1 as a function of current are shown in Fig. 4.7.

A significant consideration in construction is the magnetic force on the coils. The magnetic field exerts a force $\mathbf{F} = \mathbf{J} \times \mathbf{B}$ per unit volume of current carrying coil and in superconducting magnets, where the field and current density are both high, this force can be very large. Such forces can cause severe problems in the design and construction of superconducting magnets. They can cause structural failure and destroy the magnet, or they can damage the superconductor or insulation. Perhaps the most serious problem, because it is so difficult to predict, is the degradation of magnet performance which may be caused by the sudden release of mechanical energy. Calculations of force and stress demand knowledge of the magnetic field throughout a winding. Many of the field computing programs are now being used in conjunction

TOSCA Calculations for Q1
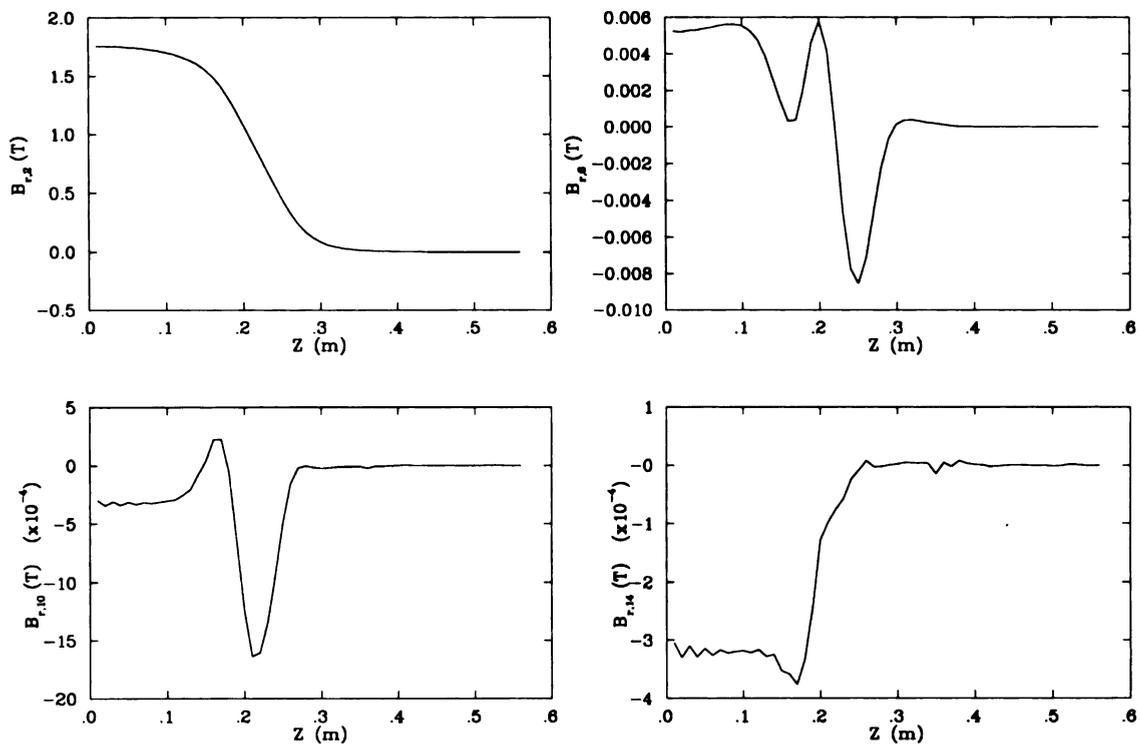
Figure 4.5: Multipole components of the Q1 radial field for the quadrupole (n=2) term and the first three allowed terms (n=6,10 and 14) are plotted as functions of z, the distance along the beamline axis from the center of the Q1 magnet at r = 8.8 cm.
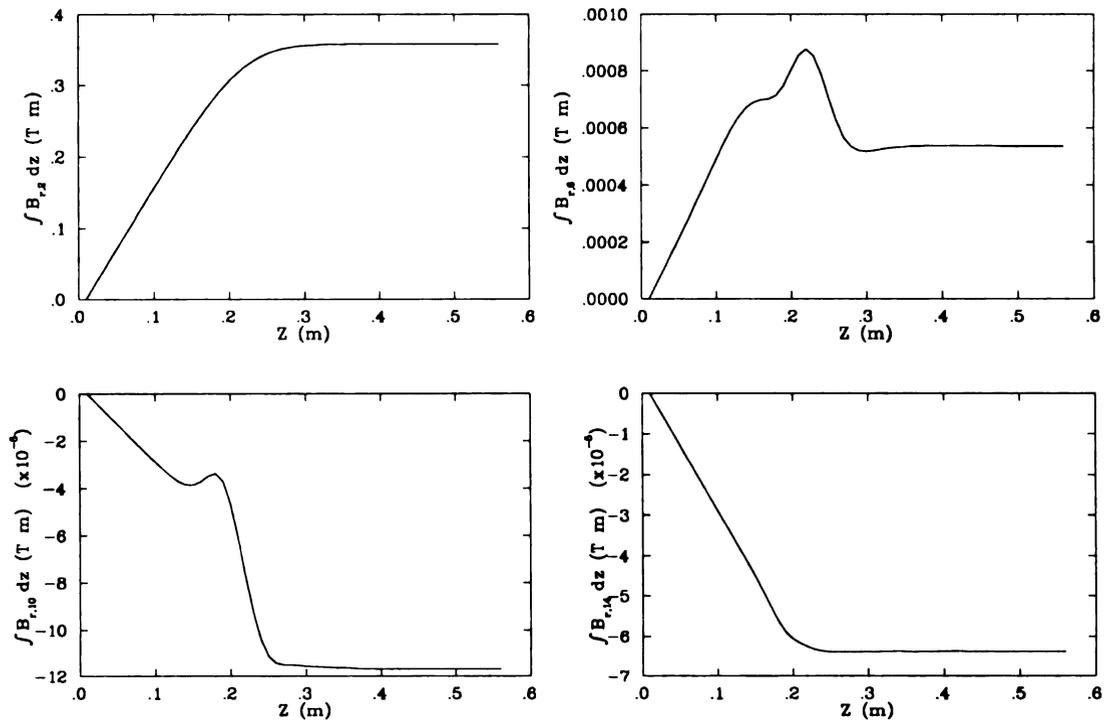
Figure 4.6: Integrated multipole component of the Q1 radial field $\int_0^z b_{r,n} dz$ for n=2, 6, 10 and 14 at r = 8.8 cm.
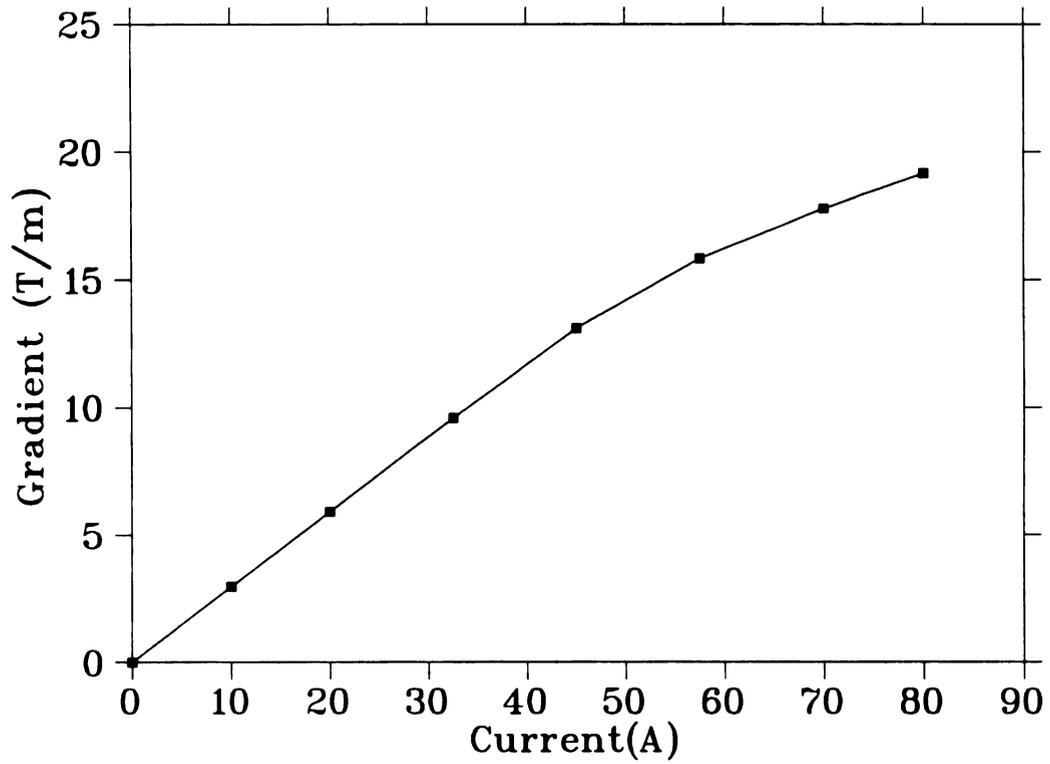
Figure 4.7: TOSCA calculations of the Q1 gradient as a function of current.

with finite element stress programs to calculate stress with considerable precision.

The forces on each coil of Q1 are calculated by TOSCA which integrates the body forces on the source conductors using $\mathbf{J} \times \mathbf{B}$. Each section of each coil is represented by an 8 or 20 node finite element. Gaussian quadrature integration with a selectable number of Gauss points is used to calculate the forces. The program calculated the force acting at the centroid of each section of each conductor. Since the fields produced near the straight section of the coils are stronger than the fields produced near the ends of the coils, the force acting on the straight section of the coils is larger. Fig. 4.8 shows the forces per unit length that act on the straight section of the Q1 coil. The strongest component of field is in the y direction and produces an outward x direction force on the conductors.

4.4.2 Magnetic field calculation of Q2 and the sextupole

The Q2 magnet design is similar to the Q1 magnet, but is a large version of the NSCL's standard beamline quads. The pole tip radius of Q2 is 21 cm which is three times larger than the NSCL's beamline quad's radius. As mentioned before, the dominant aberration of the beam optics at the focal plane of S800 spectrometer is x/θ^2. According to the beam optics calculation, the best place for a sextupole to correct this aberration is in Q2. The original Q2 and the sextupole designs, based on the two-dimensional magnetostatic code, POISSON, are shown in Fig. 4.9. However, the calculations assume that the iron and coils are infinitely long along the beam axis. Of course, the iron has a finite length and the coil must return, therefore the magnetic field can't be calculated precisely due to this loss of symmetry. It is necessary to use a three-dimensional magnetostatic code like TOSCA.

We used two straight bars to model the straight section of the Q2 coil. The cross section shape of the straight bar is the same as indicated in Fig. 4.9. However, the
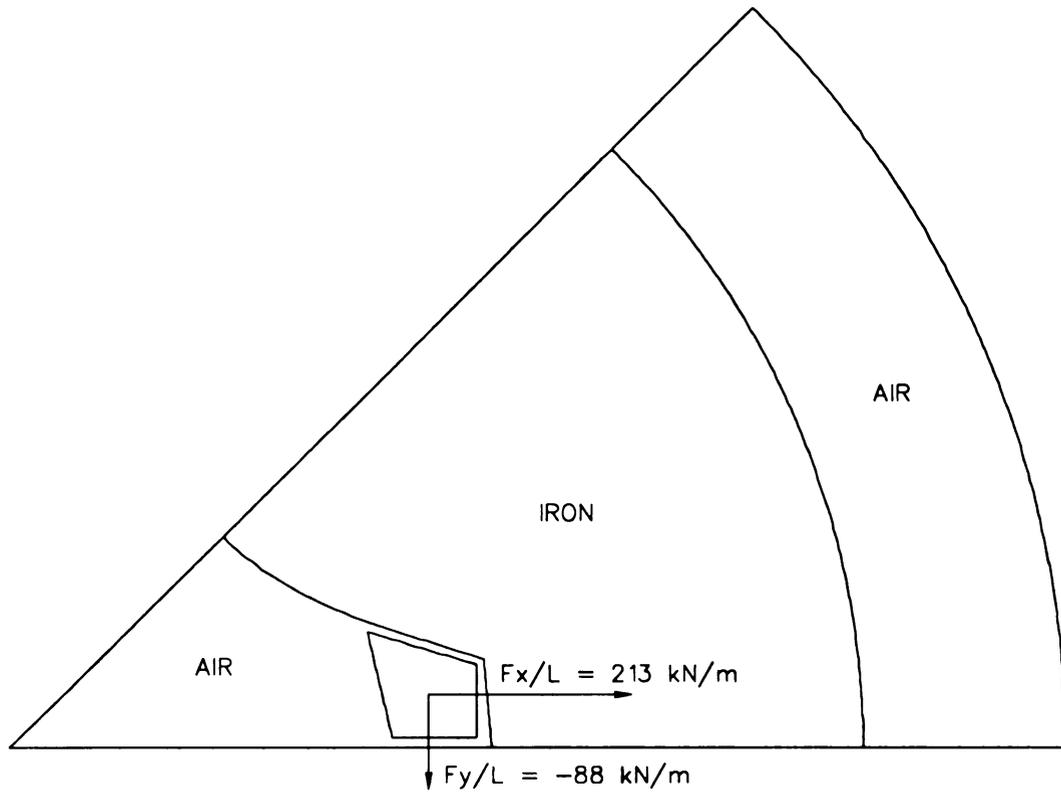
Figure 4.8: The x- and y-components of force per unit length on the straight section of the Q1 coil are calculated with the program TOSCA at $I = 86A$.

Table 4.5: Longitudinal granularity for Q2 used in the TOSCA calculations.

z (cm)	Number of divisions	Type
$0 \geq z \geq 15$	15	quadratic
$15 \geq z \geq 25$	5	quadratic
$25 \geq z \geq 30$	1	quadratic
$30 \geq z \geq 50$	1	quadratic
$50 \geq z \geq 200$	2	quadratic
$200 \geq z \geq 300$	1	linear

end of the Q2 coil is a more complex shape, especially in areas which involve a change in cross section. We used three 20-node bricks to approximately model one end of Q2 coil and also kept the cross sectional area of the 20-node brick coil the same as the straight bar's.

The sextupole coil is wound on the surface of a cylinder. It is best to model the sextupole coil using "the constant perimeter end". We assume it is made up of two straight sections parallel to the beamline axis. The half length of the central filament of these sections is 15 cm. The cross section of the sextupole is almost rectangular, the thickness is 1 cm in the radial direction and the width is 3.5 cm in the azimuthal direction. The ends of the sextupole conductor form a smooth curve over the cylinder. Fig 4.10 shows the Q2 iron, the Q2 and sextupole coils..

The mesh used in the $r\theta$ plane of Q2 and the sextupole are shown in Fig 4.11. Boundary condition are Φ = constant along the horizontal and $B_{normal} = 0$ along the symmetry edge running through the center of the pole face. This mesh is replicated in z with the granularity shown in the Table 4.5. This results in a total of 25,323 mesh points. The magnet iron ends abruptly at z = 15 cm with no shaping and chamfer. The problem takes roughly 2 hours of CPU time on a ALPHA 3000-400 undergoing 15 iterations.
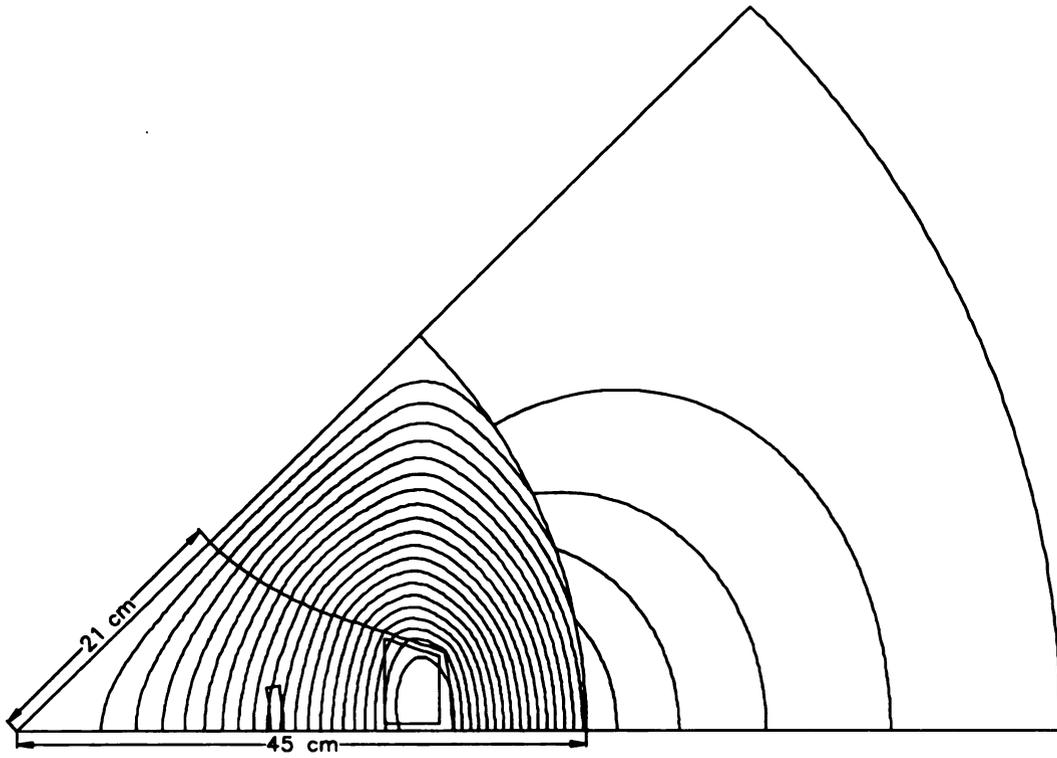
Figure 4.9: Octant of Q2 and the sextupole with field lines calculated by POISSON.
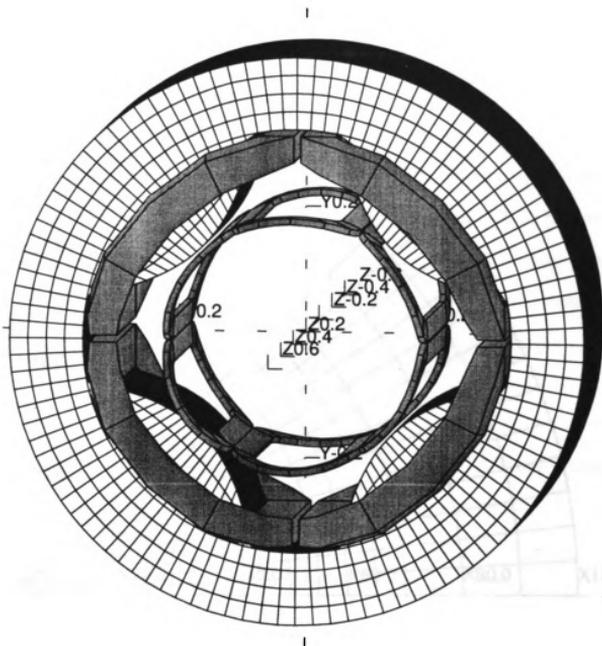
Figure 4.10: Computer simulation for Q2 and the sextupole magnets using TOSCA.
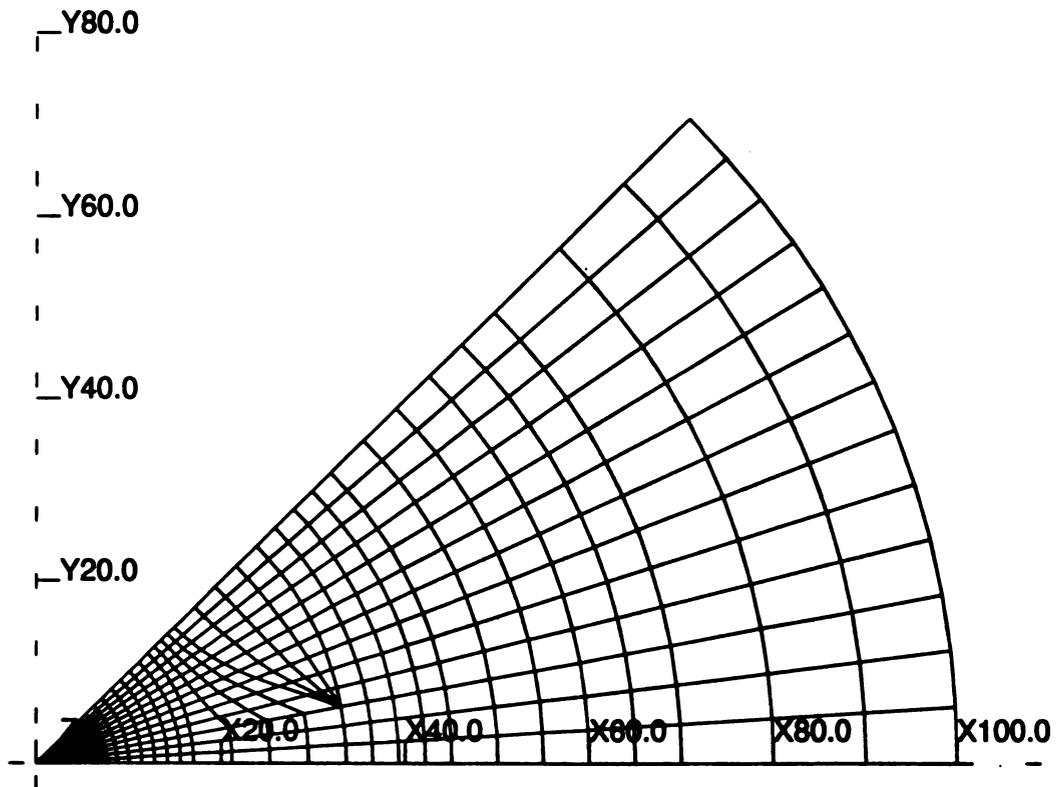
Figure 4.11: Details of Q2 and the sextupole mesh used in the $r\theta$ plane for the TOSCA calculation.

We use the three dimensional numerical integration program TOSCA to calculate the scalar potential and the magnetic field. For fixed radii r and axial positions z, the individual multipole components are extracted using a straightforward Fourier analysis. Table 4.6 shows the peak multipole components and the integrated multipole components for a Q2 magnet current of 90 A. Both of these two quantities are important, and will have different significance when the S800 spectrometer is operating in different modes. Fig. 4.12 shows the various multipole components as a function of z, the distance from the center of the Q2 magnet along the beamline axis. As expected, the field inside the Q2 magnet is dominated by straight section of the coils, producing an almost pure quadrupole field. Near the ends of the Q2 magnet, the higher order multipole fields increase greatly in strength. We have plotted the integrals of these functions, integrated up to the plotted value of z, to show their development and convergence. There is a rather long tail to large z, but the contribution to the integral past $z \approx 30$ cm is rather small. Note that these components change sign at the end of the Q2 magnet iron, yielding a significant cancellation effect in the final field integral. Since the field integral depends only on the coefficients $b_{0,n}$, it can be determined for the field integral and extrapolated to $r = r_0$. The results for Q2 are as follows:

$$\frac{1}{2}\int_{-\infty}^{\infty} B_{r,2}(21cm, z)dz = \int_0^{\infty} B_{r,2}(21cm, z)dz = 0.33 \quad T \cdot m$$

$$\int_0^{\infty} B_{r,6}(21cm, z)dz = (6.1 \times 10^{-4}) \times 0.33 \quad T \cdot m$$

$$\int_0^{\infty} B_{r,10}(21cm, z)dz = (-4.2 \times 10^{-5}) \times 0.33 \quad T \cdot m$$

$$\int_0^{\infty} B_{r,14}(21cm, z)dz = (-8.8 \times 10^{-6}) \times 0.33 \quad T \cdot m$$

Table 4.6: Q2 multipole analysis results for half of the magnet at a radius of 8.8 cm.

n	Maximum $\mid B_{r,n} \mid (T)$	$\int_0^z B_{r,n} dz (T \cdot m)$
2	0.6493	0.14
6	0.48×10^{-4}	3.5×10^{-5}
10	1.01×10^{-5}	1.0×10^{-6}
14	1.17×10^{-5}	9.0×10^{-8}

TOSCA Calculations for Q2
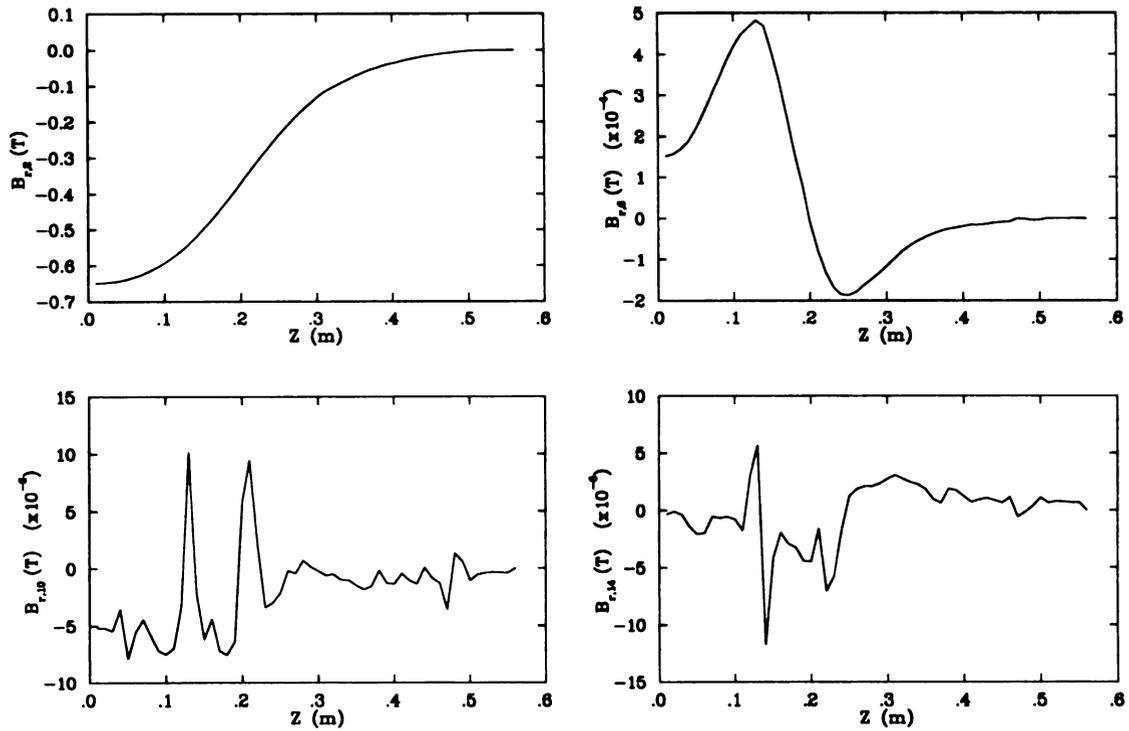
Figure 4.12: Multipole components of the Q2 radial field for the quadrupole (n=2) term and the first three allowed terms (n=6,10 and 14) are plotted as functions of z, the distance along the beamline axis from the center of Q2 magnet at r = 8.8 cm.
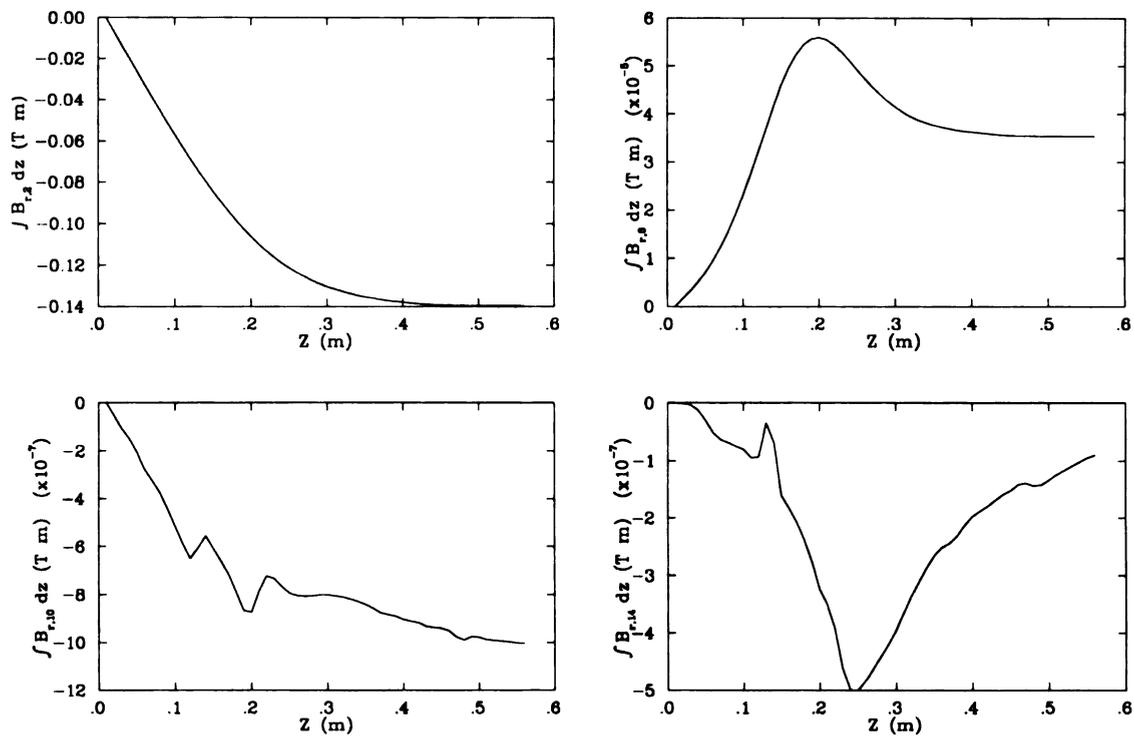
Figure 4.13: Integrated multipole component of the Q2 radial field $\int_0^z b_{r,n}dz$ for n=2, 6, 10, and 14 at r = 8.8 cm.

Table 4.7: The calculated parameters of the Q2 magnet.

Operation current	90 A
Stored energy	132 kJ
Inductance	32.8 H

Table 4.8: The calculated parameters of the sextupole magnet.

Operation current	3 A
Stored energy	103 J
Inductance	22.8 H

The calculated parameters for Q2 are given in Table 4.7. The calculated gradient of Q2 as a function of current are shown in Fig. 4.14. The claculated parameters for the sextupole magnet are given in Table 4.8.

The forces on the coils of Q2 magnet are also calculated by TOSCA. The only difference between Q1 and Q2 is that there is a sextupole inserted in Q2. If the sextupole current is zero, the force on the straight section of the Q2 coil is indicated in Fig. 4.15. Only a low current in the the sextupole is necessary to correct the x/θ^2 aberration since the sextupole field is very weak at Q2 coil position, the total forces acting on the Q2 coils are only slightly changed. However, the forces acting on the straight section of sextupole conductor are more complicated. Depending on the location of the coil, the force can be radially inward, outward, or in an azimuthal direction, as shown in Fig. 4.16. The coil clamping method must take this distribution into account.
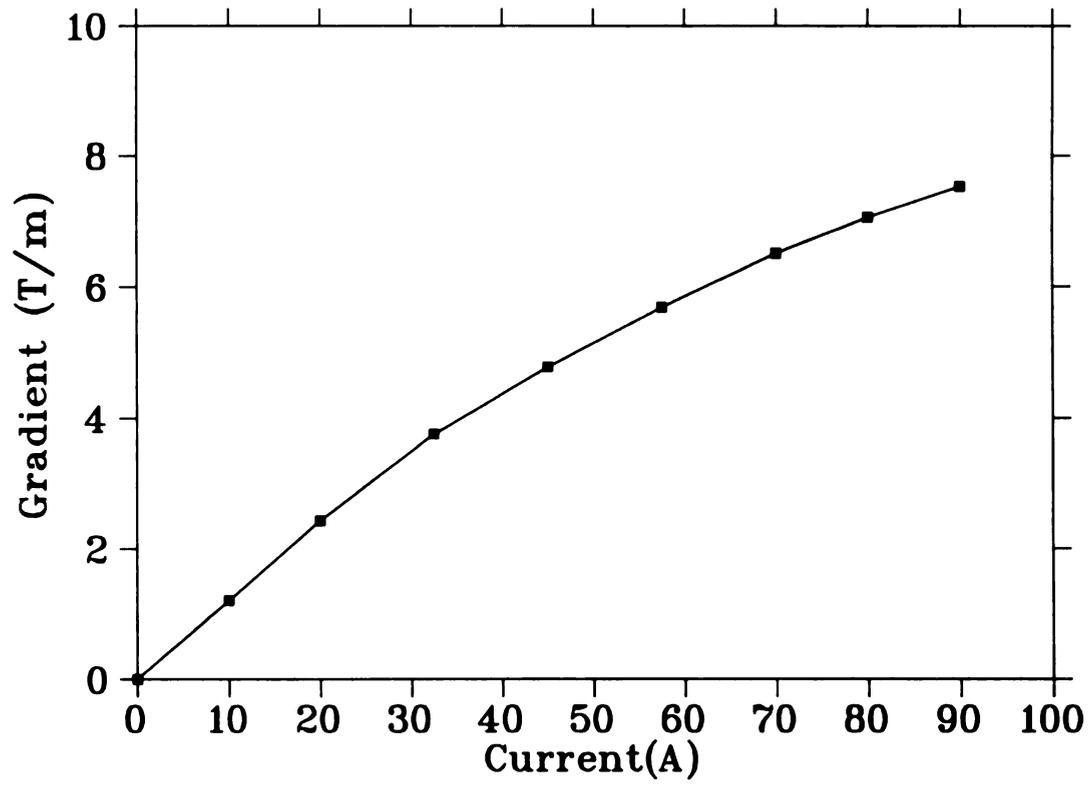
Figure 4.14: TOSCA calculation for Q2 gradient as a function of current.
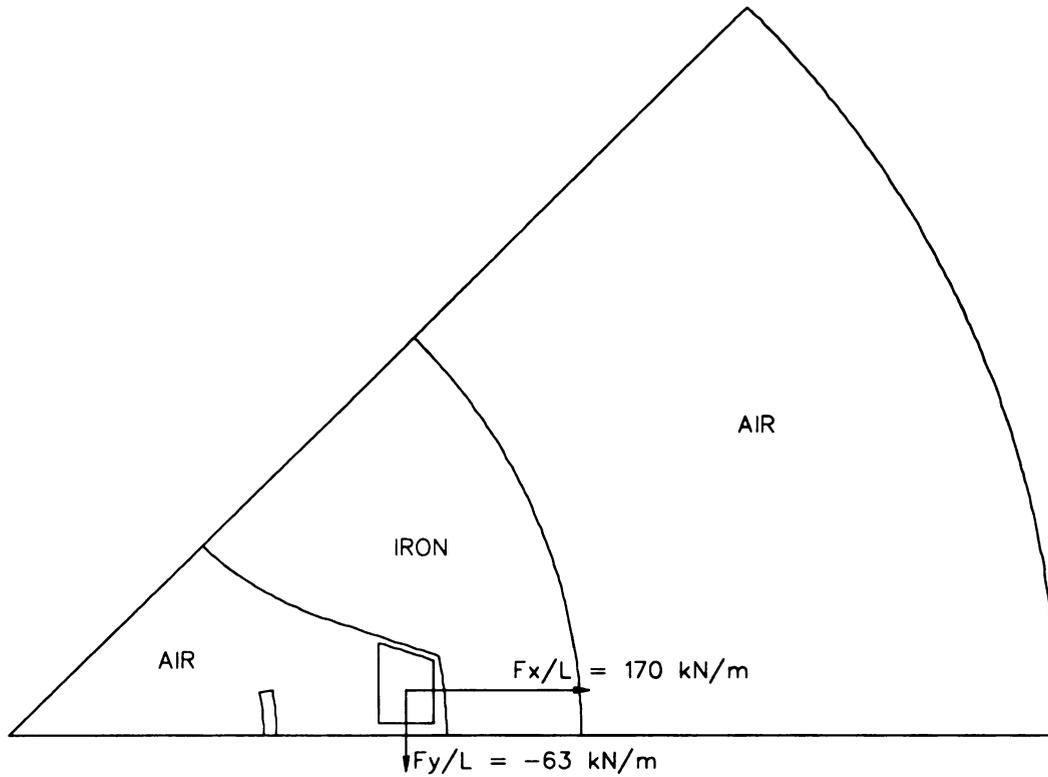
Figure 4.15: The x- and y-components of force per unit length on the straight section of the Q2 coil are calculated with the program TOSCA at $I_{Q2} = 90A$ and $I_{sextupole} = 0A$.

Fr/L • 6.4 kN/m
Ft/L • 8.3 kN/m

Fr/L • -6.4 kN/m
Ft/L • 8.3 kN/m

Fr/L • 3.5 kN/m
Ft/L • 10.5 kN/m

Fr/L • -3.5 kN/m
Ft/L • 10.5 kN/m

Fr/L • -9.2 kN/m
Ft/L • -2.1 kN/m

Fr/L • 9.2 kN/m
Ft/L • -2.1 kN/m
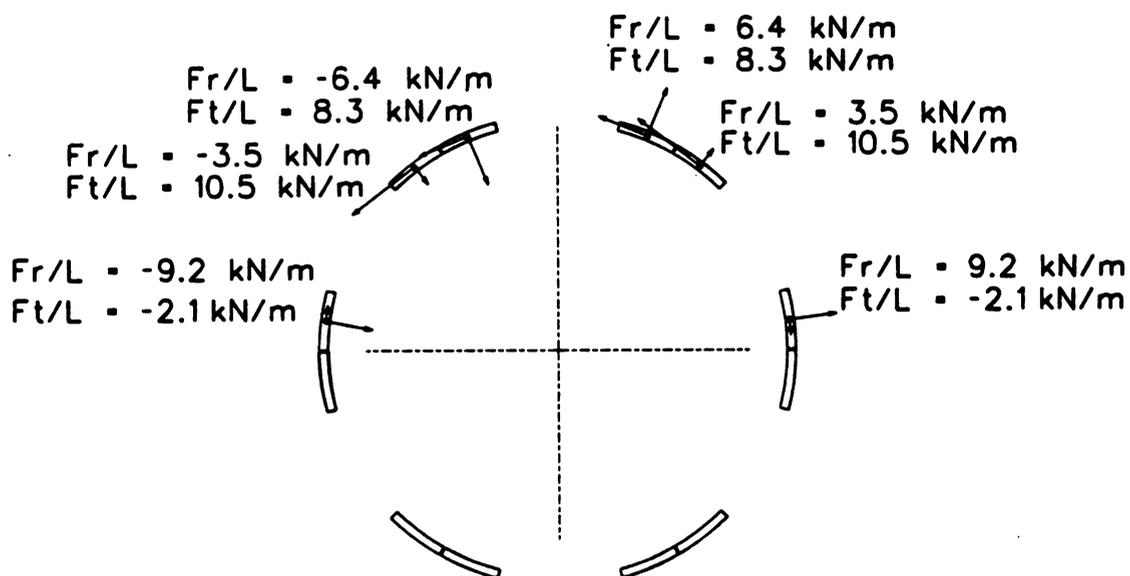
Figure 4.16: The radial and azimuthal components of force per unit length on the straight section of the sextupole coils are calculated with the program TOSCA at $I_{sextupole} = 3A$ and $I_{Q2} = 90A$.

4.5   Quench simulations

An evaluation of the quench behavior is needed for coil safety. In this case a dump resistor was not used for quench protection because a high field and small coil size make the quench propagation extremely fast, and the energy spreads more uniformly throughout the coil. However, the higher stored energy requires larger wire and higher operating current for protection in case of a quench. The code QUENCH [Wi68] has been used to evaluate the worst case scenario. Fig. 4.17 shows the internal voltage of Q1 increasing to 637 volts after quenching, which is still lower than the voltages of the NSCL standard beamline quads or the S800 beamline quads. Since the NSCL standard beamline quads have survived hundreds of quenches and the S800 beamline quads dozens of quenches without damage, no problem was anticipated for Q1 or Q2.

Since the sextupole coils are inside Q2, mutual inductance in the coils is significant and must be evaluated. We consider the total energy of the system

$$E = \frac{1}{2}L_{Q2}I_{Q2}^2 + \frac{1}{2}L_s I_s^2 + M I_{Q2} I_s$$

where L_{Q2} and L_s are the self-inductances of Q2 and the sextupole which are given in table 4.7 and table 4.8, and where M is the mutual inductance. We calculated the total energy by using TOSCA with both of the magnets on. Using above equation, the mutual inductance has been calculated to be 10.7 H. The worst case is Q2 quenching first, and the energy from Q2 transferring to the sextupole with a one second time delay, as seen in Fig. 4.18. The internal voltages for Q2 and the sextupole are shown in Fig. 4.19 and are not excessive.
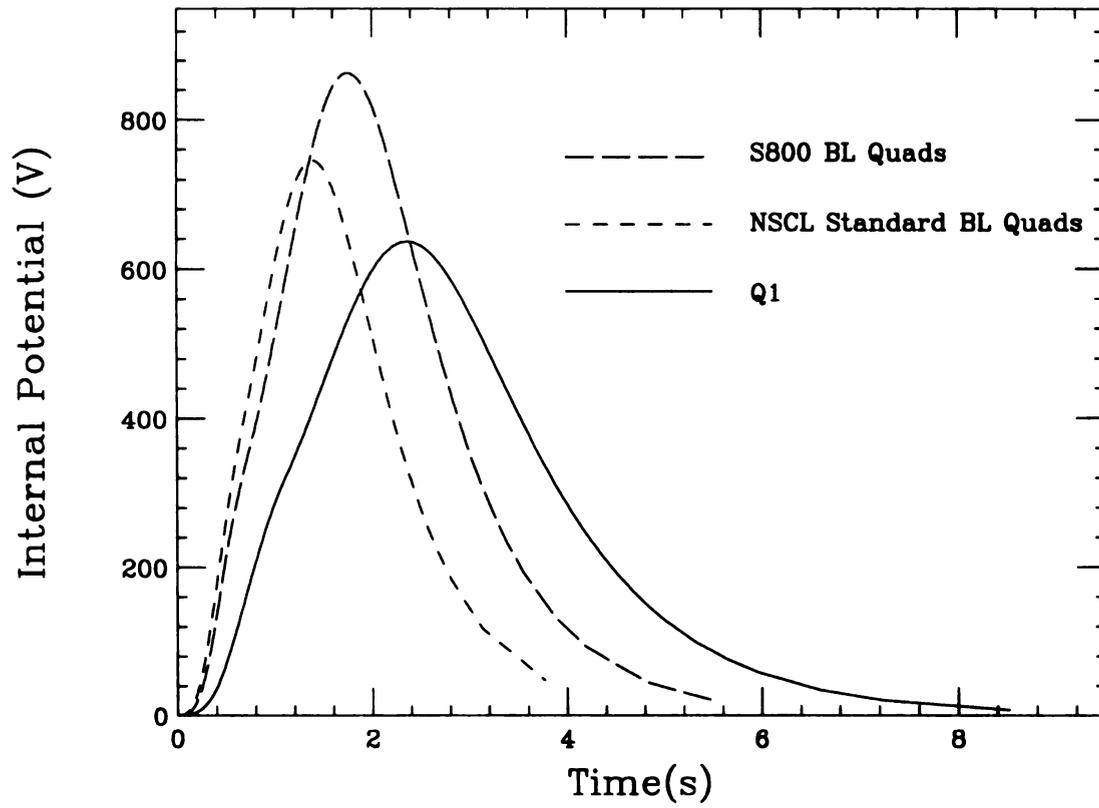
Figure 4.17: The comparison of the internal voltages in Q1, NSCL standard beamline quads and S800 beamline quads after quenching.
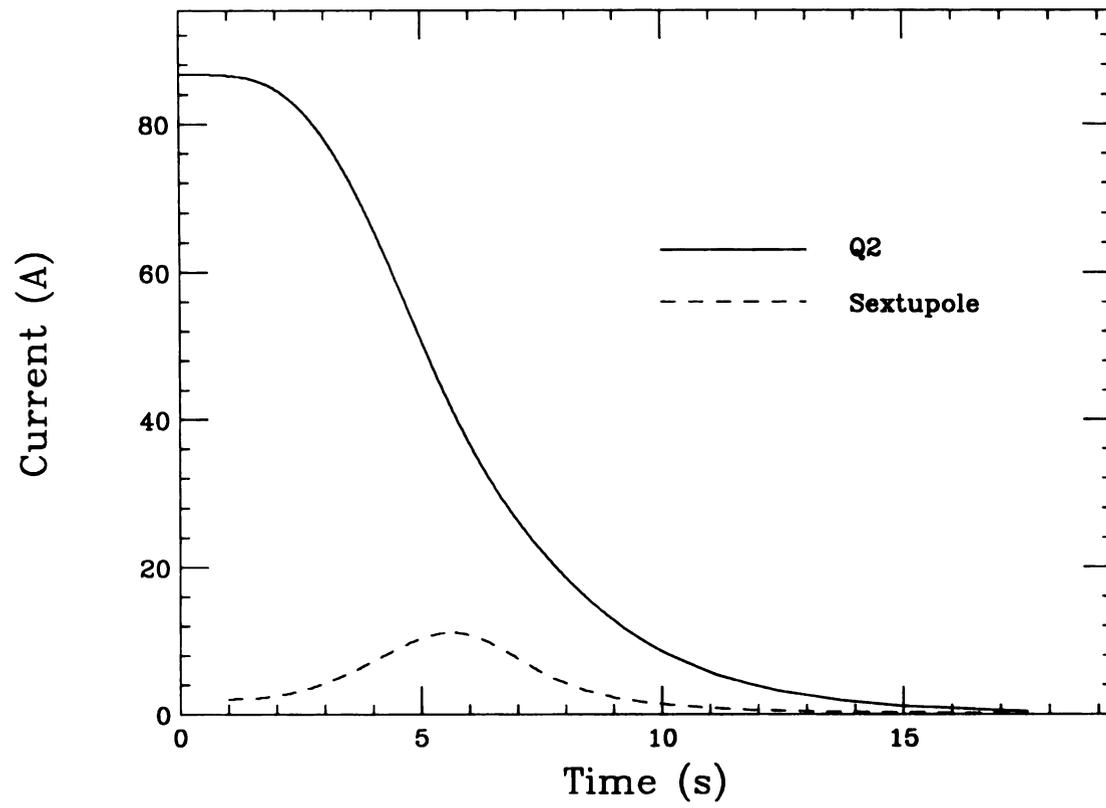
Figure 4.18: Decay of currents in Q2 and the sextupole after quenching.
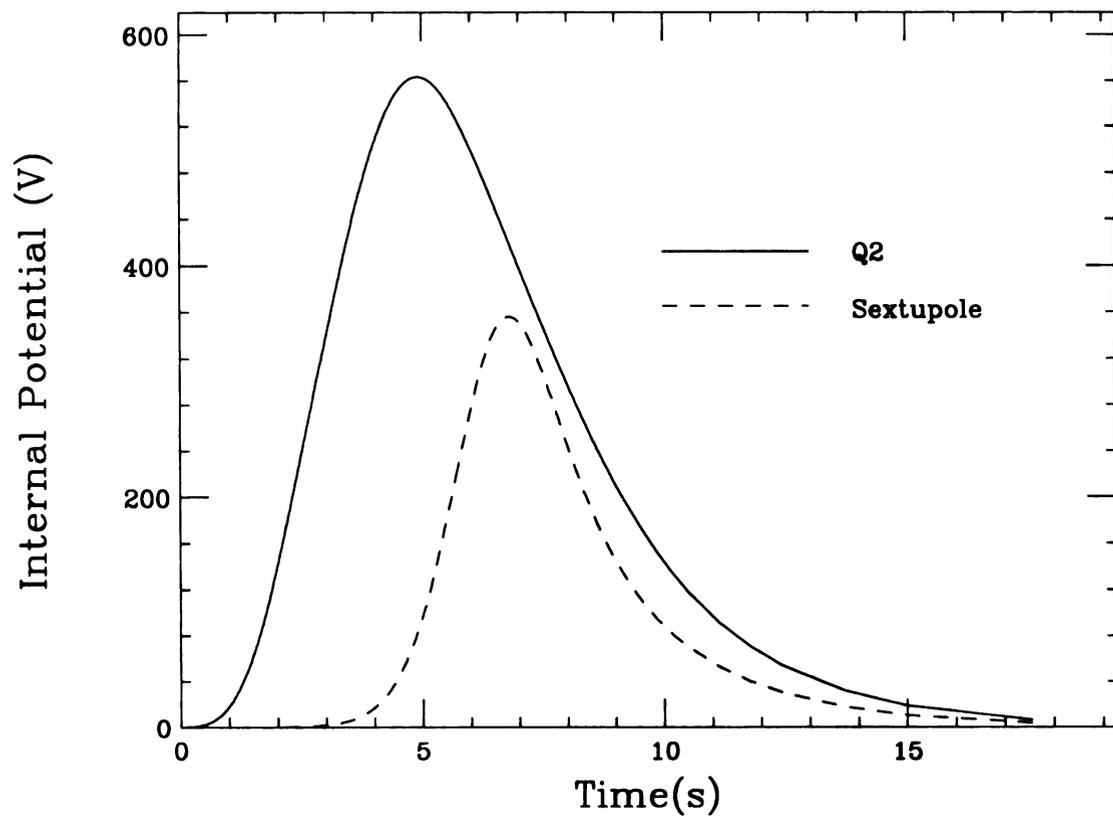
Figure 4.19: Internal voltages in Q2 and the sextupole after quenching.

4.6 Heat load calculations

Heat load is an important parameter for superconducting magnets. A high precision stainless steel spacer positions Q1 and Q2 with respect to each other. All elements are assembled into the same cryostat (Q1/Q2 doublet cryostat). A section view of the assembly showing the main features is given in Fig. 4.20. To minimize the overall liquid helium consumption load on our refrigeration system, and to cryogenically decouple devices during operation, a batch-fill mode of operation can be used. The break even point over a continuous flow system required a minimum holding time for liquid helium between fills. The length of this time period depends on the system and operation parameters. In order to fulfill this condition, and to keep the reservoir a reasonable size, careful attention must be payed to all sources if heat acting on the helium vessel. Since much of the liquid nitrogen shield is cooled by conduction through the copper to a pool of boiling liquid nitrogen at the center of the device, temperature gradients exist in the shield. The shield temperatures was measured with type T thermocouples; the highest temperature of the nitrogen shield is 95 K which was used for the heat load calculation. The heat load for the cryostat mainly comes from support links, radiation, the vent pipe, and the feed and return lines. Subsequent sections treat these four sources of heat load contributions in detail [De].

4.6.1 Support link heat loads

A support link for a superconducting magnet should be strong enough to sustain possible off-centering forces, and it should be a poor heat conductor in order to reduce the heat influx into the liquid helium. The usual choices of materials satisfying both conditions are composites, whose fibers are available in various forms. The NSCL standard beamline quads built in this lab have employed the epoxy fiberglass

ELECTRICAL LEADS

VERTICAL LINK

CRYOSTAT

Q-1 YOKE

Q-1 POLE TIP

Q-1 COIL

Q-2 YOKE

Q-2 POLE TIP

Q-2 COIL

HEXAPOLE

BORE TUBE

NITROGEN SHIELD

HELIUM VESSEL

SPACER
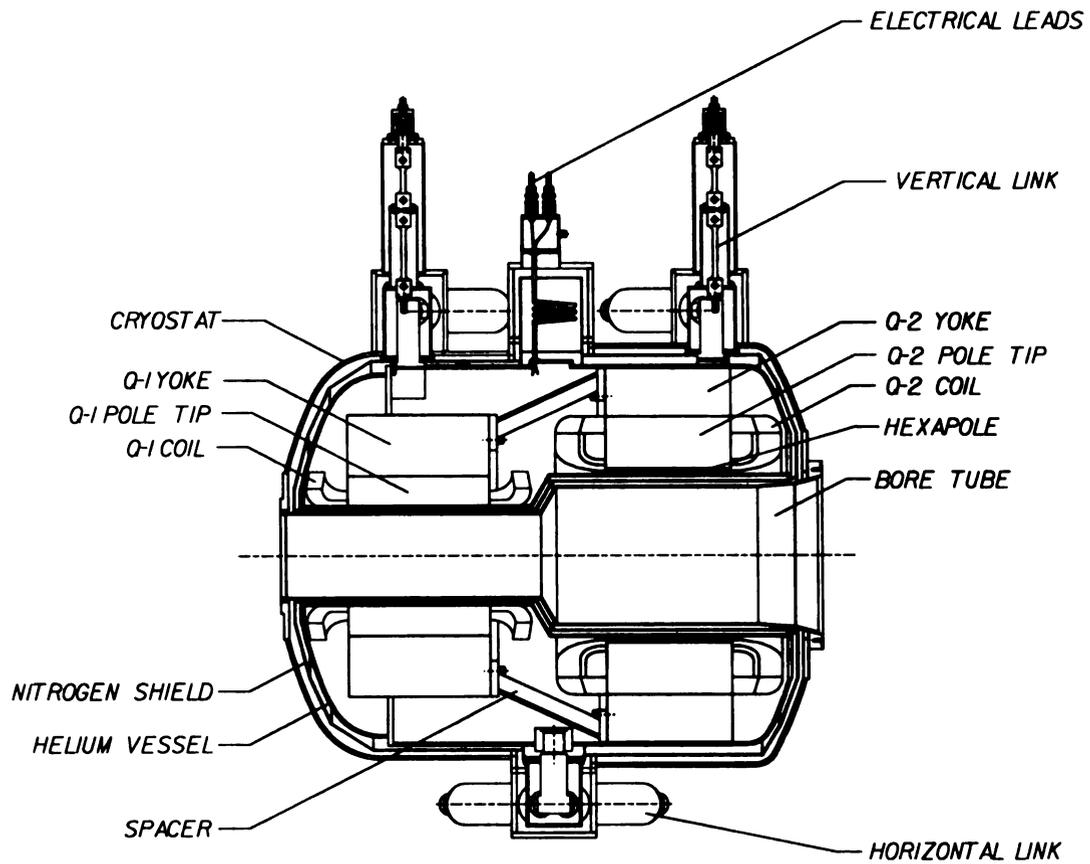
HORIZONTAL LINK

Figure 4.20: View of a longitudinal section of Q1, Q2 and sextupole.

composite G-10 (E-glass) for their links. In Q1/Q2 doublet, the 8 horizontal links have also used G-10.

The distance between the Q1/Q2 doublet and the first S800 spectrometer dipole (D1) is very short and they produce overlapping magnetic fields, so there is a strong interaction between the Q1/Q2 doublet and D1. To reduce the Q1/Q2 doublet displacement due to D1, we have employed titanium for the 2 vertical links of the doublet. The total heat loads of the support links is

$$Q_{links} = Q_{G-10} + Q_{Titanium}$$

where the cross section area is 1.06 cm^2 for the titanium links and 0.7 cm^2 for G-10 links; both links are 12.7 cm long. Also, we know that $\int_{4.2}^{95} \lambda dT = 2.905$ W/cm for titanium [Jea] and $\int_{4.2}^{95} \lambda dT = 0.272$ W/cm for G-10 [Nbs]. We obtain

$$
\begin{aligned}
Q_{links} &= 2 \times \frac{A_{Ti}}{l_{Ti}} \int_{4.2}^{95} \lambda_{Ti} dT + 8 \times \frac{A_{G-10}}{l_{G-10}} \int_{4.2}^{95} \lambda_{G-10} dT \\
&= 0.61 W
\end{aligned}
\tag{4.13}
$$

Even though the heat load of titanium is ten times bigger than G-10's, the calculation result shows using titanium for the vertical links is still acceptable.

4.6.2 Radiation heat loads

To reduce radiation, we have used a high conductivity aluminum tape, 3M #425 (from 3M Corporation) as coatings on both the 4K and 95K surfaces. We assume all the helium vessel and shield of Q1/Q2 doublet are two long concentric cylinders. We calculate that the bore tube surface area of the helium vessel is 12,000 cm^2 and the rest surface area of the helium vessel is 39,000 cm^2. If we assume 1.27 cm clearance between the helium vessel and the nitrogen shield, we can calculation that the bore

tube surface area of the nitrogen shield is 11,000 cm^2 and the rest area of the nitrogen shield is 40,000 cm^2.

The radiation heat load can be written as [Ho81]

$$Q_{radiation} = \frac{\sigma A_1(T_1^4 - T_2^4)}{\frac{1}{\epsilon_1} + \frac{A_1}{A_2}\left(\frac{1}{\epsilon_2} - 1\right)} \tag{4.14}$$

where σ is the proportionality constant and is called the *Stefan − Boltzmann* constant with the value of 5.669×10^{-12} W/cm$^2 \cdot$ K^4. ϵ is the emissivity for aluminum. ϵ_1 and ϵ_2 are 0.038 and 0.011 at 95 K and 4.2 K [Le80]. Now we use eq.(4.14) to calculate the radiation heat load.

$$Q_{radiation} = 0.2 \ W \tag{4.15}$$

4.6.3   Vent pipe heat loads

The safety vent pipe is 1.59 cm in outer diameter, 0.04 cm wall thickness and 19 cm long of 304 stainless steel, its diameter and length based on calculations for safe venting to prevent liquid helium container overpressure. There are two kinds of the heat loads associated with this vent pipe. One is the pipe wall thermal conduction heat load. The other is the helium gas conduction heat load within the vent pipe. We know that $\int_{4.2}^{95} K_{wall}dT = 4.525$ W/cm [Jeb] and $\int_{4.2}^{95} K_{gas}dT = 0.053$ W/cm [Ak50]. Therefore, the vent pipe heat flux is determined below:

$$\begin{aligned} Q_{pipe} &= \frac{A_1}{L}\int_{4.2}^{95} K_{wall}dT + \frac{A_2}{L}\int_{4.2}^{95} K_{gas}dT \\ &= 0.05 \ W \end{aligned} \tag{4.16}$$

4.6.4   Feed and return line heat loads

During isolated operation, that is, when additional liquid helium is not being fed to the device, only the feed line contributes if the return line is open and gas cooled. We use

Table 4.9: Calculation heat loads for the Q1/Q2 doublet.

Item	LHe (liter/hour)
Support links	0.92
Radiation	0.30
Vent pipe	0.08
Feed and return lines	0.29
Total	1.59

Invar tubing which is 1.27 cm in diameter and 0.089 cm thick. We assume the length of the tube from helium vessel to the vacuum break is 61 cm and has no liquid nitrogen intercept. We know that $\int_{4.2}^{300} \lambda_{wall} dT = 35$ W/cm and $\int_{4.2}^{300} \lambda_{gas} dT = 0.264$ W/cm. We obtain:

$$
\begin{aligned}
Q_{line} &= \frac{A_1}{L} \int_{4.2}^{300} \lambda_{wall} dT + \frac{A_2}{L} \int_{4.2}^{300} \lambda_{gas} dT \\
&= 0.193 \; W
\end{aligned}
\tag{4.17}
$$

4.6.5 Total heat loads for the Q1/Q2 doublet

From eq.(4.13), eq.(4.14), eq.(4.16) and eq.(4.17), we can easily calculate the total heat loads for Q1/Q2 doublet. During normal magnet operating, the helium pressure is around 1.2 atm. We can convert the heat load units from Watts to liters of liquid helium consumption per hour. 1 Watts = 1.513 liters/hour. The calculated boiloff rate is listed in Table 4.9. The actual measured heat load is 2 W for the Q1/Q2 doublet.

4.7 Construction of Q1, Q2 and the sextupole

4.7.1 Coil winding

The coil is the most delicate component of a superconducting magnet. All of the Q1, Q2 and sextupole coils were random- and wet-wound with Stycast epoxy on a semi-automatic winding table. The number of turns was counted with two counters. A mechanical ruler was used to measure the length of the wire used. The Stycast epoxy was mixed with 4.5 % of Catalyst 11 by weight and poured into the epoxy bath. During the winding process, the epoxy bath was cleaned and refilled with fresh epoxy every two hours and warmed to 158^0 F using a heater in order to reduce the epoxy viscosity.

A test coil was wound before the actual winding, to test the winding devices and to develop the winding technique. During winding many turns crossed over each other at the corner where there was a transition between the straight sides and the end arc. If the shape of the end form was not correct, shorted turns would occur. Additionally, the angle of the end form from the bottom of the winding must be adjusted so that turns did not crowd up at the top or bottom of the end form. One of the Q2 coils with 2160 turns of 0.85 mm conductor was wound in three hours; winding one of the Q1 coils with 1680 turns of 0.7 mm wire took the same amount of time.

Since the cross section of the sextupole coil is about 1 cm thick and 3.5 cm wide and the wire is very small, it was difficult to make this kind of coil. During the sextupole coil winding process, we reduced the wire tension to prevent the wire from breaking, therefore the wire had to be packed in place every 200 $\sim$ 300 turns to maintain a high packing factor. Especially when coil winding nears the finish number of turns, winding speed was slowed down to allow additional wire packing. It was found that 2160 turns of 0.3 mm wire can be wound to produce a sextupole coil in four hours. A

total of eleven sextupole coils been wound. Four of the coils were wound during the winding development process and were not seen as usable for various reasons such as variance in number of turns and shorted turns, etc.

Each of the coils for Q1, Q2 and the sextupole was oven cured. It took two hours at 212^0 F followed by a four hours post cure at 300^0 F. The electrical insulation of the Q1 , Q2 and sextupole wire was provided by formvar. During the coil winding process, the electrical insulation sometimes became damaged and several turns could be shorted. After we finished each coil, the resistance, inductance, and dissipation [Mo79] of the coil were measured to verify that there were no turn-to-turn shorts.

4.7.2   The Q1, and Q2 coils testing

The low carbon iron for the pole tips and yokes of Q1 and Q2 was machined with numerically controlled machines. In total, the magnet proved to be inexpensive and straight forward to build. This was aided because the field was shaped primarily by the iron and conductor placement was less important. Both Q1 and Q2 have cryogenic Hall generators mounted on the pole tips, to allow measurement and setting of the magnetic field. In section 4.4.1 and section 4.4.2, we discussed the force acting on the Q1 and Q2 coils. At the Q1 and Q2 coils location, the strongest components of the field are in the azimuthal direction and produce the biggest force in the outward radial direction. The forces in the outward radial direction are nearly three times larger than the forces in azimuthal direction. The coils of Q1 and Q2 are shimmed against the pole tip first, then against each other by using titanium spacers and G-10 shims. The reason we used titanium spacers was because titanium has a smaller thermal contraction than iron and G-10. The titanium spacers were held in place by G-10 keepers. On the one end of the Q1 and Q2 magnets, the bus bars and G-10 stand offs were fixed on the yoke steel, as shown in Fig. 4.21 The current leads of all

Table 4.10: Inductances of the Q1 and Q2 magnets.

Magnet	$L_{measured}$(Henry)	$L_{calculation}$(Henry)
Q1	20.1	18.4
Q2	34.0	32.8

coils were soldered with a bigger superconducting wire to increase the stiffness and to prevent the wire breakage, then connected to the bus bars.

A high precision stainless steel yoke spacer positions the Q1 and Q2 magnets with respect to each other. The Q1 and Q2 magnets were tested before being installed in their permanent cryostat in order to ensure basic coil performance before undertaking the procedures involved in assembly of the cryostat. The leads were connected, and level gages installed. The whole assembly was installed in a large commercial dewar which is a 1.83 m in diameter and 3.65 m long cylinder. Two relatively long current leads (4 meters each) were needed to make a connection from the Q1 and Q2 magnets to the existing 500 A commercial current leads at the dewar top.

In the first Q2 coil test run, the Q2 magnet quenched at 61 A. But in the second run, the Q2 magnet current reached 90.1 A which is our design value. However the Q1 magnet performance was quite different from the Q2 magnet. The Q1 magnet quenched at 57, 64, 65, 66 A; about 75% of our design value. One of the reasons Q1 coils quenched at a low current is that the Q1 magnet was on top of the Q2 magnet and the Q1 coils were not covered 100 % by liquid helium. After refill to almost cover the magent, the Q1 magnet current reached our design value, 86 A.

During the testing process, the inductances of the Q1 and Q2 magnets were measured, Table 4.10 shows the measurement results and TOSCA calculations.

Figure 4.21: Q1 and Q2 coils assembly.

4.7.3   The Q1, Q2 and sextupole magnet assembly

The sextupole magnet was mounted to the helium vessel bore tube which is shown in Fig. 4.22. In section 4.4.2 we discussed stress on the sextupole coils. The forces acting on the straight section of the sextupole coil are complicated. Depending on the location of the coil, the force can be radially inward or outward, or in an azimuthal direction. The maximum force per unit length on the straight section of the sextupole coil is 11 kN/m. The six G-10 locating spacers for the sextupole were fixed on the helium vessel bore tube. The G-10 spacers prevented the coils moving in azimuthal direction. The straight sections of the sextupole coils were held in position with stainless steel bands. Even though the forces acting on the end of the coils were much smaller than the straight sections, B stage fiberglass tape was wound around the coil and cured. The bus ring was attached on the helium vessel bore tube. Before the current leads were soldered to the bus ring, the leads of each coil were soldered with bigger superconducting wires, to increase the stiffness and to prevent the wire from breaking.

After the sextupole was in position, the end bell of helium vessel on Q2 side and the helium vessel bore tube were aligned and welded together in vertical position on the assembly table. We used a crane to picked up the Q1, Q2 iron and coil assembly from the testing dewar and drop in the helium vessel bore tube. Since the clearance between the pole tip of Q2 and the sextupole fixture was very small (0.032 in), several people helped to guide this installation and to prevent the coils from being damaged.

Figure 4.22: Sextupole coils assembly.

Chapter 5

Magnetic Field Mapping and Analysis

5.1 Introduction and need for quality maps

S800 spectrometer offers a large phase space acceptance, with solid angles of more than 20 msr and energy acceptance of greater than 10%. Such a large solid angle and high resolution spectrometer requires careful consideration and correction of aberrations. The large phase space makes the correction process considerably more difficult and complex. The conventional correction of aberrations with higher order hardware (such as dipole edge curvatures, sextupoles, octupoles, etc) will cure second order or third order terms, but these terms will eventually limit the maximum solid angle and energy acceptance for a given resolution. The superconducting sextupole in Q2 will be used to reduce the x/θ^2 term, for a limited solid angle and for special cases (to allow the use of a shadow bar in the focal plane). For the rest of the aberrations, we will use the optimization computer code COSY INFINITY to do software corrections. In order for the calculations to work, precise and accurate magnetic field maps of the Q1/Q2 doublet, D1 and D2 dipoles, and S800 beamline quadrupole triplets are necessary to achieve high resolution using ray reconstruction [Be93]. This chapter will discuss the mapping and results for the spectrometer quadrupole magnets.

5.2   Quadrupole mapper

A mapper used for magnetic field measurement is based on a 486 PC computer, with an Animatics 5000 Stepper Motor Controller and F.W. Bell 9903 series 3 axis gaussmeter. The control program was written using Borland Turbo Pascal compiler version 7.0.

Two different types of superconducting magnets were mapped with this apparatus: the S800 beamline quadrupole triplets and the S800 spectrometer doublet. A complete map requires motion in three dimensions. Azimuthal (θ) movement of the probe is achieved through the use a NEMA 34 servo motor and encoder. The increments are applied through an 80 tooth gear and worm drive, with a resolution of 0.09 degrees. Along the beamline axis (z), movement of probe is achieved through a non-magnetic Thompson slide rail assembly equipped with a NEMA 23 servo motor and encoder. This allows for z direction movement of the probe at programmable speeds up to 1 cm per second. The radial positioning of the probe is done with non-magnetic threaded rod inside the probe holder box. The center of rotation is captured and held in position by means of an aluminum machined frame which is flat to plus or minus 0.0127 cm over entire 76.2 cm length.

The gaussmeter utilizes the Hall effect to measure magnetic field. The instrument has a range of 10 μG to 2.9999 MG at sampling frequencies up to 50 kHz. The maximum field produced by any of the magnets is 2 Tesla. The three axis Hall probe of the gaussmeter has been calibrated using an NMR system. Figure 5.1 shows the magnetic field difference between the gaussmeter and NMR measurements for one of the three channels. The lines through the data are fourth order polynomial fits. The fitting coefficients are shown in Table 5.1.

$$\Delta B = a + bB_g + cB_g^2 + dB_g^3 + eB_g^4$$
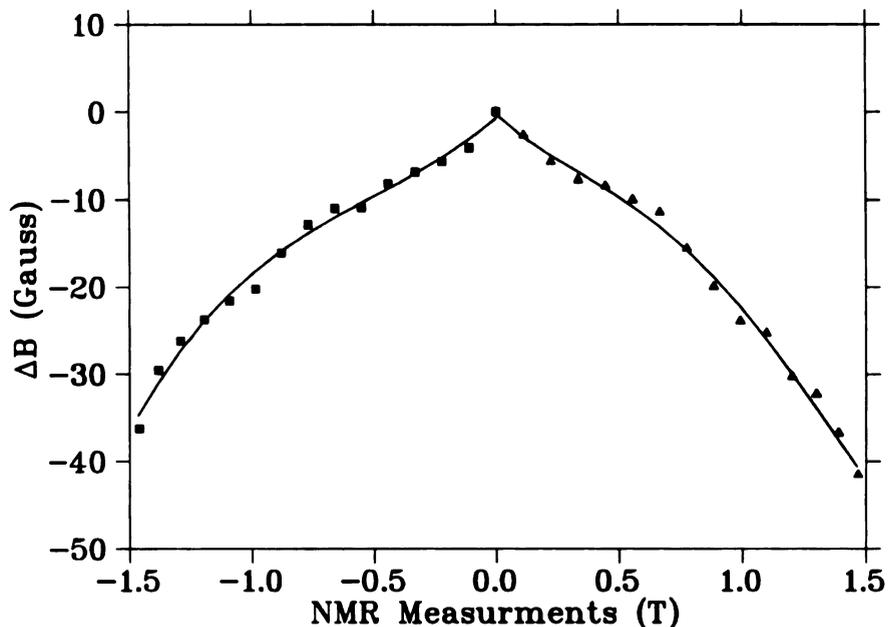
Figure 5.1: The magnetic field difference between the NMR and gaussmeter measurements for one channel. The solid lines through the data are fourth order polynomial fits.

where B_g is the gaussmeter field measurement.

Channel one of the probe measures the radial component of the magnetic field. Channel two measures θ component, or tangential component. Channel three measures the z component, which is component of the field along the beamline axis. The data acquired by the meter are transmitted through the instrument's RS-232 serial port to the PC.

The design of the gaussmeter makes it best suited for situations where the probe is in a fixed position during data acquisition. The feature conflicts with the desire to measure the field as quickly as possible. The commands to acquire data, MExx, with varying timing criteria. Thus, some measurement were in error when the probe was moved before the new field was accurately read.

In order to synchronize the field data with respect to the position, the design engineer at Bell was contacted for alternate solutions. A command that was imple-

Table 5.1: The fourth order polynomial fitting coefficients for the field differences between NMR and Gaussmeter measurements.

Coefficient	Negative field	Positive field
a_1	-0.72951	-0.25016
b_1	2.35420×10^{-3}	-2.64737×10^{-3}
c_1	1.70199×10^{-7}	3.18635×10^{-7}
d_1	1.06793×10^{-11}	-3.90871×10^{-11}
e_1	-5.82006×10^{-17}	1.15326×10^{-15}
a_2	-0.28693	-0.32442
b_2	3.39651×10^{-3}	-2.58475×10^{-3}
c_2	2.26697×10^{-7}	-2.46902×10^{-7}
d_2	1.80889×10^{-11}	-1.81681×10^{-11}
e_2	1.82584×10^{-16}	2.23829×10^{-16}
a_3	-0.28672	-0.70295
b_3	3.83656×10^{-3}	-4.04085×10^{-3}
c_3	-2.46902×10^{-7}	-3.29303×10^{-7}
d_3	-1.47827×10^{-11}	2.87842×10^{-11}
e_3	-1.47622×10^{-16}	-7.82781×10^{-16}

mented during development, but not released for customer use, allows control over the sampling period. This command, ADxx, acquires data for 200 ms when issued. Processing and correcting for probe errors takes 2 seconds, before the data are transmitted through the instrument's serial port. Using this command allowed the motor to incrementally position the probe to each location and take data while the probe was in a fixed position, ensuring synchronization.

The two axes of motion, θ and z, are independently driven by stepper motors controlled through the Animatics 5000 interface. This interface directs commands through its RS-232 serial port into COM1 on the PC. Commands to control motion are stored in data files in the same directory as the main program according to their function.

The z-axis pertains to the motion along the beamline. During mapping of the quadrupoles, the motion will consist simply of 1 cm increments. Opto-sensors deter-

mine the absolute position of the probe for reproducible results at a fixed radius. The location of the radius is determined by an adjustment of the gaussmeter Hall probe holder.

The θ direction of motion is along the circumference of the beamline. This circumference is divided into discrete location, either 120, 180 or 360 depending on the chosen resolution. Each data sample consists of the probe being position at the precise location, while the control program allows the gaussmeter to sample data. After data sampling, the probe position is incremented until the index opto-sensor is actuated when the revolution is complete.

5.3   S800 beamline quadrupole triplet mapping

An integral part of the S800 spectrometer is the analysis line which consists of fifteen superconducting quadrupoles and four superconducting dipoles. The beamline brings the beam from grade level into the spectrometer, which is situated in a ten meter deep pit. The quadrupoles are larger version of the NSCL's standard beamline quadrupoles. The standard quadrupoles have a 12.7 cm diameter inscribed circle and S800 beamline quadrupoles are 20.3 cm in diameter. The beamline quadrupoles are arranged into triplets with 3 magnets in a common cryostat. To achieve the required energy and angular resolution for nuclear physics experiments, the magnetic fields must be accurately known.

Data are stored on the internal hard drive until they are loaded to another computer for processing. At one degree step size, each revolution takes 14.35 minutes and produce a 15 kB data file. A Z-axis step of 1 cm will require 210 revolutions in order to adequately measure the length for the triplet and fringe fields. The total data file for each of these maps is 3.15 MB. A one degree map takes 51 hours to complete, with

Table 5.2: Mapping Time and File Size for S800 Beamline Quadrupole Triplet.

Parameter	1°Steps	2°Steps	3°Steps
Triplet Mapping Time	51 hours	34 hours	17 hours
Data File Size	3.15 MB	2.1 MB	1.05 MB

the mapping process requiring minimal operator supervision. Table 5.2 lists mapping times and file sizes.

Figure 5.2 shows the radial component of the magnetic field for the triplet when the currents for the three quadrupoles are 5, 15 and 10 A respectively [Zh95]. The optics for fragment separation mode have fifteen adjustable parameters so tuning the beam is only practical if the gradients are accurately known. On one pole tip of each quadrupole magnet a cryogenic Hall generator was mounted to provide reference for setting the magnetic field. The Hall generator was calibrated with the mapper gaussmeter at a known radius with a calibrated power supply. The measured gradients as a function of current for one quadrupole are shown in Figure 5.3. Each quadrupole will have its own calibration of gradient versus current (by reference to the cryogenic Hall generator). The cold Hall generator voltage and field gradient versus current for one of the magnets is given in Table 5.3.

5.4 Magnetic field analysis of the S800 beamline quadrupoles

Since the S800 beamline magnets are large versions of the NSCL's standard beamline magnets which are cold iron, iron dominated superconducting magnets, they differ from Panofsky and $\cos2\theta$ in that the field shaping is done primarily by iron poles.

Figure 5.2: The radial component of the magnetic field for the triplet when the currents for the three quadrupoles are 5, 15 and 10 A respectively.
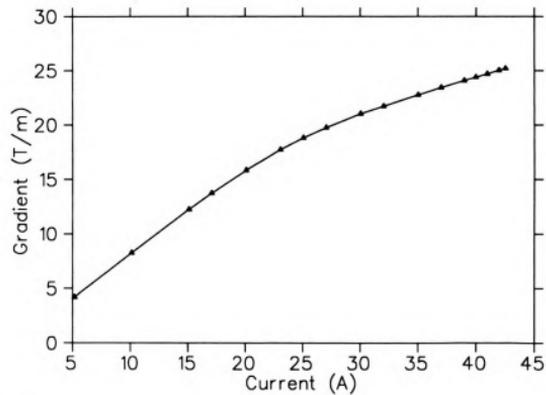
Figure 5.3: The gradient produced in a quadrupole as a function of current.

Table 5.3: The Hall generator voltages and gradients of a S800 beamline quadrupole as function of current.

Power Supply (A) Current (A)	Shunt Current (A)	Hall Generator Voltage (V)	Gradient (T/m) (T/m)
5.0	5.164	1.261	4.484
10.0	10.130	2.342	8.525
15.0	15.114	3.279	12.519
17.0	17.098	3.601	14.023
20.0	20.084	4.029	16.128
23.0	23.070	4.379	18.021
25.0	25.062	4.571	19.114
27.0	27.052	4.740	20.046
30.0	30.032	4.904	21.350
32.0	32.024	5.035	22.032
35.0	35.008	5.158	23.088
37.0	36.996	5.289	23.755
39.0	38.990	5.380	24.411
40.0	39.982	5.405	24.730
41.0	40.972	5.434	25.043
42.0	41.972	5.476	25.360
43.0	42.534	5.507	25.536

Effective Length for S800 Beamline Quadrupole
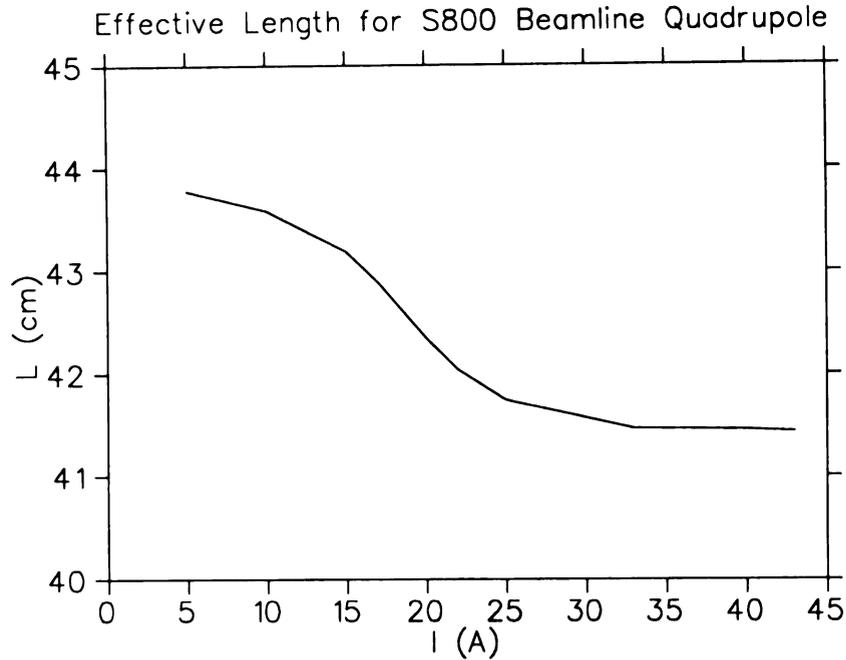
Figure 5.4: The effective length of the S800 beamline quadrupole as a function of current.

The effective length of the S800 beamline quadrupoles as a function of current is shown in Figure 5.4.

The radial component of magnetic field at the center is shown in Figure 5.5. Figure 5.6 shows a map and the harmonic content at a radius of 7.43 cm. The sextupole error is about 0.3 parts in a thousand of the quadrupole field. Note that only the N=6 and 10 terms are theoretically allowed, and the rest of the terms must result from construction errors, and/or mapper errors.

5.5   Q1, Q2 and sextupole magnet field mapping

The Q1, Q2 and sextupole magnets are mapped by using the same mapper. A z-axis step of 1 cm requires 180 revolutions in order adequately measure the length of the Q1, Q2 and sextupole magnets and fringe fields. A one degree map takes 43 hours to complete, with the mapping process requiring minimal operator supervision.
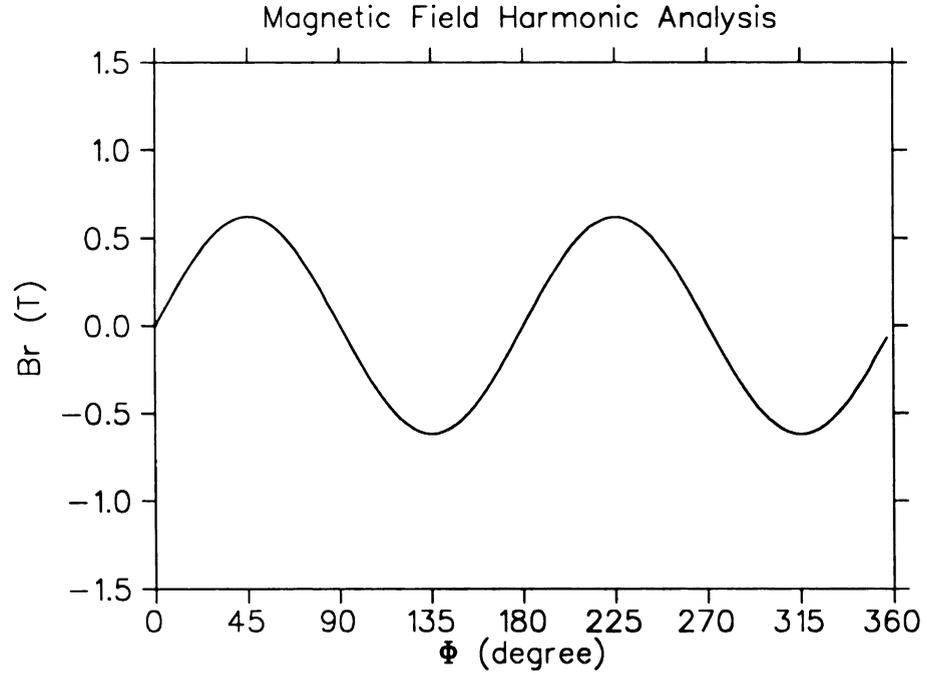
Figure 5.5: The radial component of magnetic field at the center at a radius of 7.43 cm.
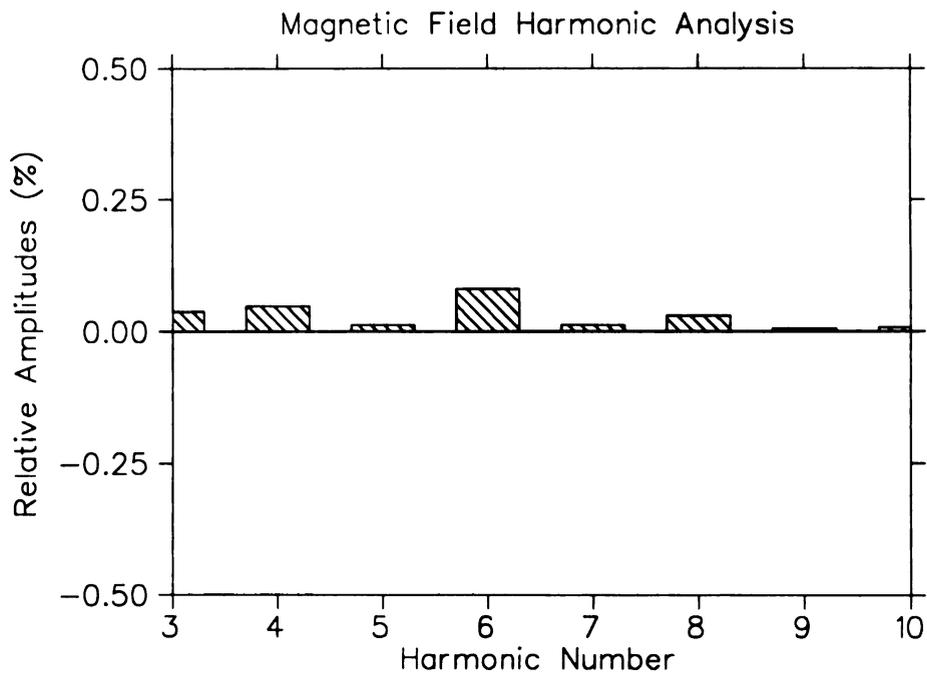
Figure 5.6: Fourier analysis of the radial component of the field in Figure 5.5.

Table 5.4: Mapping Time and File Size for the Q1/Q2 Doublet.

Parameter	1°Steps	2°Steps	3°Steps
Doublet Mapping Time	43 hours	29 hours	14 hours
Data File Size	2.7 MB	1.8 MB	0.9 MB

Table 5.4 listed mapping time and file size for the Q1/Q2 doublet.

Maps for different sets of currents have been done. Figure 5.7 shows the radial component of the magnetic field for the Q1/Q2 quadrupole doublet when the currents for the doublet are 84 and 70 A respectively. On two poles of the Q1 and Q2 magnets a cryogenic Hall Generator was calibrated with the mapper gaussmeter at a known radius with a calibrated power supply. Each quadrupole has its own calibration of gradient versus current (by reference to the cryogenic Hall generator). Table 5.5 and Table 5.6 lists the power supply current, shunt current, cryogenic Hall voltage and field gradient for Q1 and Q2.

The sextupole was mapped when the Q1 and Q2 magnets were on or off. Figure 5.8 shows the radial component of the magnetic field of the sextupole magnet when the currents of Q1 and Q2 are zero. Table 5.7 shows the sextupole shunt currents, cryogenic Hall generator voltages and field strengths for different power supply currents.

5.6 Magnetic field analysis of Q1, Q2 and the sextupole

The Q1 and Q2 magnet gradients have been measured using the quadrupole mapper [Zh97]. Figure 5.9 and Figure 5.10 show the gradient differences between the
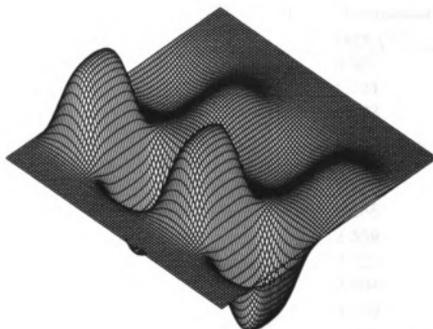
Figure 5.7: The radial component of the magnetic field for the Q1/Q2 doublet when the currents for Q1 and Q2 are 84 and 70 A respectively.

Table 5.5: The measurements of Q1 shunt current, cryogenic Hall generator voltage and field gradient.

Power Supply Current(A)	Shunt Current(A)	A Hall Generator Voltage (V)	B Hall Generator Voltage (V)	Gradient (T/m)
9.200	10.005	0.972	0.973	2.955
19.500	20.006	1.941	1.936	5.906
29.600	30.006	2.912	2.898	8.848
34.700	35.002	3.393	3.375	10.240
40.100	40.008	3.863	3.840	11.734
45.200	45.009	4.313	4.284	13.100
50.200	50.003	4.727	4.695	14.354
55.300	55.000	5.058	5.026	15.380
60.500	60.003	5.331	5.291	16.257
65.500	65.006	5.563	5.522	17.050
70.600	70.012	5.784	5.735	17.787
80.800	80.049	6.201	6.146	19.143
85.800	85.036	6.394	6.332	19.772

Table 5.6: The measurements of Q2 shunt current, cryogenic Hall generator voltage and field gradient.

Power Supply Current(A)	Shunt Current(A)	A Hall Generator Voltage (V)	B Hall Generator Voltage (V)	Gradient (T/m)
9.800	10.008	0.597	0.582	1.216
19.800	20.000	1.162	1.124	2.423
29.800	30.008	1.676	1.623	3.517
34.800	35.003	1.898	1.839	3.985
39.800	40.009	2.094	2.029	4.397
44.900	45.010	2.281	2.210	4.785
49.900	50.000	2.462	2.386	5.158
54.900	55.000	2.640	2.559	5.519
59.900	60.012	2.814	2.729	5.869
64.900	65.010	2.984	2.894	6.203
70.000	70.015	3.144	3.049	6.511
80.000	80.000	3.420	3.318	7.046
90.050	90.007	3.666	3.557	7.534
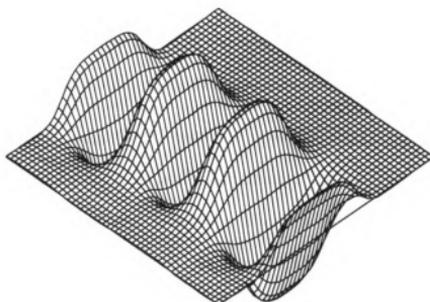
Figure 5.8: The radial component of the magnetic field for the sextupole when the sextupole current is 3 A, Q1 and Q2 are off.

Table 5.7: The measurements of the sextupole shunt current, cryogenic Hall generator voltages and field gradient.

PS I (A)	Shunt I (A)	A Hall Generator Voltage (V)	B Hall Generator Voltage (V)	Sextupole strength (T/m^2)
1.350	1.001	0.100	0.040	0.829
2.800	2.005	0.167	0.146	1.642
4.280	3.002	0.234	0.169	2.468
5.740	4.002	0.302	0.234	3.281
7.200	5.002	0.369	0.299	4.107
8.660	6.002	0.437	0.364	4.920
10.140	7.001	0.504	0.429	5.733
11.600	8.003	0.572	0.494	6.546
13.070	9.002	0.639	0.559	7.359
14.540	10.000	0.707	0.624	8.172

measurements and TOSCA calculations. The results of the mapping indicate that the magnets are in close agreement with TOSCA model predictions and the required specification for the S800 spectrometer.

The measured and TOSCA calculations of the effective lengths as a function of the gradients are shown in Figure 5.11 and Figure 5.12. The effective lengths of Q1 and Q2 decrease when the magnetic fields increase like beamline quads, the Q1 effective length differs by less a 1 % from the TOSCA calculations. For Q2 the effective length has a 2 % difference at low field, but gives close agreement at high currents.

For an ideal quadrupole, $B_{r,2}$ would increase linearly with r and would have no z dependence inside the magnet. Outside the magnet, $B_{r,2}$ would be zero. $B_{r,n}$ would be zero everywhere for $n \neq 2$. However, there is always a gradual decrease in the field near the end of the magnet. It is not possible to completely remove every higher order multipole. Figure 5.13 and Figure 5.14 show the harmonic content at the center and end of Q1 and Q2 at a radius of 8.8 cm. Note that only N=6 and 10 terms are theoretically allowed, and the rest of the terms must result from
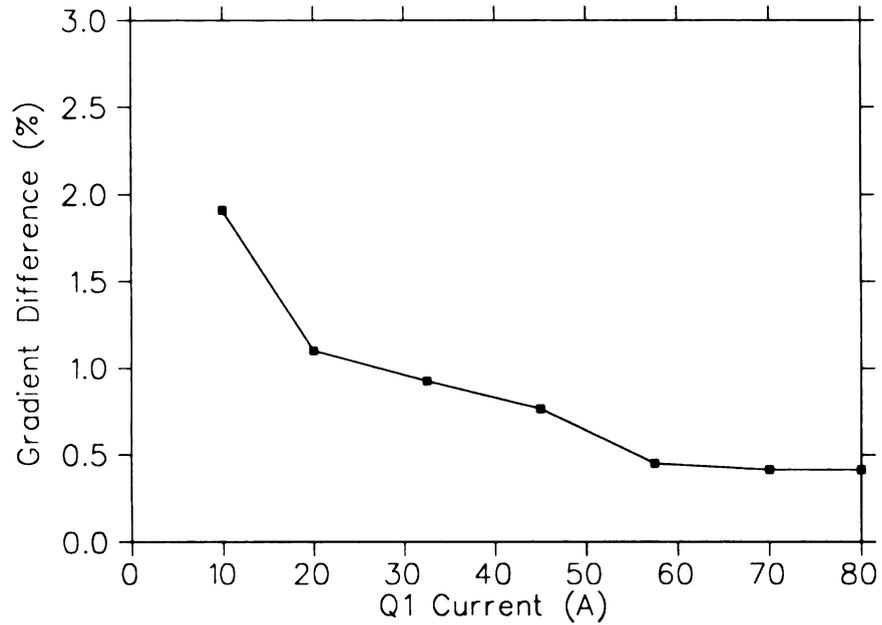
Figure 5.9: The Q1 gradient differences between the measurements and TOSCA calculations versus current.
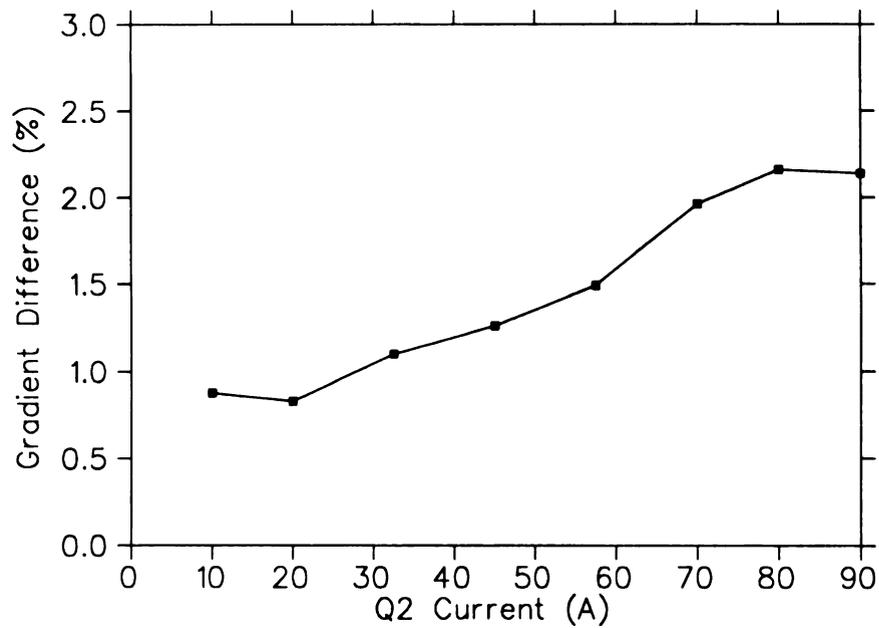
Figure 5.10: The Q2 gradient differences between the measurements and TOSCA calculations versus current.
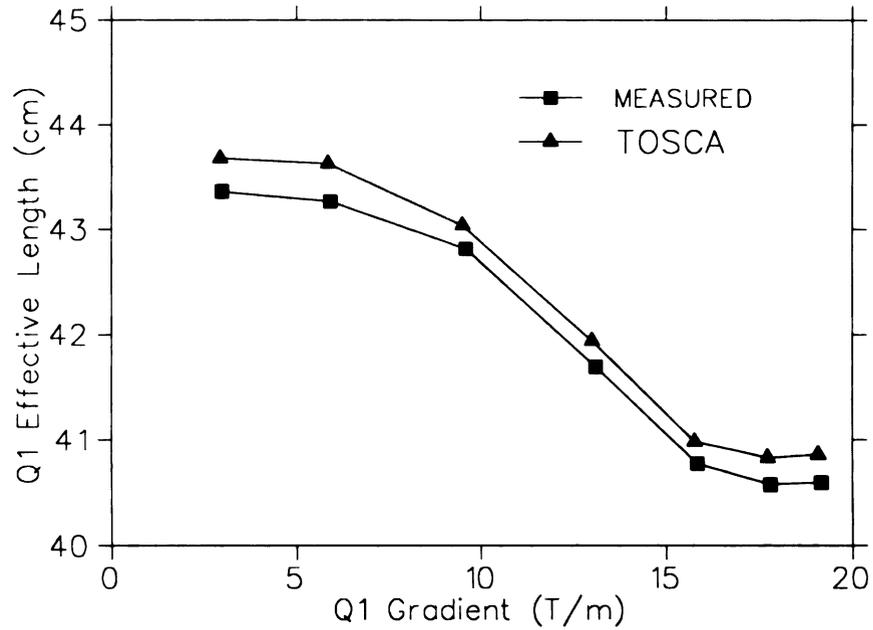
Figure 5.11: The Q1 effective length differences between the field measurements and TOSCA calculations versus gradient.
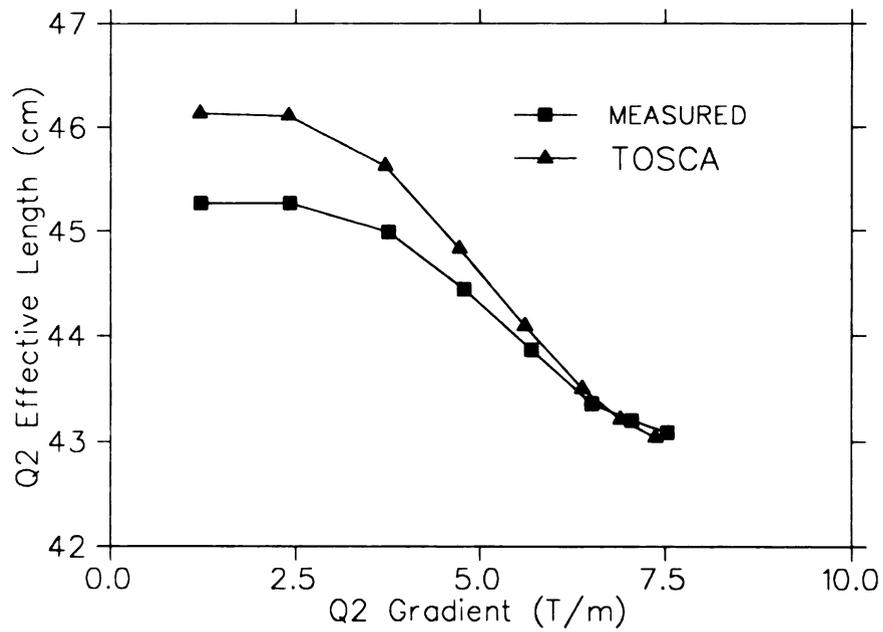
Figure 5.12: The Q2 effective length differences between the field measurements and TOSCA calculations versus gradient.

construction errors, or mapper errors. The N=6 terms at center of the magnets have big differences with those terms at end of the magnets. This is due to the coil return at ends which introduces significant higher order multipoles in the magnetic field. Fig. 5.15 and Fig. 5.17 show the various multipole components as a function of z, the field inside the Q1 and Q2 magnets is dominated by straight section of the coils, producing an almost pure quadrupole field. Near the ends of the Q1 and Q2 magnets, the higher order multipole fields increase greatly in strength. We have plotted the integrals of these functions in Fig. 5.16 and Fig. 5.18, integrated up to the plotted value of z, to show their convergence. Note that these components change sign at the ends of the Q1 and Q2 magnet iron, yielding a significant cancellation effect in the final field integral. Table 5.8 shows the peak multipole components and the integrated multipole components for the Q1 magnet current of 80 A and Q2 magnet current of 90 A. Table 5.9 and Table 5.10 list the multipole components of Q1 and Q2 for different currents. When the currents of the Q1 and Q2 magnets change, the sextupole, octupole and decapole components remain almost constant. However, the dodecapole components are strongly current dependant and are much larger at the ends of the magnets than at their centers.

We also mapped Q2 with the sextupole magnet on and off. Fig. 5.19 shows the multipole components for Q2 and the sextupole magnet at center of the magnets. As can be seen the sextupole magnet does not disturb the Q2 field, but does allow the addition of an n=3 component, as needed.

During mapping process, the field interaction between Q1 and Q2 has been measured. The field at the center of each magnet is independent of the other throughout the whole dynamic range.

The contribution to the magnetic field uncertainties from the mapping apparatus have been studied. The major error source likely comes from mapper/magnet mis-
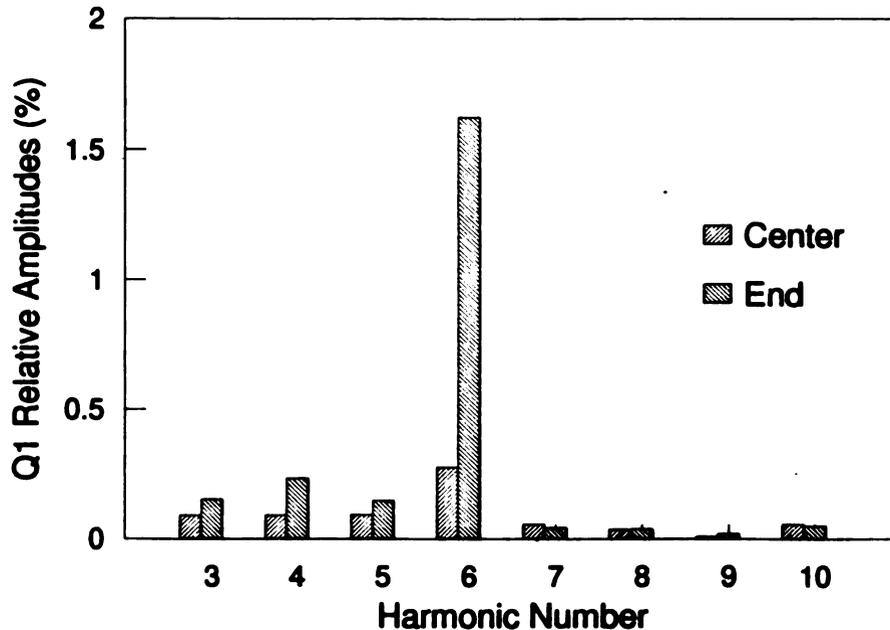
Figure 5.13: Fourier analysis of the radial component of the field in Q1 magnet at I = 45 A.

alignment. When we installed the mapper into the Q1/Q2 doublet, alignment was done using as optical transit. However, mapper/magnet alignment was extremely difficult and the difference between centers of less than ± 0.0127 cm could not be achieved. This error produces 0.1 % systematic error. Also, the Hall probe is temperature dependent with a temperature coefficient of ± 0.02%/C [Bell]. Once the mapper achieved thermal equilibrium in the bore of the doublet it changed little during mapping process. Therefore the relative contributions are very small, this does, however, limit the absolute field calibration of the magnets to ± 0.04%.
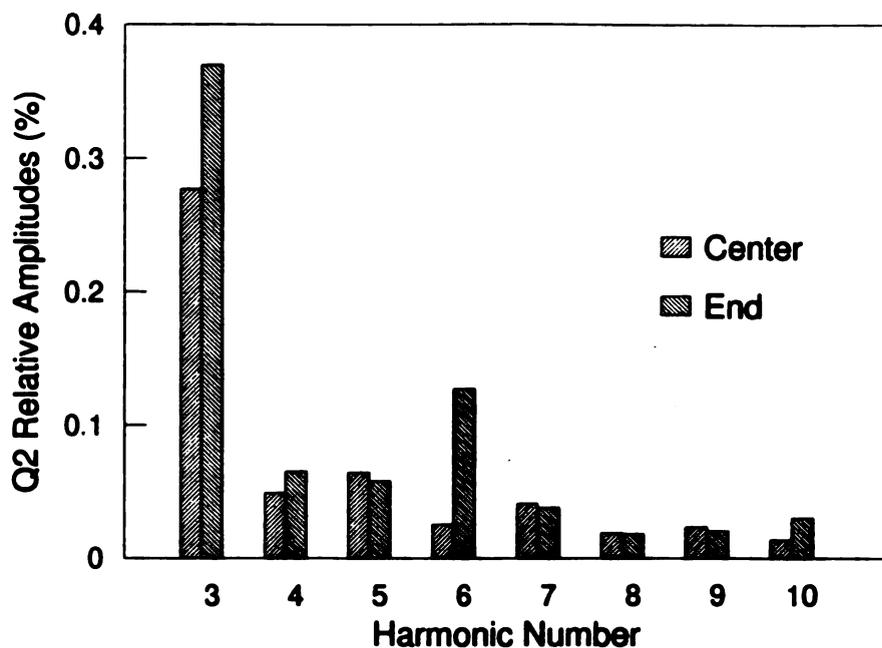
Figure 5.14: Fourier analysis of the radial component of the field at the center and end of Q2 at I = 45 A.

Table 5.8: Q1 and Q2 multipole analysis results at a radius of 8.8 cm.

n	Q1 (I=80 A)		Q2 (I=90 A)	
	Max $\mid B_{r,n} \mid (T)$	$\int_{-z}^{z} B_{r,n} dz (T \cdot m)$	Max $\mid B_{r,n} \mid (T)$	$\int_{-z}^{z} B_{r,n} dz (T \cdot m)$
2	1.687	0.685	0.663	0.286
3	2.8×10^{-3}	-4.4×10^{-4}	1.9×10^{-3}	7.9×10^{-4}
4	2.6×10^{-3}	-2.9×10^{-4}	7.4×10^{-4}	2.0×10^{-4}
5	2.0×10^{-3}	-6.0×10^{-4}	2.9×10^{-4}	1.2×10^{-4}
6	7.1×10^{-3}	-9.9×10^{-4}	1.1×10^{-3}	1.3×10^{-4}
10	1.8×10^{-3}	-2.5×10^{-4}	1.3×10^{-4}	4.4×10^{-5}
14	2.2×10^{-4}	1.4×10^{-5}	1.2×10^{-4}	4.0×10^{-5}

Q1 data analysis
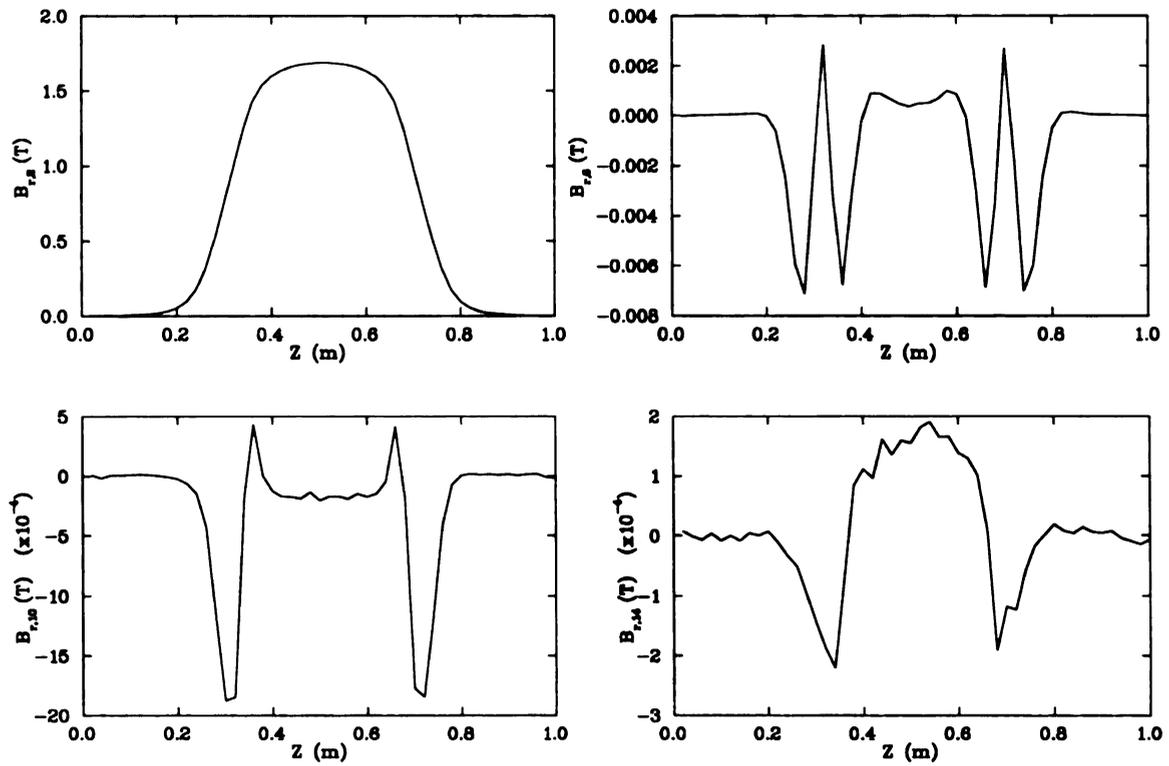
Figure 5.15: Multipole components of the Q1 radial field for the quadrupole (n=2) term and the first three allowed terms (n=6,10 and 14) are plotted as functions of z, the distance along the beamline axis at r = 8.8 cm and I = 80 A.

Q1 data analysis
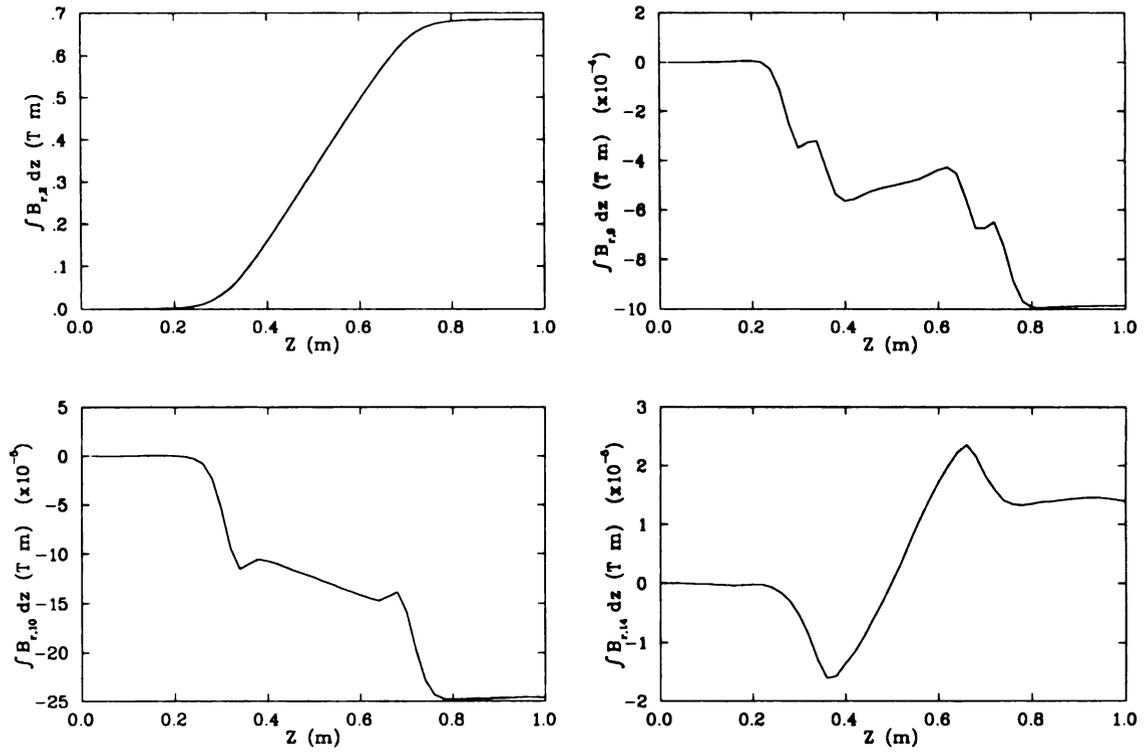
Figure 5.16: Integrated multipole component of the Q1 radial field $\int_0^z b_{r,n}dz$ for n=2, 6, 10 and 14 at r = 8.8 cm and I= 80 A.
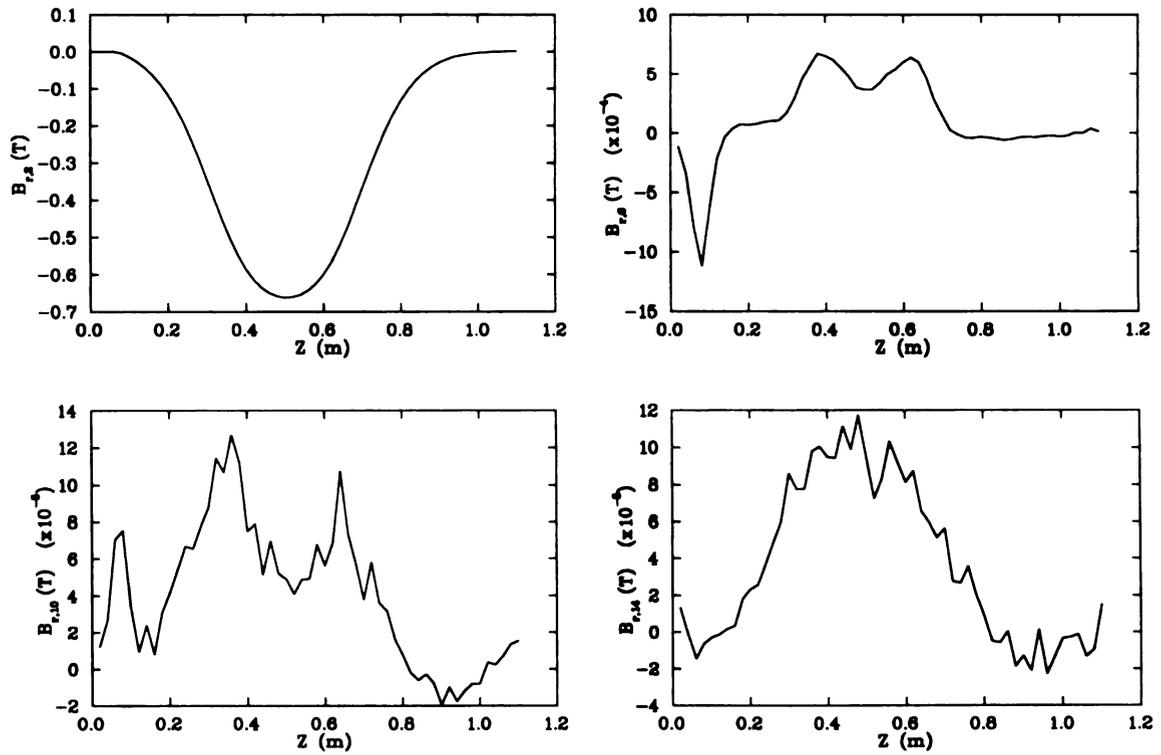
Figure 5.17: Multipole components of the Q2 radial field for the quadrupole (n=2) term and the first three allowed terms (n=6,10 and 14) are plotted as functions of z, the distance along the beamline axis at r = 8.8 cm and I = 90 A.

Q2 data analysis
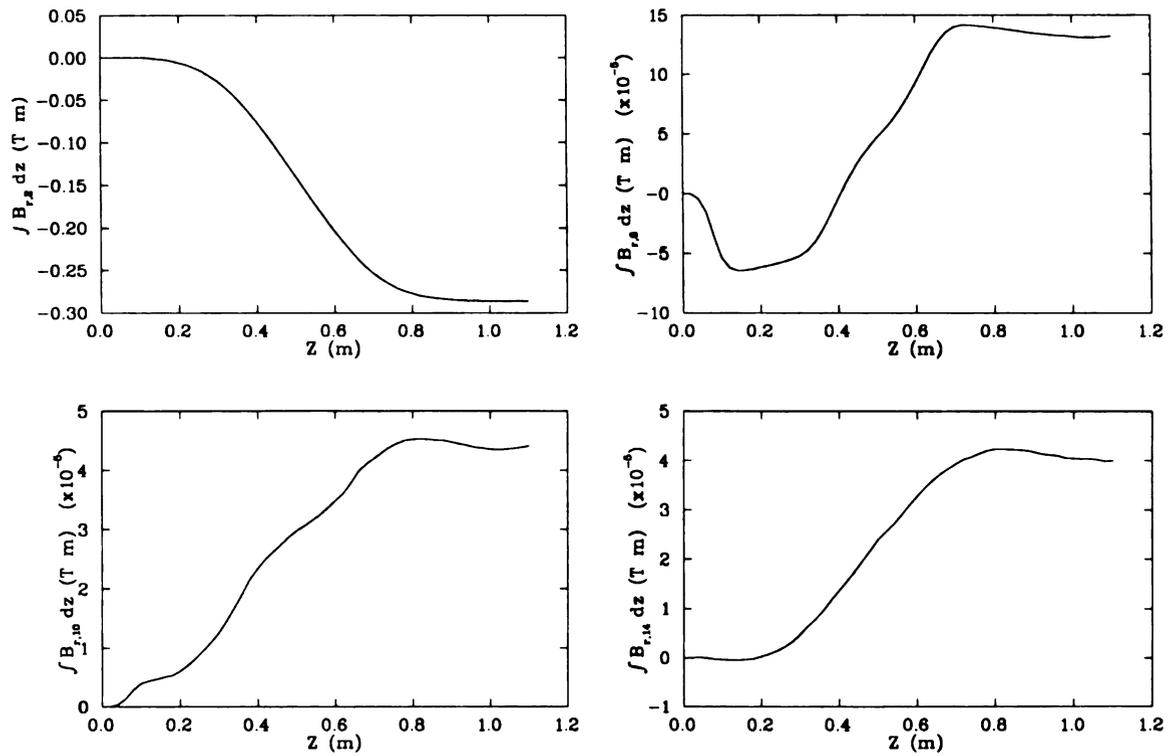
Figure 5.18: Integrated multipole component of the Q2 radial field $\int_0^z b_{r,n}dz$ for n=2, 6, 10 and 14 at r = 8.8 cm and I = 90 A.

Table 5.9: Harmonic components of the field at the center and end of Q1 at a radius of 8.8 cm for several currents. The numbers are defined by B_n/B_2 in %.

Current (A)	n=3		n=4		n=5		n=6	
	Center	End	Center	End	Center	End	Center	End
10	0.097	0.107	0.135	0.107	0.117	0.172	0.263	2.571
20	0.108	0.131	0.124	0.166	0.099	0.156	0.256	2.553
32.5	0.124	0.165	0.128	0.175	0.121	0.173	0.270	2.291
45	0.093	0.154	0.093	0.234	0.095	0.149	0.278	1.626
57.5	0.100	0.179	0.106	0.235	0.103	0.180	0.255	1.093
70	0.080	0.149	0.077	0.282	0.075	0.153	0.155	0.701
80	0.082	0.134	0.044	0.295	0.095	0.180	0.139	0.432

Table 5.10: Harmonic components of the field at the center and end of Q2 at a radius of 8.8 cm for several currents. The numbers are defined by B_n/B_2 in %.

Current (A)	n=3		n=4		n=5		n=6	
	Center	End	Center	End	Center	End	Center	End
10	0.271	0.307	0.053	0.073	0.074	0.059	0.026	0.192
20	0.233	0.295	0.022	0.033	0.036	0.036	0.005	0.175
32.5	0.318	0.367	0.074	0.094	0.058	0.068	0.015	0.167
45	0.277	0.347	0.049	0.066	0.064	0.067	0.025	0.162
57.5	0.321	0.383	0.078	0.107	0.058	0.081	0.020	0.145
70	0.257	0.327	0.030	0.060	0.042	0.043	0.049	0.112
80	0.256	0.338	0.018	0.067	0.043	0.046	0.052	0.111
90	0.285	0.370	0.024	0.065	0.063	0.055	0.054	0.091
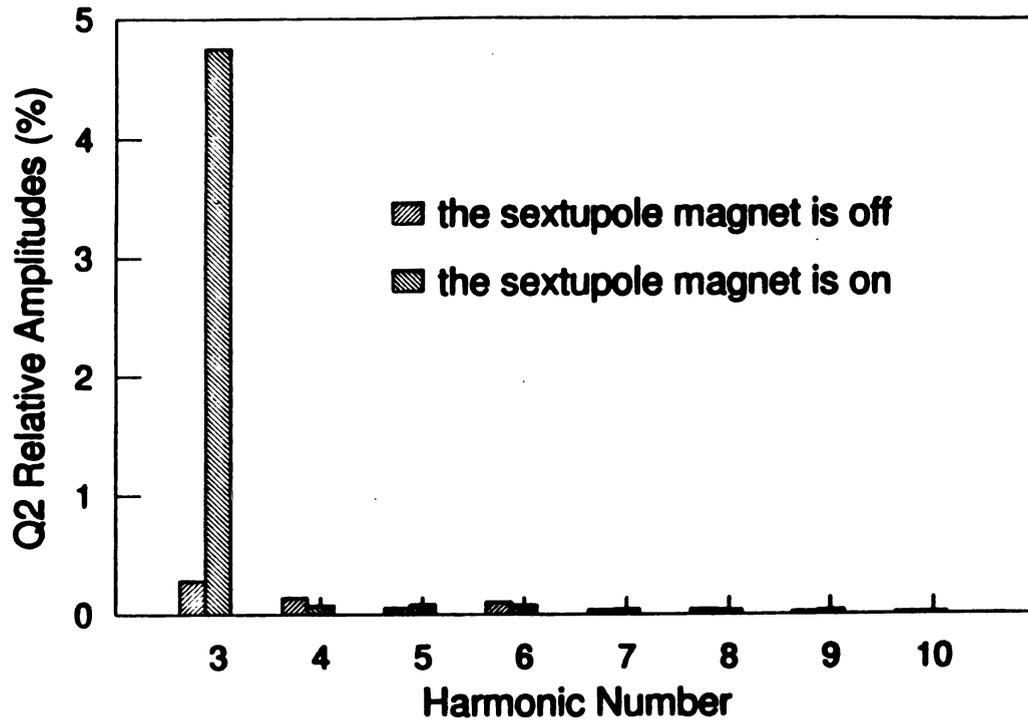
Figure 5.19: The Q2 and sextupole magnet multipole components at center of the magnets at $I_{Q2} = 70A$ and $I_{sextupole} = 3A$.

Chapter 6

Conclusion

This thesis describes the characteristics of the superconducting magnets for the NSCL spectrometer. In order to study the properties of the single particle states populated in reactions, the S800 spectrometer with energy resolution $E/\Delta E$ of 10,000 has been designed and constructed. The spectrometer design is based on a quadrupole-quadrupole-dipole-dipole layout and computer-optimized magnetic fields. The spectrometer magnets, along with the beam analysis line magnets, are superconducting magnets. The decision to use superconducting magnets was based on a cost analysis.

Considerable consideration went into the design and construction of the S800 dipole magnets. A two dimensional computer code has been used for the dipole design. To achieve the spectrometer requirements with the least amount of iron two features have been added to the basic H-frame magnet for the dipoles: The addition of resistive trim coils attached to the pole tip and at the median plane and the use of a tapered air gap behind the pole tip. The construction of the S800 dipole magnets with a negative side went well and the dipoles have achieved their design goals. The cryostable coils consist of 350 turns each and operate at 500 A. Both dipoles (D1 and D2) have been operated at full field. The forces on the D1 and D2 links are well within operational limits and are close to the calculated values. Detailed mapping of the S800 dipole magnets was performed using special mapping systems. The dipole mapping

system was based on the induced *emf* in a moving search coil. The deviations of the field gradients are less than 1 Gauss/cm, the spectrometer design requirements.

Two high gradient, large aperture quadrupoles (Q1 and Q2), for use as spectrometer elements, have been designed and constructed. Three basic type quadrupoles were considered for the design: a) $\cos(2\theta)$ type, where the field is shaped by the coil, b) Panofsky type, which is a square or rectangular current sheet approximation, and c) iron dominated type, where the iron pole tip primarily shapes the field. We decided against the $\cos(2\theta)$ quadrupoles because of the high current operation and its helium requirements. We also investigated superconducting Panofsky quadrupoles. A Panofsky design was not chosen due to the sensitivity of the field quality to errors in conductor placement and construction problem. From these studies and from experience with our standard beamline quadrupoles the iron dominated type had been chosen for Q1 and Q2.

This thesis presents the magnetic field calculations for Q1, Q2 and the sextupole using two- and three-dimensional computer codes. The individual maltipole components are extracted using a straightforward Fourier analysis. TOSCA was used to compute the total magnetic force on each coil. The code QUENCH was used to evaluate the quench behavior of these magnets. The calculations for these potted coils indicate that they are still conservatively designed.

All coils of Q1, Q2 and the sextupole are random and wet wound with epoxy on a simple winding table. After curing, the coils of Q1 and Q2 are shimmed against the poles tip first, then against each other by using titanium and G-10 spacers. Both Q1 and Q2 have cryogenic Hall generators mounted on the pole tips, to allow setting the magnetic field. Before being put into the liquid helium container, Q1 and Q2 were rigidly connected together so that alignment was maintained. The sextupole coils are held in position with G-10 spacers and stainless steel bands. Q1 and Q2 have been

operated at full field. The measured total heat load on the cryogenic container is 2 Watts, which is consistent with our calculation.

To achieve the required energy resolution and angular resolution for nuclear physics experiments, the magnetic fields must be accurately known. The quadrupole mapper consists of a gaussmeter and a dual axis motor controller. The three axis hall probe of the gaussmeter has been calibrated to absolute field with NMR measurements. Maps for different sets of currents have been done. The cryogenic Hall generators were calibrated with the mapper gaussmeter at a known radius with a calibrated power supply. Each quadrupole has its own calibration of the gradient versus current by reference to the cryogenic Hall generator.

The results of the mapping indicate that the magnets are in close agreement with TOSCA models predictions. The integral contribution of the 12-pole of Q1 and Q2 relative to the quadrupole terms, respectively, are 1.4×10^{-3} and 4.5×10^{-4}. The sextupole magnet in Q2 operated up to its design value, 5.7 T/m^2 , with both Q1 and Q2 magnets running at maximum operation currents.

Initially, the CTI-1400 liquefier (40 l/hr or 100 Watt) alone was available to operate the spectrometer system of D1, D2, Q1/Q2 doublet, it was impossible to use continuous feed mode for all magnets due to the elevated pressure in the return gas stream. It was found that operating D1 and D2 in continuous feed mode and filling the Q1/Q2 doublet once daily would allow continuous operation on the order of a week before having to shut down to replenish liquid in the storage dewar. The estimated heat load of operating the spectrometer system in continuous feed is approximately 100 Watts. This is the mode of operation since bringing on line a new liquefier which first produced liquid on Dec. 3, 1996. With the new liquefier in operation the spectrometer magnets remain full and at the same time liquid is accumulated in a 2500 liter dewar which is then also used to perform the daily bath filling operation of the

s800 beamline magnets.

The S800 spectrometer was completed and commissioned in September 1996. Without computer software correction, the energy resolution obtained was 1 part of 5,000. This is a very good value for a first attempt, and within a factor of two of the design resolution. The quadrupole map data have been processed and processing continues on the dipole data. The next significant challenge is to use COSY INFIN-ITY and the measured magnetic field data to determine the coefficients in the ray reconstruction.

Bibliography

[Ak50]   S. W. Akin, *Trans. ASME,* **72**, (Aug. 1950) 751-57.

[Al95]   J. S. Alcorn, private communication.

[An89]   N. Anantaraman, B. Sherrill, *Proc. Int. Symp. Conf. on Heavy Ion Research with Magnetic Spectrographs,* MSUCL-**685**, (April 1989).

[Be93a]   M. Berz, Computer simulation of beam optics, version **6**.

[Be93]   M. Berz, K. Joh, J. A. Nolen, B. M. Sherrill, A. F. Zeller, *Phys. Rev. C,* **47**, (1993) 537.

[Bell]   F. W. Bell, *Operation Manunal,* Series 9900 Gaussmeter, 1.

[Bo93]   P. Bogensberger, R. K. Maix, F. Ramsauer, A. Umschaden, H. Köfler, K. Piswanger, P. Brindza, *IEEE Transactions on Applied Superconductivity,* **3**, (1993) 797.

[Bu48]   W. W. Buechner, E. N. Stait, C. G. Stergiopolos, A. Sperduto, *Phys. Rev.,* **74**, (1948) 1569.

[Ca]   J. Caggiano, private communication.

[Co83]   W. E. Cooper, et al. *IEEE Transactions on Magnetics,* MAG-**19**, (1983) 1372.

[De]   J. DeKamp, NSCL Technical Notes.

[Ha59]   L. H. Hand, W. H. Panofsky, *Magnetic Quadrupole with Rectangular Aperture,* Rev. Sci. Instr. **33**, (1959) 927.

[Ha89]   L. H. Harwood, *Proc. Int. Symp. Conf. on Heavy Ion Research with Magnetic Spectrographs,* MSUCL-**685**, (April 1989) 305.

[Ho81]   J. P. Holman, *Heat Transfer,* McGraw-Hill, Inc. (1981) 336.

[Ha96]   L. H. Harwood, private communication.

[Jea]   J. E. Jensen, R. B. Stewart, W. A. Tuttle, *Bubble Chamber Group,* Selected Cryogenic Data Notebook, VII-O-4.

[Jeb]   J. E. Jensen, R. B. Stewart, W. A. Tuttle, *Bubble Chamber Group,* Selected Cryogenic Data Notebook, VII-Q-2.

[Le80]   E. M. W. Leung, R. W. Fast, H. L. Hart, J. R. Heim, *Advances In Cryogenic Engineering*, **25**, (1980) 489.

[Ma65]   J. B. Marion, *Classical Electromagnetic Radiation*, Academic Press, (1965) 79.

[Mo79]   Model 253, *Autoranging Digital Impedance Meter*, Electro Scientific Industries, Inc. (1979) 2-16.

[Mo]   C. L. Morris, H. A. Thiessen, Los Alamos, private communication.

[Mu89]   A. Mueller, GANIL Beamtime Coordinator, private communication.

[Mu88]   G. Muenzenberg, *Rep. Prog. Phys.*, **51** (1988) 57.

[Na91]   J. Napolitano, T. Hunter, *Nucl. Instr. Methods in Phy. Res.*, **A301** (1991) 465-472.

[Nbs]   *NBS LNG Users Manual*, LNG Materials & Fluids Data, Boulder, Colorado, (1979), 2.

[No75]   J. A. Nolen, P. S. Miller,,   *Proc. 7Th Conf. on Cyclotron*, Berkhaeuser, Basel, (1975) 249.

[No78]   J. A. Nolen, L. H. Harwood, E. Kashy, *MSU Ann. Report*, (1978-1979), 102.

[No79]   J. A. Nolen, MSUCL-**308**, (August 1979), (unpublished).

[No81]   J. A. Nolen, *ibid*, IV-F1.

[No81a]   J. A. Nolen, Proc. Workshop on High-resolution, Large-acceptance Spectrometers, ANL/PHY-**81-2**, IV-E.

[No81b]   J. A. Nolen, Proc. Workshop on High-resolution, Large-acceptance Spectrometers, ANL/PHY-**81-2**, III-B.

[No83]   J. A. Nolen, et al. *Proc. 12th Int. Conf. on High-Energy Acc.*, FNAL (1983) 549.

[No89]   J. A. Nolen, A. F. Zeller, B. Sherrill, J. C. DeKamp, J. Yurkon, *A Proposal for construction of the S800 Spectrogragh*, MSUCL-**694**, July 1989.

[No]   J. A. Nolen, *ibid*, III-B1.

[Re83]   R. P. Reed, A. F. Clark, *Materials at Low Temperatures*, American Society for Metals, (1983) 486.

[Ro]   The idea of using a larger resolving power in the beam analysis system than in the spectrograph itself came from discussions with P. Roussel of Orsay.

[Sh92]   B. M. Sherrill, D. J. Morrissey, J. A. Nolen Jr., N. Orr, J. A. Winger, *Nucl. Instr. Methods in Phy. Res.*, **B70** (1992) 289-303.

[Th79]   H. A. Thiessen, M. Klein, K. Boyer, LASL Report (1979) unpublished.

[To]   TOSCA, Version **6.3**, Vector Field, Inc. 1700, N Farnsworth Ave., Aurora, IL 60505.

[Wi68]   M. N. Wilson, Computer Simulation of the Quenching of a Superconducting magnet, RHEL/M 151 (1968).

[Ze79]   A. F. Zeller, J. A. Nolen, L. H. Harwood, E. Kashy, *MSU Ann. Report,* (1979-1980), 78 (unpublished).

[Ze80]   A. F. Zeller, J. Nolen, L. H. Harwood, *ibid* 1980-1981, 105.

[Ze81a]   A. F. Zeller, J. Nolen, L. H. Harwood, *ibid* III-C1.

[Ze81]   A. F. Zeller, J. A. Nolen, L. H. Harwood, E. Kashy, *ibid* V-B1.

[Ze84]   A. F. Zeller, et al. *Proc. of 10th Int. Conf. on Cyclotron,* New York, IEEE Press, (1984), 79-81.

[Ze86]   A. F. Zeller, Proc. Workshop on CEBAF Spectrometer Magnet Design and Tech. (1986) 11.1.

[Ze92]   A. F. Zeller, et al. *Adv. in Cryogenic Engineering,* **37**, (1992) 417.

[Ze93]   A. F. Zeller, S. Bricker, J. C. DeKamp, H. Laumer, J. A. Nolen, R. T. Swanson, B. Zhang, *IEEE Transactions on Applied Superconductivity,* **3**, (1993) 114.

[Ze94]   A. F. Zeller, J. C. DeKamp, E. M. W. Leung, R. W. Fast, *Adv. in Cryogenic Engineering,* **39B**, (1994) 1691-1697.

[Ze95]   A. F. Zeller, J. C. DeKamp, C. Magsig, J. Wagner, D. Pendell, *IEEE Transactions on Applied Superconductivity,* **5**, (1995) 1032.

[Ze95a]   A. F. Zeller, S. Bricker, L. Morris, D. Pendell, R. Swanson, R. Fontus, B. M. Sherrill, H. Laumer, B. Zhang, D. Sanderson, J. C. DeKamp, P. Johnson, J. Caggiano, *IEEE Transactions on Applied Superconductivity,* **5**, (1995) 654.

[Zh95]   B. Zhang, P. Johnson, B. Sherrill, A. F. Zeller, R. Zink, *MSU Ann. Report,* (1995) 229-233.

[Zh96]   B. Zhang, A. F. Zeller, J. DeKamp, P. Johnson, B. Sherrill, R. Swanson, R. Zink, *Adv. in Cryogenic Engineering ,* **41A**, (1996) 375-381.

[Zh97]   B. Zhang, A. F. Zeller, S. Bricker, R. Berleigh, J. DeKamp, P. Johnson, B. Sherrill, R. Swanson, R. Zink, *IEEE Trans. on Applied Superconductivity,* in press.